Numerical and experimental studies of coherent Smith-Purcell radiation

Faïssal BAKKALI TAHERI
University College Oxford

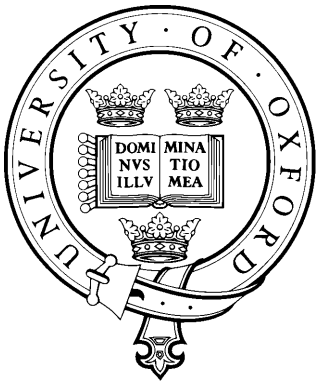

Thesis submitted in partial fulfilment of the requirements for the degree of Doctor of Philosophy at the University of Oxford

Trinity Term, 2016

Abstract

This thesis investigates the properties of coherent Smith-Purcell radiation (cSPr) at femtosecond-scale in the case of electrons bunches in the ultrarelativistic regimes. Of particular interest is the use of cSPR as a diagnostic tool to determine the longitudinal time profiles of such bunches, the study of azimuthal distribution of the radiated energy, and a contribution to the understanding of polarization properties. The study consists in a first theoretical part carried mostly in the context of the surface-current theory, supported with insights from particle-in-cell simulations. Then, as a step toward a better determination of time profile, the question of phase reconstruction is addressed through the design of a new algorithm proposed in this thesis and tested in known challenging cases. Experimental results are then presented, spanning shifts having taken place at the FACET facility at SLAC, Stanford, between 2013 and 2015.

I dedicate this work to my parents.

Declaration

The experimental and numerical work contained within this thesis is original research carried out by the author, unless otherwise stated, in the University of Oxford, and at SLAC National Accelerator Laboratory, Stanford, USA, under the authority of the University of Oxford. The work has been carried out between October 2012 and October 2016. No material contained herein has been submitted for any other degree, or at any other institution. All the figures and photographs are made by the author, unless otherwise stated in the caption. In particular, the figure 2.2 originates from the page https://fdtd.wikispaces.com/The+Yee+Cell and is publicly available under Creative Commons Attribution Share-Alike 3.0 License, with the original filename YeeCell01.jpg.

Results from other authors are referenced in the usual manner throughout the text.

Selected original results of the chapter 2, 3, and 5 have been published in the four following papers:

H.L. Andrews, F. Bakkali Taheri, J. Barros, R. Bartolini, V. Bharadwaj, C. Clarke, N. Delerue, G. Doucas, N. Fuster-Martinez, M. Vieille-Grosjean, I.V. Konoplev, M. Labat, S. Le Corre, C. Perry, A. Reichold, and S. Stevenson

Reconstruction of the time profile of 20.35 GeV, subpicosecond long electron bunches by means of coherent Smith-Purcell radiation

Phys. Rev. ST Accel. Beams 17, 052802

F. Bakkali Taheri, I.V. Konoplev, G. Doucas, P. Baddoo, R. Bartolini, J. Cowley, and S.M. Hooker

Electron bunch profile reconstruction based on phase-constrained iterative algorithm,

Phys. Rev. Accel. Beams 19, 032801

F. Bakkali Taheri, J. Barros, R. Bartolini, C.I. Clarke, N. Delerue, G. Doucas, I.V. Konoplev, and A. Reichold

Experimental and Theoretical Studies of the Properties of Coherent Smith-Purcell Radiation

Proc. 7th International Particle Accelerator Conference (IPAC'16), Busan, Korea, Mar. 2016, paper MOPMR041, pp. 344–346

F.B. Taheri, I.V. Konoplev, G. Doucas, A. Reichold, R.J.D.A. Smith, R. Bartolini, N. Delerue, H. Andrews, N. Fuster-Martínez, C. Clarke, V. Bharadwaj, P.H. Stoltz

Spectra of coherent smith-purcell radiation observed from short electron bunches: Numerical and experimental studies

IPAC 2013: Proceedings of the 4th International Particle Accelerator Conference (2013) 801-803

and in the general context of this PhD, I also contributed to the following list of publications:

J.Barros, N.Delerue, S.Jenzer, M.Vieille-Grosjean, F.Bakkali Taheri, G.Doucas, I.Konoplev, A.Reichold, C.Clarke

Reconstruction of longitudinal electrons bunch profiles at FACET, SLAC

IPAC 2014: Proceedings of the 5th International Particle Accelerator Conference (2014) 3453-3455

J.Barros, S.Le Corre, N.Delerue, M.Vieille-Grosjean, F.Bakkali Taheri, R.Bartolini, G.Doucas, I.Konoplev, C.Perry, A.Reichold, S.Stevenson, L.Cassinari, M.Labat, H.L. Andrews, N.Fuster-Martinez, C.Clarke

Longitudinal profile monitors using Coherent Smith-Purcell radiation

1st European Advanced Accelerator Concepts Workshop (EAAC2013), Jun 2013, La Biodola, Italy. Elsevier, 740, pp.212-215, 2014

F.B. Taheri, I.V. Konoplev, G. Doucas, A. Reichold, R.J.D.A. Smith, R. Bartolini, N. Delerue, H. Andrews, N. Fuster-Martínez, C. Clarke, V. Bharadwaj, P.H. Stoltz

Spectra of coherent smith-purcell radiation observed from short electron bunches: Numerical and experimental studies

IPAC 2013: Proceedings of the 4th International Particle Accelerator Conference (2013) 801-803

I.V. Konoplev, F.B. Taheri, G. Doucas, A. Reichold, R. Bartolini, N. Delerue, C. Clarke, V. Bharadwaj

Some properties of coherent smith-purcell radiation from electron bunches and gratings of finite dimensions

International Conference on Infrared, Millimeter, and Terahertz Waves, IRMMW-THz (2013)

N. Fuster-Martínez, A. Faus-Golfe, J. Resta-López, N.Delerue, J. Barros, M. Vieille-Grosjean, A Reichold, C. Perry, F. Bakkali, G. Doucas, I. Konoplev, R. Bartolini, S. Stevenson, H. Andrews, C. Clarke, V. Bharadwaj

Feasibility study of a 2nd generation smith-purcell radiation monitor for the ESTB at SLAC

IPAC 2013: Proceedings of the 4th International Particle Accelerator Conference (2013) 634-636

N. Delerue, J. Barros, S. Le Corre, M. Vieille-Grosjean, F. Bakkali Taheri, R. Bartolini, G. Doucas, I.V. Konoplev, C. Perry, A. Reichold, S. Stevenson, N. Fuster Martinez, H An-

drews, V Bharadwaj, C Clarke, M Labat

Longitudinal profile monitor using smith-purcell radiation: Recent results from the E-203 Collaboration

IBIC 2013: Proceedings of the 2nd International Beam Instrumentation Conference (2013) 464-466

Acknowledgements

I would like to thank my supervisor, Ivan Vasilyevich Konoplev. Ivan has advised me through all the major steps of my work on a regular basis, giving some of his precious time and support when needed. I also learned much from his experience in particle-in-cell simulations, where his guidance helped me to avoid falling in the usual traps and obstacles met by many early researchers in the field. I must also thank the whole E203 team who has been a major source of inspiration, and first and foremost Dr George Doucas, an emeritus physicist who has been one of the original authors of the mathematical formulation of the surface-current theory, the backbone of my work. As well as Ivan has been the main source of inspiration for the near-field analysis, George was the main one for the far-field, and again I learned much of his past experience gained from the early work on Smith-Purcell far-field analysis. I must also thank the rest of the E203 team: Nicolas Delerue, who played a critical leading role during the shifts we had at SLAC, Riccardo Bartolini, Joanna Myriam Barros, as well as the past members who contributed: Armin Reichold, Melissa Vieille-Grosjean and Nuria Fuster Martinez. I would like also thank Simon Hooker and James Cowley for their collaboration in the PCI algorithm paper we published. I would like to thank also the support to this PhD provided by University College Oxford, in particular my College PhD advisor, Patrick Edmond George Baird, as well as Peter Jezzard and Mrs Angela Unsworth.

This work would not have been possible without the access to major facilities, laboratories and supercomputers, and here I must thank the whole SLAC team with whom I worked very closely during the nine months I spent there: Christine Isabel Clarke, Alan Samuel Fisher, Doug McCormick, Juan Cruz, Zenon Szalata, Mike Litos and Spencer Gessner. I must also thank all the people who have been involved in the use of Oxford Supercomputing facilities

with the *VSim* commercial software, both at the local Physics Dept (JAI cluster) and the Central Mainframe, where I worked on Arcus and Hal : here I must mention Jonathan Smith, from Tech-X Corporation, the company who designed *VSim*, as well as Nicolas Bourgeois with whom I had several extremely useful meetings in my early stage of *VSim* work. Then, for the Departmental supercomputers, I would like to thank the Unix division: Sean Brisbane , Kashif Mohammed, Peter Gronbech and Ewan McMahon. For the Arcus and Hal systems, I would like to thank Steven Young and Mihai Duta too. I would like finally thank Sue Geddes and Kim Proudfoot for having been so helpful and patient during all these years.

It is important to realize that the PhD is not only a work on its own, but also a step along a continuous academic chain started from the very early undergraduate years, and as such, all past professors, lecturers, assistants are parts of that chain of knowledge. In particular, I would not have been here without all my previous dissertation supervisors (undergraduate and MSc) who all contributed to make me an apprentice physicist, and the academics who kindly provided references to help me going first to the MSc at Imperial College London, then to this PhD. For this reason I would like to thank them here: Jean-Claude Matthys and Guy Boulet (both of them my supervisors at the I.S.P.G., Brussels, Belgium), Yves Brihaye (who supervised my undergraduate dissertation at the former Université of Mons-Hainaut, now renamed as Université of Mons, Belgium), Claude Semay, Jonathan Halliwell (who supervised my MSc dissertation at Imperial College London), Daniel Waldram and Kellog Stelle. With my current supervisor Ivan, they all contributed to construct myself as a physicist, and were all of them steps toward this PhD achievement.

I would like to thank my parents, my family and my wife Mrs Nurfariza Bahrin. Their constant support have been a key factor that has continuously driven me forward in the challenging times I have been through. This was even truer after my funding finished, for their provided the help without which I would never have made it up to the end of this thesis. All of them have to be gratefully acknowledged for the very wise advices heir provided during these difficult times.

Finally, I would like to gratefully acknowledge the Support of the UK Science and Technology Facilities Council, who financially supported this work (STFC reference 1237217, ID

B103491E), and the US Department of Energy who provided the financial support required to access and use SLAC research facilities (DoE Contract DE-AC02-7600515).

A quoi bon savoir ce qu'est une droite, si l'on ignore ce qu'est la droiture?

Lucius Annaeus Seneca, letter 88

Contents

List of Figures

List of Tables

List of abbreviations

cSPR coherent Smith-Purcell Radiation.

DAQ Data acquisition.

DR Diffraction radiation

FACET Facility for Advanced Accelerator Experimental Tests.

FIR Far infra-red.

FPGA Field-Programmable Gate Array

FEL Free electron laser.

FFT Fast-Fourier transform

GFW Grating of finite width

.h5 Main output family of files of the *VSim* simulation software

LCLS Linac Coherent Light Source

OTR Optical transition radiation

.PRE Source file of the *VSim* simulation software

SPR Smith-Purcell radiation

TCAV Transverse cavity.

Chapter 1

Introduction

1.1 Beam diagnostics in particle accelerators

Diagnostics in the context of accelerator physics, is the research area that deals with the measurements of beam quantities that are involved in experiments. In some traditional approaches [1], it is distinguished in three types:

(i) A first type deals with the fundamental machine parameters that have to be determined immediately, such as the current of the beam.

(ii) A second type includes diagnostics which measure machine parameters at hardware level that are needed for troubleshooting, or more complex physical quantities such as the beam profile.

(iii) Finally we have diagnostics which measure parameters of more sophisticated nature that often require the commissioning of a dedicated structure. Typical examples are beta-function or emittance.

The various quantities determined through diagnostics can be of interest not only for experiments that are parts of the accelerator, but also for the life and performance of the accelerator itself: the diagnostic outputs are often sent as input into feedback systems into

the machine, to allow the auto-correction of the system if a quantity drifts from a designated set up. A typical example is the trajectory correction of a beam across the accelerator, which depends largely on such feedback systems. Despite a certain level of automation however, human monitoring is still required and diagnostics personnel can involve large proportions of the scientific personnel and a non-negligible cost. Beam diagnostics is therefore an essential part of an accelerator life.

The requirements of the diagnostics usually depend on the type of machine used. The research covered in this thesis is set in a linac, where the requirements would be different from a synchrotron, for example, as explained in detail in [1]: in a linac each sector is reached by the beam only once, while in a synchrotron, multiple turns are usually required. For this reason, linac can more easily accommodate destructive techniques of measurements.

In every diagnostic methodology, one is always driven by the following chain of three questions:

(i) What is the physical quantity we want to determine?

(ii) What (usually other) physical phenomena can I investigate to achieve this goal?

(iii) What device could we set up to use the measurement of the physical quantity in the step (ii) and deduce from it the desired diagnostics of the required quantity in step (i)?

Such a methodology is present in many areas of physics which are not necessarily related to Accelerator Science: for example we can consider the simple case of electronic sensors of temperature: with respect to the above questions, the quantity to determine in (i) would be the temperature, the physical phenomena in (ii) would be voltage, and the device in (iii) would be a transducer.

The main focus of this work will be the determination of a very specific quantity, the longitudinal time profile, through the measurement and spectral analysis of the Coherent Smith-Purcell Radiation (CSPR), which is generated, investigated and explained in the framework of classical electrodynamics.

1.2 General properties of coherent radiation

Coherent radiation is generated by the charged particle of a bunch when the wavelength of the radiation is of same order than the bunch length, or longer. We are interested in the determination of longitudinal bunch profile and the method chosen here will be the reverse Fourier Analysis of spectrum of coherent emission in the Terahertz and sub-THz region. This approach is called coherent radiation diagnostics (CRD) and its principles are well established [2]. Bunch diagnostics through coherent radiation measurements are not the only methods, and some other techniques, such as electro-optics measurements and X-ray generation, are widely used too, but they will not be discussed in the frame of this work.

The basic idea of coherent radiation diagnostics, is to consider the behaviour of the electric field at a distant point from the bunch, in the far-field. In the far-field point, the coherent radiation from every individual charge of the bunch will add up leading to the total effect of N charged particles being given by

$$\vec{E}(t) = \sum_{i=1}^{N} \vec{E}_i(t) \tag{1.1}$$

the fields add up with a time delay with respect to a specific reference:

$$\vec{E}_i(t) = \vec{E}_1(t + \Delta t_i) \tag{1.2}$$

With this, the total electric field in the observation point, expressed in the frequency domain, becomes:

$$\vec{E}(\nu) = \vec{E}_1(\nu) \sum_i e^{2\pi i \nu \Delta t_i} \tag{1.3}$$

which yields the energy density:

$$\frac{\mathrm{d}I}{\mathrm{d}\lambda \mathrm{d}\Omega} = \left(\frac{\mathrm{d}I}{\mathrm{d}\lambda \mathrm{d}\Omega}\right)_1 \left\langle \left| \sum_i e^{-i\vec{k}\vec{r_i}} \right|^2 \right\rangle \tag{1.4}$$

where $\left(\frac{\mathrm{d}I}{\mathrm{d}\lambda \mathrm{d}\Omega}\right)_1$ is the energy density of the reference charged particle. For a large number of particles, we can approximate the bunch by a continuous distribution, and assuming that all of them are uncorrelated, the continuous limit is

$$\frac{\mathrm{d}I}{\mathrm{d}\lambda \mathrm{d}\Omega} = \left(\frac{\mathrm{d}I}{\mathrm{d}\lambda \mathrm{d}\Omega}\right)_1 [N + N(N-1)|F(\lambda)|^2] \tag{1.5}$$

where N is the number of particles and $|F(\lambda)|$ is the longitudinal form factor. The linear term in N describes the incoherent radiation contribution, while the quadratic term is the coherent part [3]. For a number of particles in the bunch that is very large ($> 10^8$), the quadratic term will dominate and therefore the emission is expected to be largely coherent.

In longitudinal bunch diagnostics based on coherent radiation spectrum analysis, it is the form factor $|F(\lambda)|$ that is calculated from the experimental data. It is related to the longitudinal particle distribution $S(z)$ through the equation

$$F(\lambda) = \int_{-\infty}^{\infty} S(z) e^{2\pi i z/\lambda} \mathrm{d}z \tag{1.6}$$

and the final objective is to calculate the quantity . In theory, a Fourier transform of the above expression should suffice. In practice however, there are a number of problems that arise which can make the process considerably less trivial. Two of them are discussed below.

The first problem is that the modulus of the form factor is usually known only for a limited number of frequencies, and this will require us to extrapolate these, to generate an essentially continuous expression. In performing this extrapolation, one can use sensible approximations known at the time of experiment, such as the hypothesis of a single gaussian beam of unknown longitudinal length. However such an approximation constrains the type of spectrum that can be obtained.

The second problem we face is that, the calculation of the Fourier transform to get requires knowledge of the phase. But the phase is unknown, and as a result, it is necessary to set up a strategy to estimate it sensibly, and then insert it into the mathematical Fourier expression,

then only we will have found . As it was mentioned there are a number other problems but the two above are the most critical.

The properties of coherent radiation described above are very general. Coherent radiation itself can be caused by a wide range of phenomena, and in the area of bunch length diagnostics, three main families are routinely encountered in linear accelerators.

A first family is the coherent transition radiation. It happens when charged particles go through the boundary of two media of different dielectric characteristics. This well-known process has a wide range of applications depending on the frequency range considered: in the optical/far-infrared regions, it is usually used for beam diagnostics [5], while in microwave range it is mostly used for coherent generation [6], and, at X-ray wavelengths, it is used for particle detection [7]. The incoherent part of transition radiation has also been used to calculate the transverse dimensions of an electron bunch [5],[8], [9]. Bunch diagnostics methods based on transition radiation are obviously destructive for the bunch and are therefore not ideal if we wish the beam to remain unaffected.

Another family of interest is coherent diffraction radiation. It happens when a bunch of charged particles , passes at the vicinity of a material such that the impact parameter x_0 satisfies :

$$x_0 = \lambda \frac{\gamma}{2\pi} \tag{1.7}$$

where γ is the usual relativistic parameter.

Unlike the transition radiation, which is emitted by the particles themselves, the diffraction radiation is an emission that originates from the boundary involved, such as an aperture or border material. It is possible to describe the phenomena with the familiar scattering formalism of photons created on the target surface [10]. Interest on the possibility to use diffraction radiation to determine the longitudinal bunch length started in 2001 at Fermilab [14] at low energies ranging from a few dozens to a few hundreds of MeV, and went a stage further in 2004 with measurements of an 8 mm bunch length at 1.28 GeV at KEK test facility

[15].

A third family is the Smith-Purcell radiation, which I have considered for the project and presented in this thesis. Coherent Smith-Purcell Radiation happens when an electron bunch travels above a metal periodic structure. The effect was experimentally detected in 1953 at Harvard, in the optical range [16]. The coherence condition implies that in the far field, the detected wavelength is related to the angle of observation through the following expression:

$$\lambda = \frac{l}{m}\left(\frac{1}{\beta} - \cos\theta\right) \tag{1.8}$$

In the above expression, l is the period of grating along the direction of propagation, m is an integer that stands for the order of radiation, and β is the electron beam relative velocity with respect to the speed of light c. The angle θ is referenced with respect to the direction of propagation so that high angles correspond to a backward direction while small angles are directed forward.

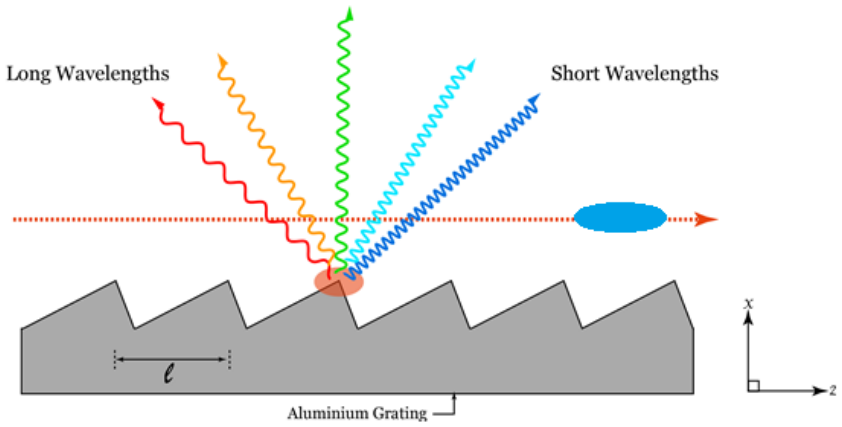

Figure 1.1: Schematic of electron beam propagating above the grating and excitation of Smith-Purcell radiation.

1.3 Interest and motivation of Smith-Purcell studies

In this thesis, we will focus on a thorough study of experimental and numerical aspects of coherent Smith-Purcell radiation. The context will be the measurements and analysis of

data taken at highly relativistic regime at femtosecond scale. Attempts have been made in the past to use transition and diffraction radiation as diagnostic tools at such regimes, but with limited success and difficulty to overcome some challenges: for example, transition radiation has been used at energies up to 30 GeV at SLAC, as successful measurements in 1999 took place for longitudinal bunch sizes down to 170 fs. However the apparatus used is very expensive, and its design does not accommodate future size accelerators which will require the measurements of much smaller bunch lengths. Transition radiation has several inherent problems such as difficulty to take into account properly the effects of background radiation or measure frequencies below 1 THz. In addition, because of the requirement of using thin foils to create the transition radiation, there is also the problem of degradation of the material with regular replacement of the foil and the heat loss generated. As for coherent diffraction radiation, similar issues arise with respect to the measurements of short bunch lengths, but with additional problems because there is currently no satisfactory method to take into account the presence of background radiation.

Compared to transition and diffraction radiation methods, the Smith-Purcell radiation offers a very cost-effective, non-invasive way to perform bunch length diagnostics, and with a proven technique to subtract the background radiation properly when it is present, as it will amply be shown in this thesis.

To understand the potential of Smith-Purcell radiation, let us have a look at the table 1.1. It gives an outline of the requirements of some major accelerators, either existing, or still in the stage of design project: we can see on that table that at FACET II and LCLS II, which are the not-yet active upgrade projects for FACET and LCLS respectively, the design aims at longitudinal bunch length as ultra-short as 2 fs/ 3fs under maximal compression. At such distances, the design reports recommend the use of transverse-deflecting cavities, but they have the disadvantage to be destructive for the beam. Such transverse-deflecting cavities have also a prohibitive cost which make other smaller labs unable to afford them.

The fact that Smith-Purcell-based diagnostics are cost-effective and non-invasive is thus a considerable driving motivation. One of the reasons why the use of Smith-Purcell radiation

Table 1.1: Nominal bunch length of some major accelerators

ILC	500 fs
CLIC	130 fs
XFEL	80 fs
LCLS	75 fs
LCLS II	27 fs [2 fs - 175 fs]
FACET	100 - 1600 fs
FACET II	3.3 fs - 66.6 fs

Table 1.2: Bunch lengths successfully measured using coherent Smith-Purcell diagnostics

ENEA FEL	Frascati, Italy	2000-2002	14-16 ps
FOM	Utrecht, Netherlands	2005-2006	1-3 ps
FELIX	Nijmegen, Netherlands	2006	5-6 ps
ESTA	SLAC, USA	2008-2009	2-3 ps
FACET	SLAC, USA	2011-2015	0.3-0.7 ps

as a diagnostic tool seems so promising is that it has been researched for some time and was detected at many different accelerator facilities using beams with very different parameters.

The table 1.2, shows the accelerators and research laboratories where the Smith-Purcell ra-

diation has been studied. Initial successful results were obtained in Oxford and published in 1992, and were investigating the possibility to use it as an inexpensive and compact free-electron laser [11]. From the early 2000's, increased interest came to Smith-Purcell radiation not only in the scope of free-electron lasers but also specifically as diagnostic tool, when it became clear that it had the ability to resolve bunch lengths of sub-ps dimensions. This is illustrated in the table 1.2, where in the decade 2000-2010 it has been used at FOM, FELIX and SLAC specifically to study the possibility to use SP radiation for diagnostics. An important point to be mentioned, is that despite all the very different accelerator environments listed in Table 1.2 where the experiments have been performed, the Smith-Purcell apparatus has undergone minimal changes, usually to accommodate the local data acquisition system available, as well as the space constraint. At the current stage, one can state that we have always been able to measure smaller and smaller bunch dimensions without being failed by the choice of Smith-Purcell as a method. Therefore it is sensible to speculate that we have not identified yet the experimental limit of bunch dimensions that cannot be resolved anymore. Consequently, this provides a very strong motivation for studying Smith-Purcell radiation in the context of future accelerators in mind. Now, as indicated in the Table 1.2, this thesis focuses on the work carried at FACET, SLAC, (Stanford, USA). More will be said on that experimental facility in the Chapter 4. The actual experimental work that I performed, has taken place from 2013 to 2015 and dealt with sub-picosecond scales, that is, essentially in the THz and GHz ranges. This leads us to another of the major motivations to study Smith-Purcell radiation, which is the general context of THz generation and THz studies. THz studies have applications that go far beyond the scope of just accelerator science: at FACET for example, the THz radiation produced is extracted and redirected into other facilities where it is used to study the behaviour of materials in presence of intense field, or for biological imaging. Properties of THz radiation are also studied for themselves by particle astrophysicists at SLAC, as 50% of the cosmic microwave background (the remaining radiation in the deep space that originates from the big bang) is of THz nature, with anisotropic substructures that go down to femtosecond-scale. Recent use of sub-picosecond to femtosecond signals include biomedical imaging for high-resolution cell analysis and skin

cancer detection using pulses of 230-250 fs longitudinal length [12].

1.4 Structure of this work

In the Chapter 2, we will first develop the theoretical framework called the surface-current theory. It is a far-field description that models the cSP radiation within certain approximations and assumptions, and will provide us a guideline of interpretation across this work. The idea of a surface-current to explain the Smith-Purcell radiation dates back to their original paper in 1953 where they suggest the idea of *"surface charge moving across a grating"*. Despite this, a satisfactory mathematical model based on the surface-current idea only came in the late 1990's.

The results described in the chapter 2 will be provided from a computer semi-analytical implementation. A comparison will be presented with particle-in-cell results that describe the behaviour of fields in the vicinity of the beam, to understand up to what extent the near-field and far-field manifestations of cSPR can relate to each other.

We have to realize that the methodology of chapter 2 for a theoretical study is the exact opposite of what we do in a real experiment: in the chapter 2, we assume the knowledge of the bunch length, and we deduce the physical quantities such as spectrum etc., while in a real experiment, we perform the measurements and we deduce the bunch length. As explained previously, going from measurement to the calculation of bunch length, will require a suitable method to estimate the phase. This will be the topic covered in the chapter 3.

In the chapter 3, a new algorithm called "PCI algorithm" (Phase-Constrained Iterations algorithm) will be considered. It has revealed itself to be very promising when applied to our measurements. The PCI algorithm is, in essence, a meta-algorithm, that is, a combination of smaller algorithms. In the previous literature, two well-known problems of phase retrieval is that iterative algorithms do not usually provide a unique solution even if repeated with the same set of parameters, and non-iterative techniques like the Kramers-Kronig minimum phase method , often yield profiles with some non-physical features, such as oscillations that

reach negative values. The major progress of the PCI algorithm, with respect to previous iterative techniques, is that it provides a most probable solution , and a bunch profile which is rigorously physical because it has no negative values. This is achieved by constraining the iterative computations by boundary conditions known from the Kramers-Kroning relation, and using the latter also as initial condition at the start of iterative process.

The experimental studies conducted during the project including experimental set-up description and results are presented in the chapters 4 and 5. The chapter 4 will be dedicated to the description of the experimental apparatus of the E203 ("Experiment 203") research at SLAC, the linear accelerator operated by Stanford University. Although E203 has run from 2011 to 2015, the work presented here will deal only with the 2013-2015 period, which corresponds to my thesis contribution. The operational parameters of the beam delivered for the bunch diagnostic experiment such as charge, emittance, etc. will also be described in the chapter 4. The chapter 5 will follow with the presentation of the main results obtained in the various runs undergone. It is articulated across three topics:

- First, and most importantly, will be presented the results on longitudinal profile measurements. The bunch length will be defined as the full-width at half maximum of the retrieved profile, at 10% cut-off of normalized maximum amplitude. This will ensure comparison with the other bunch length diagnostics at SLAC, who adopt the same definition. The results of Smith-Purcell radiation measured in various conditions will be described: various compressions, various beam-grating separations. An important result that will be shown is the fact the bunch length of the profile retrieved is independent of the beam-grating separation. This will have two consequences: it will support the consistency of using the Smith-Purcell as diagnostic tool, and it will support the use of surface-current model as valid theoretical framework.

- The second and third part of the chapter 5 will be dedicated to the investigation of two other aspects of Smith-Purcell radiation for which only limited research has been performed in the past: its azimuthal distribution and its polarization properties. The azimuthal distribution has never been studied experimentally before, while polarization

has been studied only marginally. Here again, the predictions from the surface-current model, will generally fit the observed measurements within experimental errors, but it will be shown that in some cases, the agreement is not always very satisfactory. This suggests a possible room for improvement of the theoretical model in a future work. The azimuthal distribution analysis presented in this thesis will be meant to be reasonably complete, while the polarization study is actually more of a contribution: this is because only a few frequency channels have been studied at SLAC, and therefore the work should be complemented with an extended investigation.

The chapter 6 will conclude this thesis by discussing possible future works as well as how the use of coherent Smith-Purcell radiation can be extended further, as a diagnostic tool in a single-shot design, but also as candidate for THz generation source in strong regimes. In the light of the results obtained through the E203 experiment, I shall also take the opportunity to discuss the identified limitations of the surface-current model and motivate deeper theoretical investigations of properties such as polarization. Improvements of reconstruction method or alternative ones will also be suggested.

Chapter 2

Theory and simulations

2.1 Algorithms used in theoretical studies

2.1.1 The far-field: the surface-current model

The surface-current theory is a relativistic implementation of the image-charge model developed in the late 90's [17]. The interpretation of the resulting equations, presents the Smith-Purcell radiation as an emission of surface current from the grating when an electron bunch propagates above the surface of the grating, as seen in the figure 1.1 . The surface current theory is still under development and the thesis is part of the effort to describe the coherent SP radiation. The formulas and terminology used in the thesis are adopted from [18] and follows the conventions and principles developed in that paper. At first we consider a model of cSPr generated by a single electron of charge e . Assuming it propagates with a velocity v at a distance x_0 from the grating (impact parameter), the surface charge σ on the grating, due to the electron's field E is given by:

$$\sigma = \frac{2\,E}{4\,\pi} = \frac{\gamma\,e\,x_0}{2\,\pi[x_0^2 + y^2 + \gamma^2(z - v\,t)^2]^{\frac{3}{2}}} \tag{2.1}$$

In the above formula, γ is the relativistic parameter defined by $\gamma = (1 - \beta^2)^{-\frac{1}{2}}$, and x is the vertical coordinate perpendicular to the grating, along which the impact parameter is

defined. As for the other coordinates y and z , we define z as being parallel to the direction of propagation of the electron, while y will be the transverse direction. This is illustrated in the figure 2.1 below:

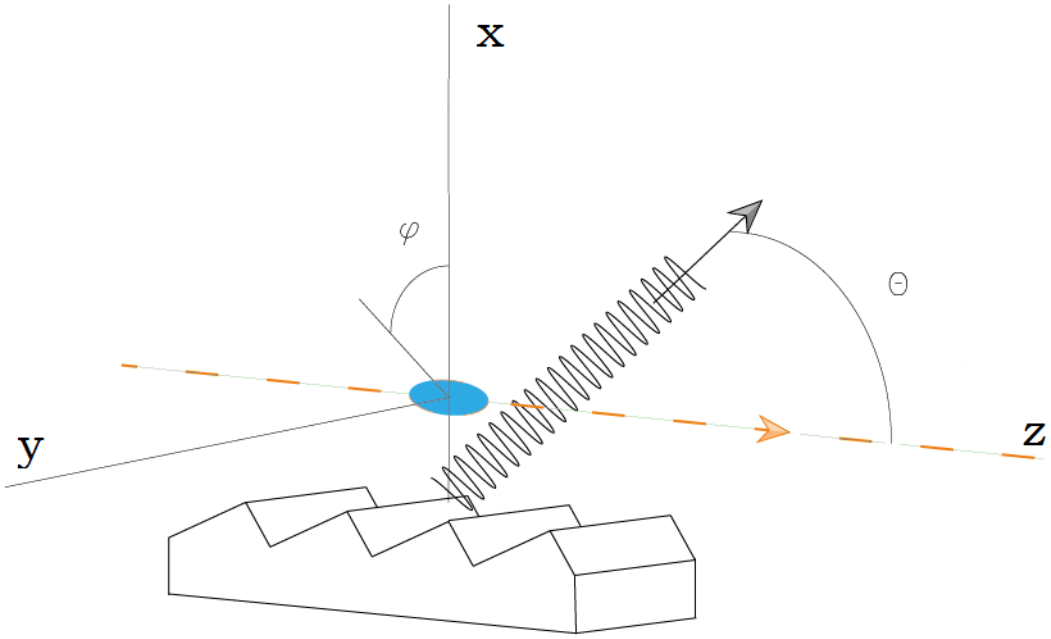

Figure 2.1: Axis and angles for the surface-current model

Given the surface charge, the surface current density is then:

$$\overline{J} = \frac{\gamma\, e\, x_0\, v}{2\,\pi[x_0^2 + y^2 + \gamma^2(z - v\,t)^2]^{\frac{3}{2}}}(\tan\alpha_1, \frac{y}{x}\tan\alpha_1, 1) \tag{2.2}$$

This expression for $\overline{J}$ is then substituted in the expression for radiation generation by currents [19]

$$\frac{\mathrm{d}^2 I}{\mathrm{d}\omega \mathrm{d}\Omega} = \frac{\omega^2}{4\pi^2 c^3}\left|\int_{-\infty}^{\infty} \mathrm{d}t \int \overline{n} \times (\overline{n} \times \overline{J}) \exp[i\omega(t - \frac{\overline{n}\overline{r}}{c})]\mathrm{d}y\mathrm{d}z\right|^2 \tag{2.3}$$

where $\overline{r}$ is the position coordinates of a particular induced charge, and $\overline{n}$ is the direction of observation. Once the $\overline{J}$ substitution is performed, follows an integration over the coordinates and over ω. Finally one obtains an expression for the differential energy $\mathrm{d}I$ per solid angle $\mathrm{d}\Omega$ for a single electron:

$$\left(\frac{\mathrm{d}I}{\mathrm{d}\Omega}\right)_1 = 2\pi\, e^2 \frac{Z}{l^2} \frac{n^2\,\beta^3}{(1-\beta\cos\theta)^3}\, R^2 \tag{2.4}$$

– Z is the grating length

– R is the "grating efficiency", also called "radiation factor". It is a function of the grating profile, radiation angle, the radiation order, and the beam-grating separation x_0 :

$$R^2 = |\overline{n} \times (\overline{n} \times \overline{G})|^2 \tag{2.5}$$

Here, $\overline{n}$ is a unit vector perpendicular to the integrated facet, and G is a complex vector which is a sum running over all of the N facets of the gratings, and indexed by the letter j:

$$\begin{cases} \overline{G} = \sum_{j=1}^{N} \overline{G}_j \\ \overline{G}_j = (\tan\alpha_j, 2ik_y\lambda_e \tan\alpha_j, 1) \exp\left[\left(\frac{1}{\lambda_e} - ik_x\right) x_{j1} + i\left(\frac{k}{\beta} - k_z\right) z_{j1}\right] \frac{\exp[iD_j(z_{j2}-1)]}{iD_j\, l} \end{cases} \tag{2.6}$$

where:

– The quantity λ_e is the evanescent wavelength, and describes the coupling between the bunch length and the grating. Its explicit expression is given by

$$\lambda_e = \frac{\beta\gamma\lambda}{2\pi\sqrt{1+\beta^2\gamma^2\sin^2\theta\sin^2\phi}} \tag{2.7}$$

– The complex quantities D_j 's are given by

$$D_j = \frac{k}{\beta} - k_z - k_x\tan\alpha_j - i\frac{\tan\alpha_j}{\lambda_e} \tag{2.8}$$

– The coordinates (x_{j1}, y_{j1}) and (x_{j2}, y_{j2}) are the running beginning and end coordinates across each j-facet out of the N.

– The angles α_j's can be the grating angle, counted with a positive sign, or its 90-degrees complement, to take into account the downward side of the facet in the numerical integration, in which case the angle will carry a negative sign. For a blazed grating, our choice for will be 30 degrees, and its 90-degree complement for the second facet of the grating is thus 60 degrees.

Usually, an analytical form for the grating efficiency R can be obtained only for simple configurations, such as like square grating, and even then, the calculation is far from trivial [17]. For more complicated shapes, such as blazed grating, no analytical solution is known and R must be computed numerically. The choice of a suitable grating type in order to optimize the radiated energy has been studied in the past and, in line with all the previous work, the appropriate chosen geometry in this thesis will be blazed gratings [18] .
Based on the single electron yield formulation, it is now possible to use the general theory of coherent radiation, to extend the single electron case to an electron bunch. Here the total EM wave yield will depend on the square of the number of particles N and the coherent contribution S_{coh} :

$$\left(\frac{\mathrm{d}I}{\mathrm{d}\omega}\right)_{\mathrm{sp}} = 2\pi q^2 \frac{Z}{l^2} \frac{n^2\beta^3}{(1-\beta\cos\theta)^3} R^2 \exp\left(-\frac{2x_0}{\lambda_e}\right) N^2 S_{coh} \tag{2.9}$$

This last expression illustrates the meaning of the evanescent wavelength λ_e : the factor $\exp\left(-\frac{2x_0}{\lambda_e}\right)$ showing that the signal intensity decreases exponentially with the increase of beam-grating separation. The formula also shows that this decrease depends on the value of the evanescent wavelength taken in (r, θ, ϕ) and in this sense, $1/\lambda_e$ can be considered as a description of the effective beam-grating coupling.

Based on all the previous equations, the surface-current simulations presented here have been performed using a semi-analytical C based, code GFW (for “Grating of Finite Width”)

written by Dr George Doucas using Numerical Algorithms Group company (NAG) subroutine library [18].

2.1.2 The near-field: particle-in-cell simulation

Another approach can be used to study theoretically cSPr. This approach based on numerical studies using Particle-in-cell software. It implements directly a self-consistent set of Maxwell equations with complex boundary conditions and will be used to gain some insight on the near-field behaviour of the radiation. It is well-known that Maxwell Equations can be successfully implemented numerically using one of three types of simulations:

- The FDTD method (finite difference time domain): here, the domain is constructed as a grid on which the fields are calculated, and updated through time as the simulation progresses.
- The boundary element methods: the problem is reformulated as a set of integral equations.
- The finite elements methods: this is used for highly industrial simulations where FDTD methods are computationally ineffective.

In the case of Smith-Purcell radiation, both FDTD and BEM methods have been the methods of choices for numerical investigations through the literature. Most commercially available PIC codes tend to use algorithms defined in an FDTD framework because they are mathematically easier, and are computationally more effective. They also provide better convergence and can easily be optimized for parallelized programming. In this PhD I have used the commercial code *VSim*, formerly known as *VORPAL* until its release 5.X, and developed by Tech-X Corporation, which is designed for FDTD-types simulations. In practice, due to the high resolution required, conducting simulations in the far field is not feasible and in this thesis all numerical studies were conducted in the near field. This limits studies to certain properties, such as the spectrum or polarisation, which can be compared quantitatively

between the semi-analytical and numerical models. I will start first with the determination of the cSPr spectrum generated by grating in a two dimensional system, which can be achieved even with limited computational power. I have also performed 3-D simulations for finite width grating to have a qualitative idea of the directionality of the radiation along the azimuthal coordinate. It should be noted that, unsurprisingly, 3D simulations require a very high computational power (ideally, more than 1000 cores), but despite this , small-scale directionality studies (conducted experimentally in the last year) which require 3D simulation led to qualitative data and can be considered as a contribution to be complemented with future work. The power of particle-in-cell simulation with *VSim* comes from the combination of an optimized meshing called the Yee Mesh, along with the well-known algorithm called the leap-frog algorithm. The so-called Yee mesh, was described in 1966 by Kane S. Yee [20]. It describes the division of the grid which has the structure presented in the figure 2.2: the domain is divided into cubes. At the centre of each cube-face, there is an associated index of the magnetic field, while the electric field is calculated at the centre of each vertex. This means that, at first, E and H are not known in the same points in this cubic structure. Since we need to have values for E and H in all coordinates to describe the dynamics, the missing E and H are reconstructed by the electromagnetic solver as spline interpolation. The Yee mesh is provided by *VSim* and does not need to be programmed, except for its dimensions.

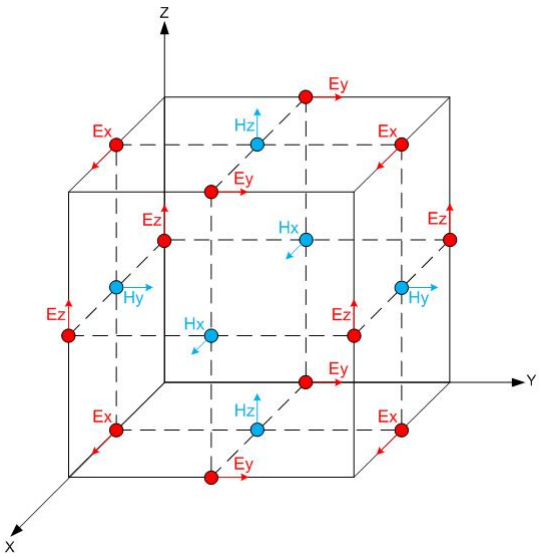

Figure 2.2: Structure of the Yee Mesh. The magnetic field is calculated on the centre of cube faces, and the electric field is calculated on the centres of cube vertices. (Creative Commons image, please see Declaration page for the source)

The Yee-Mesh defines only the grid but can accommodate several computational techniques to solve the dynamics. The one I implemented is the leap-frog algorithm. It calculates the time evolution of the electric and magnetic fields according to the following mechanism:

- A field is started to be solved at $t = 0$ (for example, E)
- That field will be solved at all subsequent integer step time-intervals $\mathrm{d}t$ of the simulation
- The other field (for example, H, if we have previously chosen E) will be solved at all half-steps of the simulation

This means that, if E is calculated through the grid at the times

$$t = 0,\ \mathrm{d}t,\ 2\mathrm{d}t,\ 3\mathrm{d}t...$$

then H will be solved at the times

$$t = 0.5\,\mathrm{d}t,\ 1.5\,\mathrm{d}t,\ 2.5\,\mathrm{d}t...$$

At each step, *VSim* then solves the Ampere's law and Faraday's law. Poisson and Gauss equations are taken into account as initial conditions, and this is sufficient to make the simulation consistent from the dynamics point of view. The boundary conditions of the simulations are defined by:

- A *perfectly matched layer* (PML): this is a layer that surrounds the whole physical simulated regions and ensures that the fields are absorbed and do not reflect back as parasitic signal. The fields arriving at the PML decrease exponentially very rapidly within that layer and are not recalculated when reaching the border of the simulation. PML features are essential: if a PML is not defined, the default particle-in-cell behaviour will be to recalculate the dynamics at the border of the simulation, which will lead usually to a certain amount of signal reflection. In *VSim*, the PML is defined in terms of "width", that is, the "number of cells" of the layer of the PML, whose size are the same as the non-PML cells. *VSim* provides the possibility to use non-PML boundary conditions called MAL, but those are licensed and acts as a black-boxes, hence I chose the PML, which have the advantage to be well documented in the literature.

- An outer *absorbing box*: to ensure that the electrons arriving at the border of the simulation disappear. The absorbing box can usually embed the PML layer and is defined through a macro, hence the programmer has no work to do apart from defining it.

2.2 The Smith-Purcell spectrum

I developed the initial version of the code using the release 5.2 of *VSim* code on 512 cores (Juropa supercomputer at Jülich, Germany), during the academic year 2012-2013. Then the version 6.0/6.2/6.8 versions of *VSim* were used on 64 cores of the Arcus cluster of the Oxford Advanced Research in Computing (ARC) facilities for the year 2013-2014, then using the versions 7.0/7.2 of *VSim* on 64 cores of the John Adams Institute cluster for the 2014-2016 period. The radiation from gratings of three different periods: 250 microns, 500 microns

and 1500 microns were studied. The core numerical model was a 2 dimensional (2D) grid of 10 mm x 20 mm and a resolution of 5.10^{-6} cm per cell side. An electron bunch of 300 fs of full-width half maximum propagates at 2 mm above the grating with an energy of 20 GeV. Absorbing boundary conditions for the electrons as well as for the electromagnetic fields were set to avoid reflections, and the simulation was run for 20000 timesteps with a time-step of 8.10^{-15} seconds at each iteration.

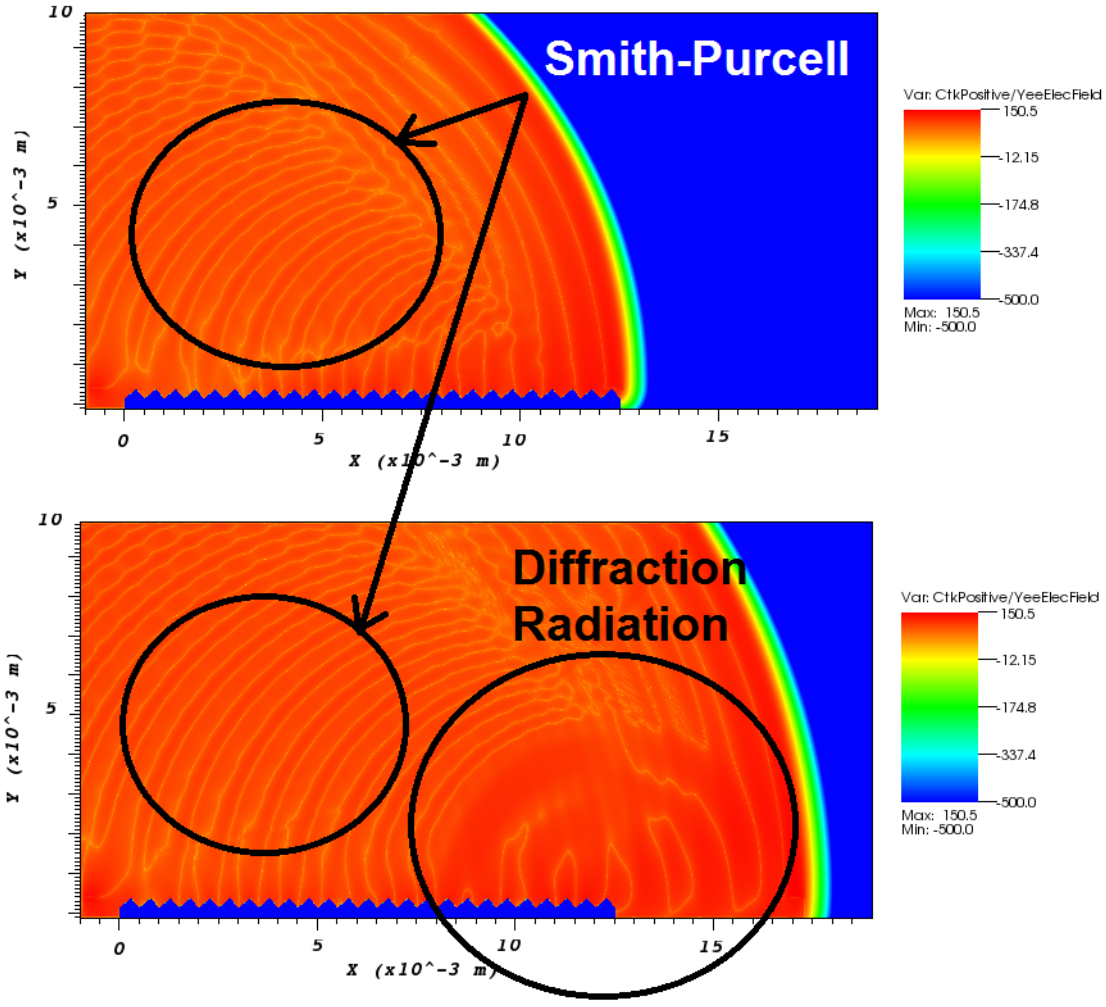

Figure 2.3: Observed Emission before and after the bunch reaches the end of the grating. The diffraction radiation is clearly visible on the bottom plot.

In the figure 2.3, the dynamics of the simulation is illustrated. The upper inset of 2.3 shows the radiation before the bunch arrives at the end of the grating, and the lower inset shows the radiation just after the bunch has left the grating area. The diffraction radiation from the

edge is clearly visible, and constitute an unwanted source of parasitic background radiation. To isolate the Smith-Purcell radiation only, such diffraction effects must be eliminated. This is done by running the simulation twice:

- A first simulation is run with the electron bunch moving above a regular grating
- A second simulation is run with the electron bunch moving above a flat substrate called "blank".

The subtraction between the two results will provide the contribution from the grating teeth only: this will be the Smith-Purcell radiation. We shall see in the chapters 4 and 5 that in the actual experiment, the Smith-Purcell radiation is also extracted by subtraction of the radiations emitted from a grating and a blank. A difference between simulation and experiments, is that simulations account for background radiation caused by diffraction from the edges while in a real experiment, other sources of background radiation might be present: they can still be removed by performing a subtraction with a blank, but they cannot be simulated. It is worth noticing that in the figure 2.3, we can see that the PML have been properly implemented, as no reflection occurs at the borders of the simulation region.

The figure 2.4 shows the time dependence of the magnetic field at a specific point above the grating. It clearly shows the nature of coherent Smith-Purcell radiation. The number of main oscillations of the field is equal to the number of grating teeth. This is particularly noticeable in the 1500 microns case in figure 2.4, where the grating had only 10 teeth due to the limited size of the grid. In the three pictures shown in figure 2.4, the contribution of the diffraction radiation is clear through the display of two peaks, before the electron bunch reaches the grating area and when he leaves it. These results can be compared with the predictions from the surface-current theory. The comparison between the particle-in-cell yield and the surface-current theory prediction for the spectra, are illustrated for the three gratings in Figure 2.5. We see that each grating has a spectrum delimited within a frequency region, as it is expected from the dispersion relation. The 250 microns grating radiates mostly in a region that spans 0.5-2.5 THz, while the 500 microns grating spans a

core region of 0.2-2THz, as well as some residual radiation between 0.2-4 THz and the 1500 grating spans that goes up to 1THz only. In all these three cases, the predicted spectrum in the far-field is compatible with the ranges determined by the particle-in-cell model. Despite the fact that there is agreement between the spectrum predicted from the surface-current theory and the spectrum calculated with *VSim*, it should be noted that those two spectra are taken at different distances from the gratings:

- The spectrum extracted from *VSim* corresponds to the frequency of a near-field single point.
- The surface-current spectrum prediction corresponds to a set of far-field points for θ angles ranging from 30^o to 140^o.

The comparison however is possible at any point of the near field (considering that grating is large compared to the distance to the observation point) carry the same frequency content as the whole set of points in the far field. This can be understood by remembering that Smith-Purcell radiation associates each angular direction to a specific wavelength: as a result, far from the grating, a detector receives signal from a very narrow direction, while near the grating, a point receives signal from all angles.

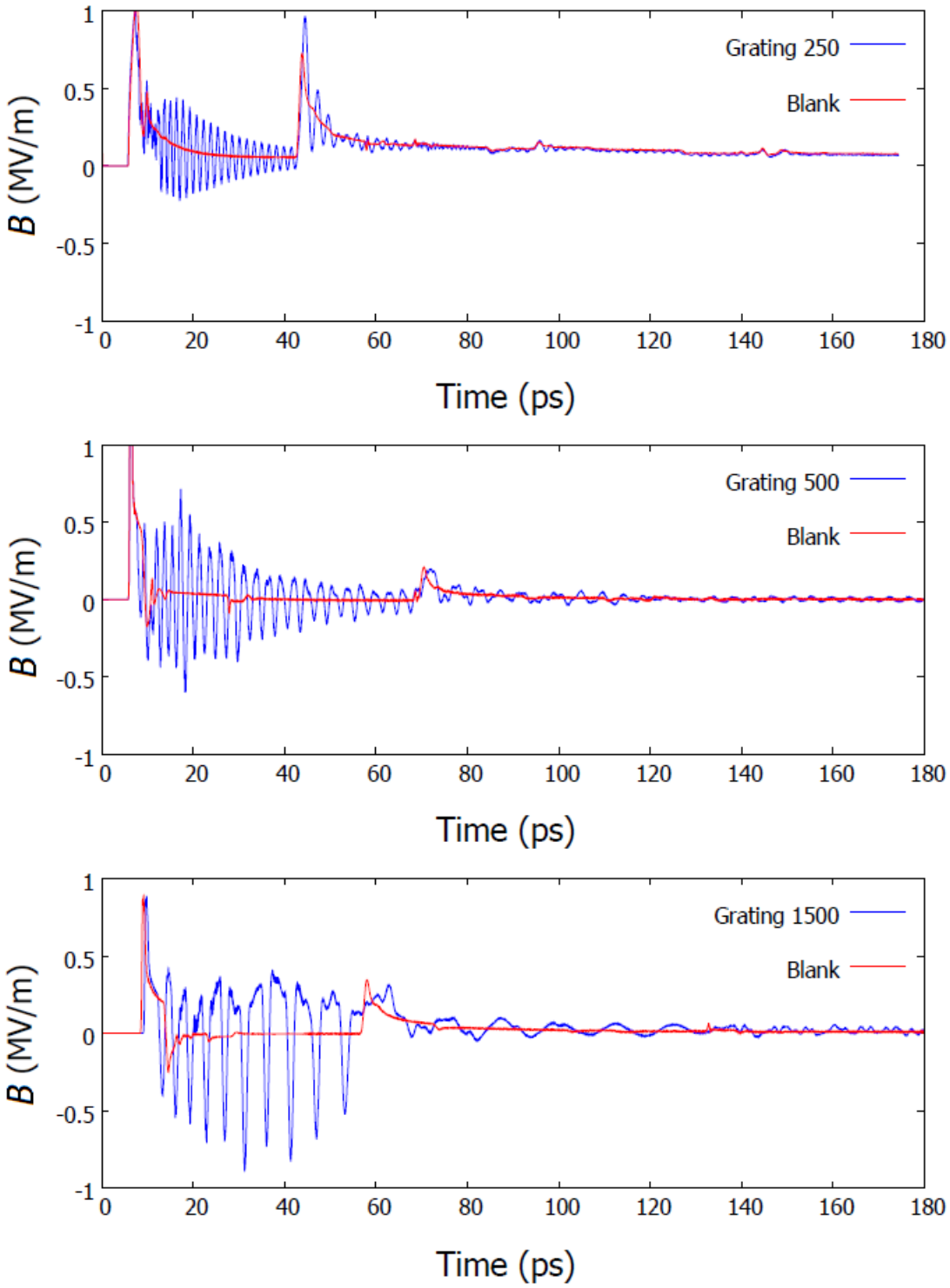

Figure 2.4: Time dependence of the particle-in-cell simulation of cSPR

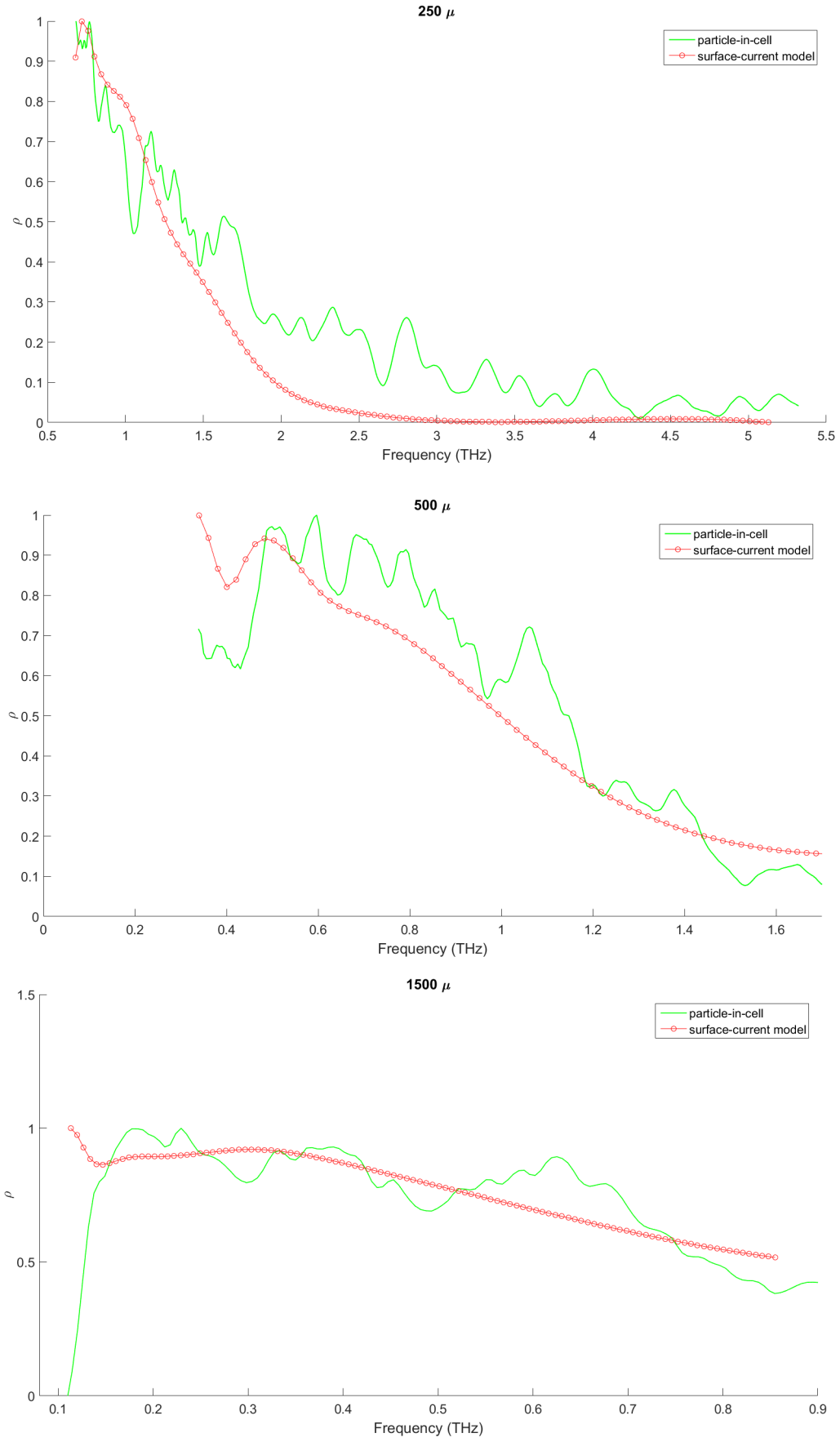

Figure 2.5: Comparison of the spectrum between the far-field yield according to the surface-current theory, and the near-field yield from the particle-in-cell simulation

2.3 Azimuthal distribution of the Smith-Purcell radiation

To the best of my knowledge, the analysis of both numerical and experimental of the azimuthal distribution of the cSPR that are as presented in this thesis, is the first study of cSPr generated by at ultra-relativistic electron bunches. The motivations for such a study are two-fold:

- First, having a clear idea of what one can expect through simulation will help better to embrace the potentials or limitations of the theory when confronted to experiments, and the comparison can be a guide of a possible further model improvements.

- Secondly, since the long-term aim of these Smith-Purcell studies is the design of a single-shot time profile monitor, it is important to have a good idea of the angular extension of the signal. This information will guide in setting the requirements of potential future designs.

Before describing the results, it is important to mention the fact that in this section, I present the simulations as deduced from the surface-current theory. As such, they do not account for device-dependent experimental aspects such as transmission factors, adaptation to the solid angle of a slit, etc. To avoid repetition, I put here the predictions from the semi-analytical simulation code GFW mentioned at the end of the section 2.1.1 , based on the theory only, while the GFW predictions taking into account our particular optical system will be presented in the experimental chapter results (chapter 5). This is consistent with the structure of the thesis, since all features of the optical system will be presented in the chapter 4 in the description of the experimental set-up. The beam parameters used for the simulations are given in the table 2.1:

Table 2.1: Parameters used in the simulation of the semi-analytical model

variable name	parameter
number of electrons	1.8×10^10
relativistic factor γ	40,000
normalized emittance	60 mm.mrad
fwhm in x	0.4 mm
fwhm in y	0.4 mm
radiation order	1
nominal bunch length	0.3 ps
beam-grating separation	2 mm

Let us first have a look at the predictions of the azimuthal distributions for the 1500 microns-period grating. The two figures 2.6 and 2.7 show the simulated yield in that case. The figure 2.6 shows a view-from-the top, while the figure 2.7 is a three-dimensional perspective. Because the GFW code implements directly the equations previously seen in [18], and is not an ab initio electromagnetic solver from Maxwell equations, a single simulation for the grating is sufficient, and no simulation needs to be performed with the blank. In these simulations, I have chosen an azimuthal extension of 3.5 degrees in ϕ . This is motivated by the fact that acceptance at entrance of the optical system receiving the signal (Winston cones, see chapter 4) is 6.1 degrees. The pictures below show that the radiated energy from the 1500-period gratings is within the 3.5 degrees and in theory, the full signal could be detected. A particular feature of these plots is the existence of a local minimum at $\phi = 0$ for almost all θ angles. These local minima are strongly pronounced between $\theta = 40$ and $\theta = 87$ degrees.

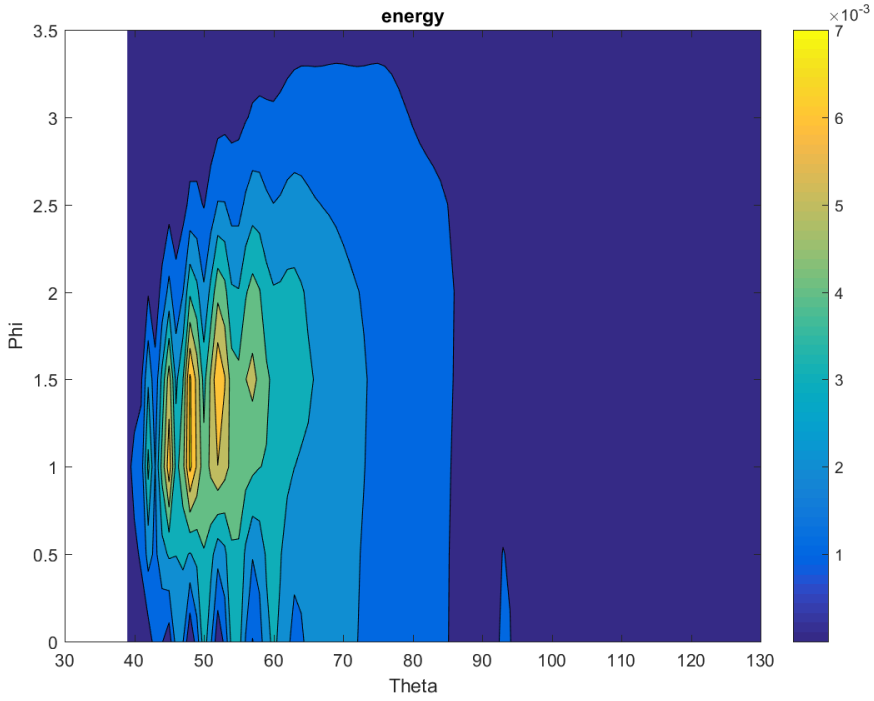

Figure 2.6: Surface-current prediction of azimuthal cSPR signal (1500-um period): view from top

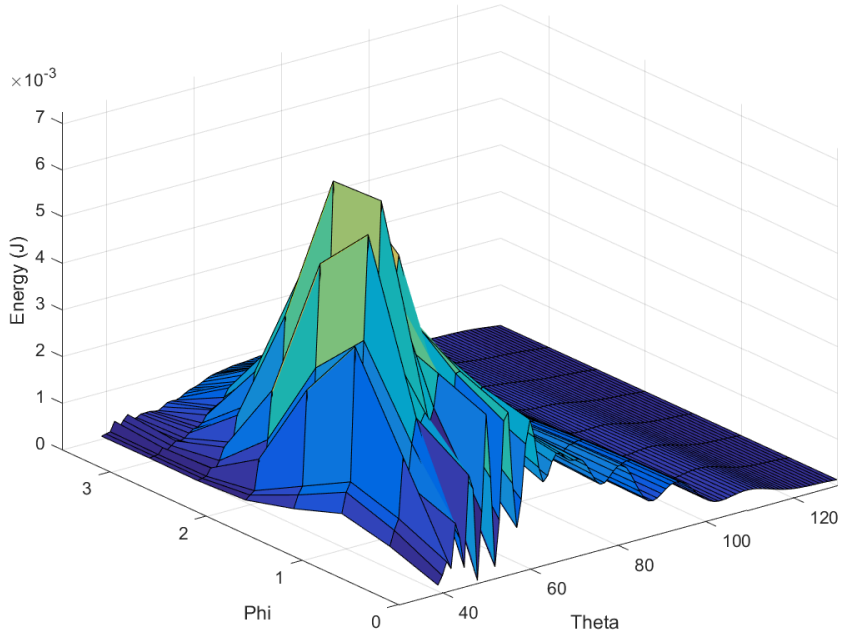

Figure 2.7: Surface-current prediction of azimuthal cSPR signal (1500 um-period): view from perspective

The predicted azimuthal distribution from the surface-current theory, in the case of the 500 microns period grating are shown in figures 2.8 and 2.9. The azimuthal extension changes significantly compared to the case of 1500 microns period: the whole signal is contained within just 2 degrees from either side of the bunch propagation trajectory. We also notice that the radiated energy has local spikes at $\theta = 44$ and $\theta = 52$ degrees, both at $\phi = 0.49$, but the overall signal across the domain is still mostly within the order of 10^{-3} J. Despite these quantitative differences, we still see that, like with the 1500 microns case, we also have a local minimum of the Smith-Purcell yield, as shown in the figure 2.9. These local minima in the middle therefore mean that the signal at those wavelengths has a double peak-structure because of the symmetry at $\phi = 0$.

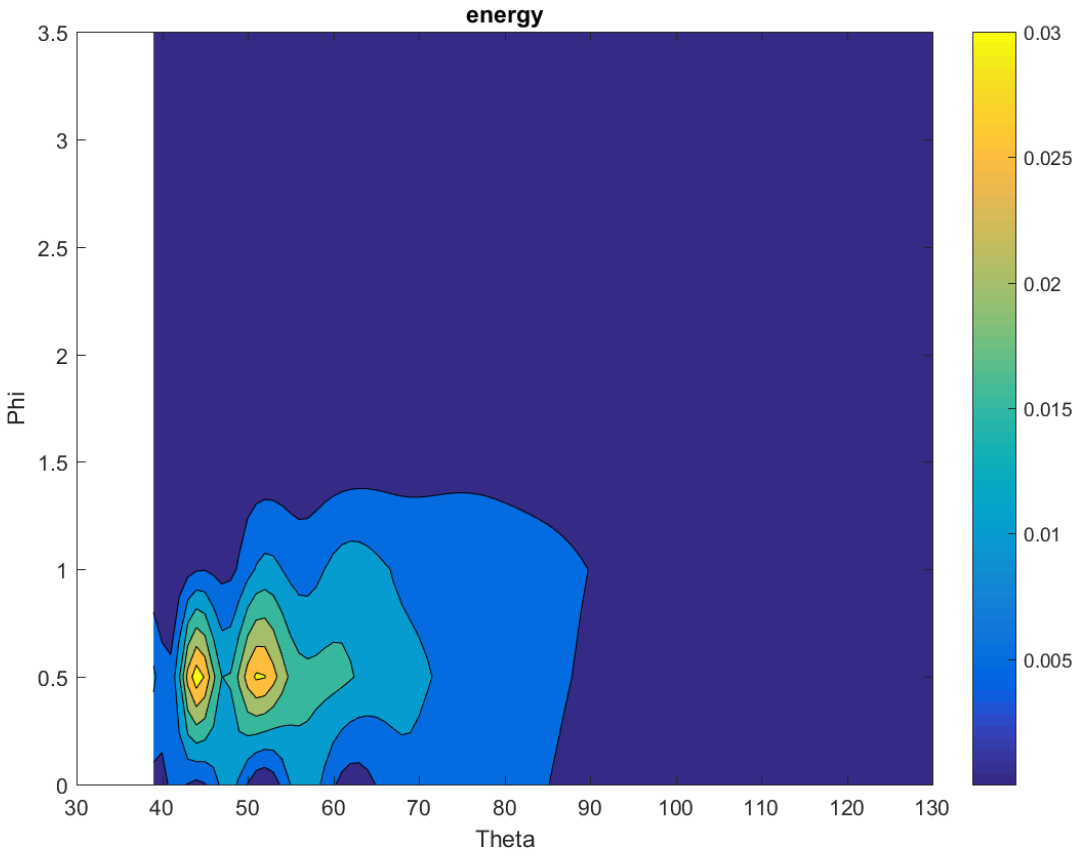

Figure 2.8: Surface-current prediction of azimuthal cSPR signal (500-um period): view from top

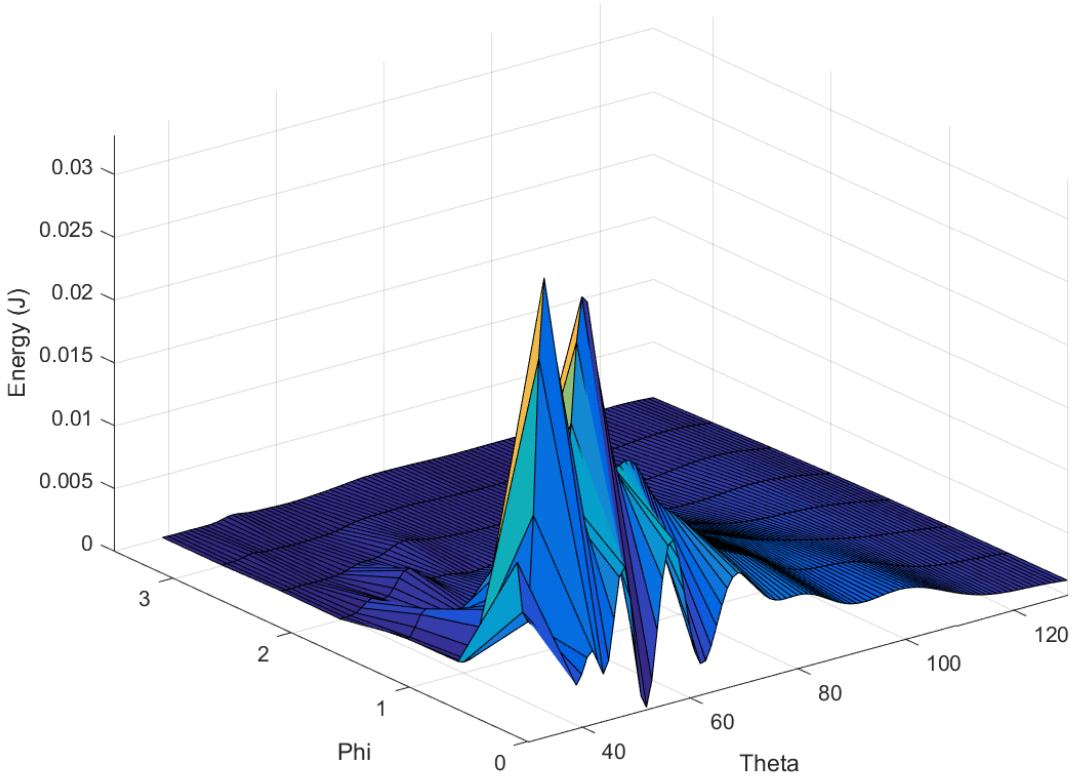

Figure 2.9: Surface-current prediction of azimuthal cSPR signal (500-um period): view from perspective

Finally, we can have a look at the predicted azimuthal signal from the 250 microns period grating. As the period of grating decreases, the simulations shows that here, the yield emission dominates at large angles, and again, the whole signal is essentially contained within $\phi < 2$ degrees. No obvious double-peaked structure seems to appear, this is because the drop to the local minimum at $\phi = 0$ is very small and not visible on the scale unless zoomed in.

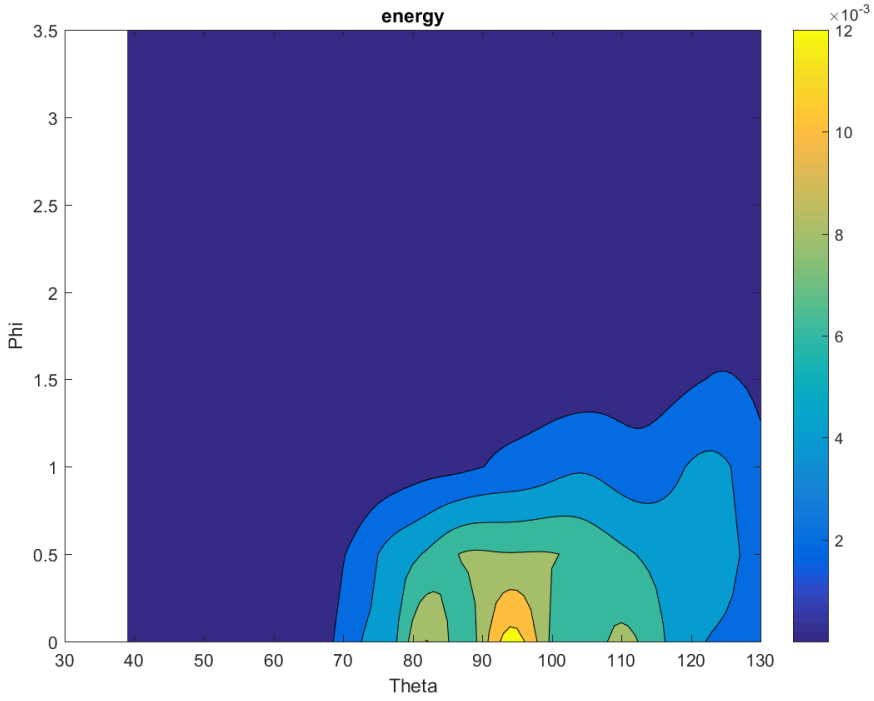

Figure 2.10: Surface-current prediction of azimuthal cSPR signal (250-um period): view from top

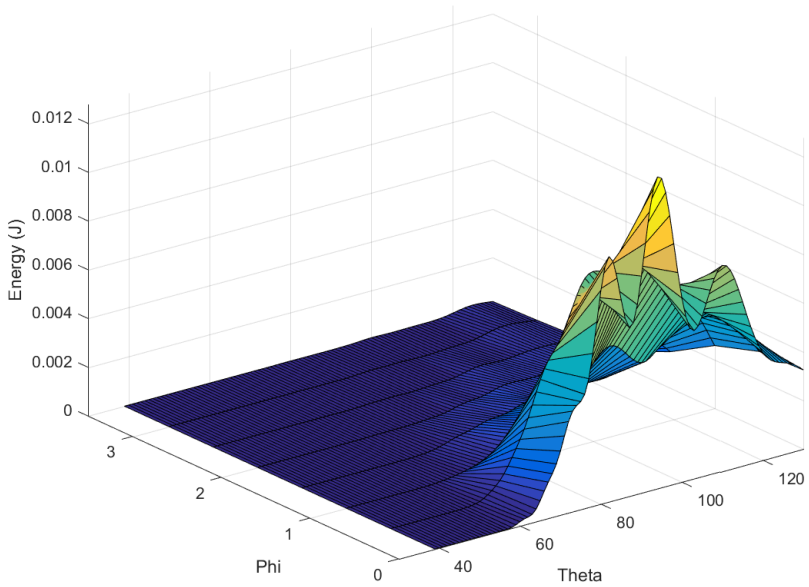

Figure 2.11: Surface-current prediction of azimuthal cSPR signal (250-um period): view from perspective

We can now turn to the results observed using particle-in-cell code *VSim*. As mentioned before, the observation point was located near the grating. The construction of three-dimensional simulations of coherent Smith-Purcell radiation is considerably more challenging. The larger domain increases the computational time and the PML requires much more memory. In practice, just running a 3D version of the 2D simulation used in the previous sections has been impossible: 1 GB was used for the computation of each iteration step, and a typical iteration step was requiring 24 hours using 64 cores. An actual 3D simulation would have actually required about 1000 cores. The only possibility was then to reduce the size of the simulation and the resolution of the Yee grid. But then comes the problem of being far away enough from the beam to detect Smith-Purcell phenomena rather than the evanescence surface waves located at the immediate vicinity of the beam. I have therefore chosen the following compromise: to keep a 10 mm x 10 mm longitudinal domain, with a 1 mm transverse domain. This has three advantages:

- It contains the whole information about the footprint of the Smith signal.
- The vertical size of the simulation is large enough to be far from the beam, and allows us therefore to obtain actual Smith-Purcell radiation instead of evanescent signal.
- The longitudinal extension allows to simulate the effect of a sufficient number of grating teeth to consider the overall radiation as being actually Smith-Purcell.

The figure 2.12 shows the results for a 3 dimensional simulation on a 500 microns period grating and a 1 mm beam-grating separation. The low quality of the images is due to the fact that neither *MATLAB* nor *VSim* is able to handle the slicing of the huge output of such simulations, due to the requirement of contiguous memory of .h5 dumps. I have thus post-processed the data using a separate software called *HD5view* and exported the results, which are shown below.

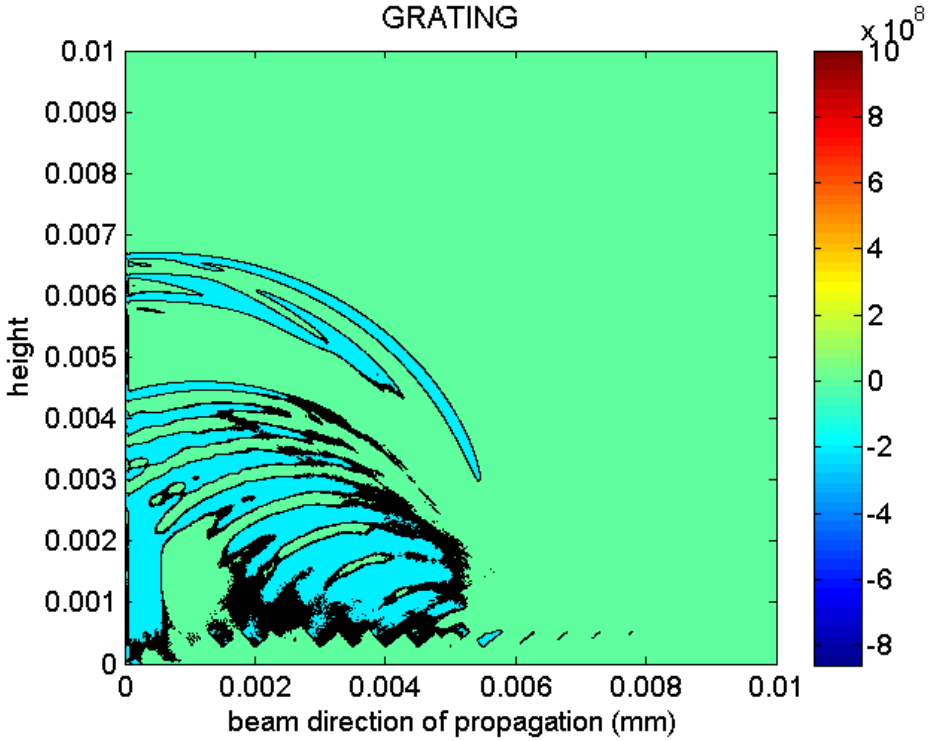

Figure 2.12: The electric field of a 3D simulation on a 500 um-period grating, for the grating

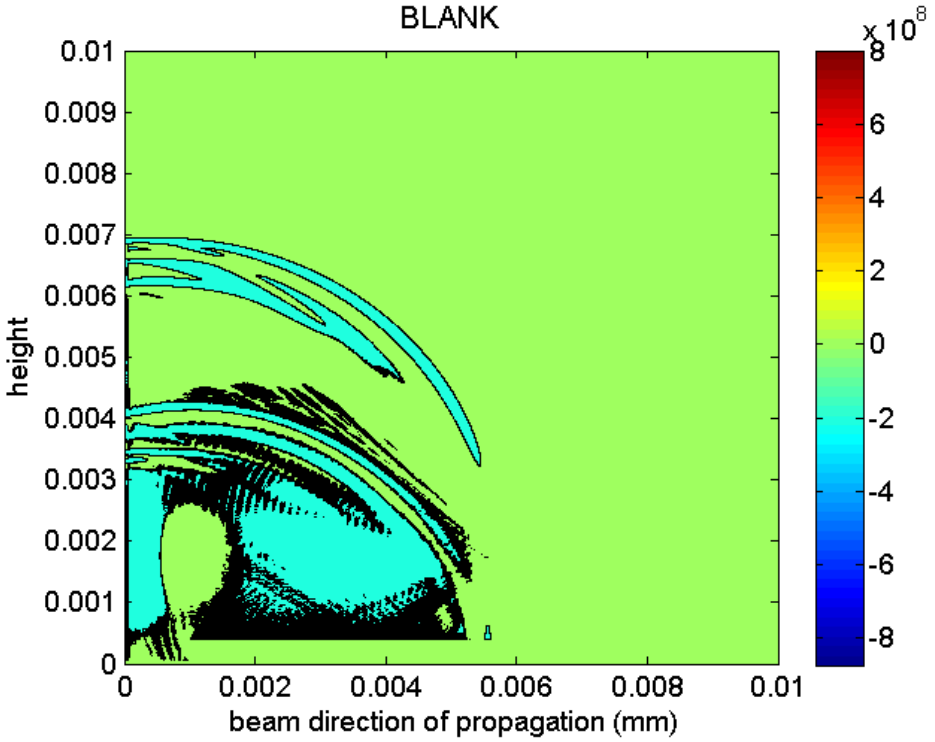

Figure 2.13: The electric field of a 3D simulation on a 500 um-period grating, for the blank

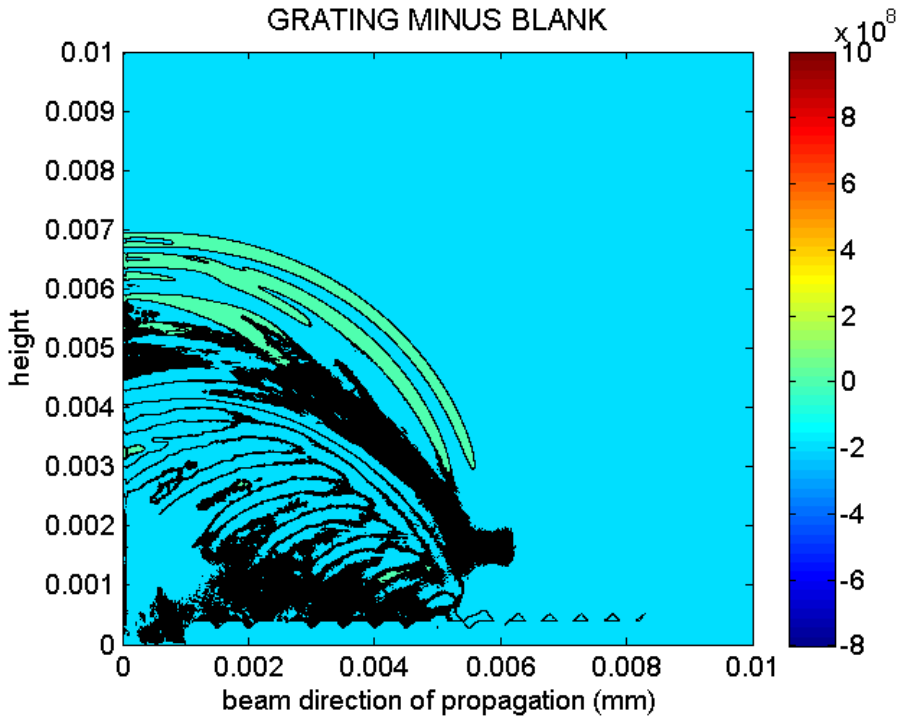

Figure 2.14: The electric field of a 3D simulation on a 500 um-period grating, for the subtracted signal.

In the figures 2.12,2.13,2.14 the contributions from the grating, the blank and the resulting subtracted signal are shown. The large black blob in the front of the subtracted plot is a numerical effect corresponding to the position of the bunch. All the three plots at the figure 2.12 - 2.14 are shown for a time at $t = 1.74\,10^{-11}$ seconds after the beginning of the simulation. Having obtained a 3-dimensional simulated region, it is possible to have an idea of the overall structure of the signal by slicing the output field over the 3D-domain. The simulation ran sufficiently long ($\approx$ 40 picoseconds) so that the bunch leaves completely the simulation box. The slicing of the domain was also performed using *HD5View*. The results are shown in the figures 2.15 and 2.16. In the 2.15, the cross-section is shown in its entirety. The bottom of the simulation is very noisy and we can't distinguish any clear feature. However, at some distance above the grating (from 7 to 10 mm) we clearly see that the radiation has a structure. A zoom in the region of interest is displayed in the figure 2.16.

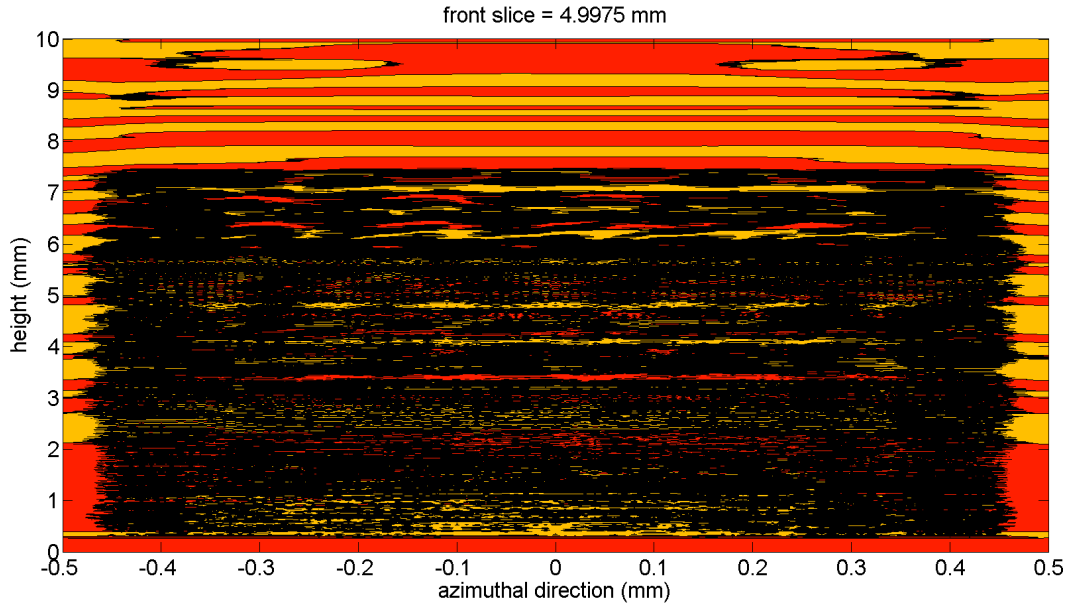

Figure 2.15: Azimuthal structure of the electric field in a 3D simulation for the 500 um-period grating. Slice over the whole simulation domain.

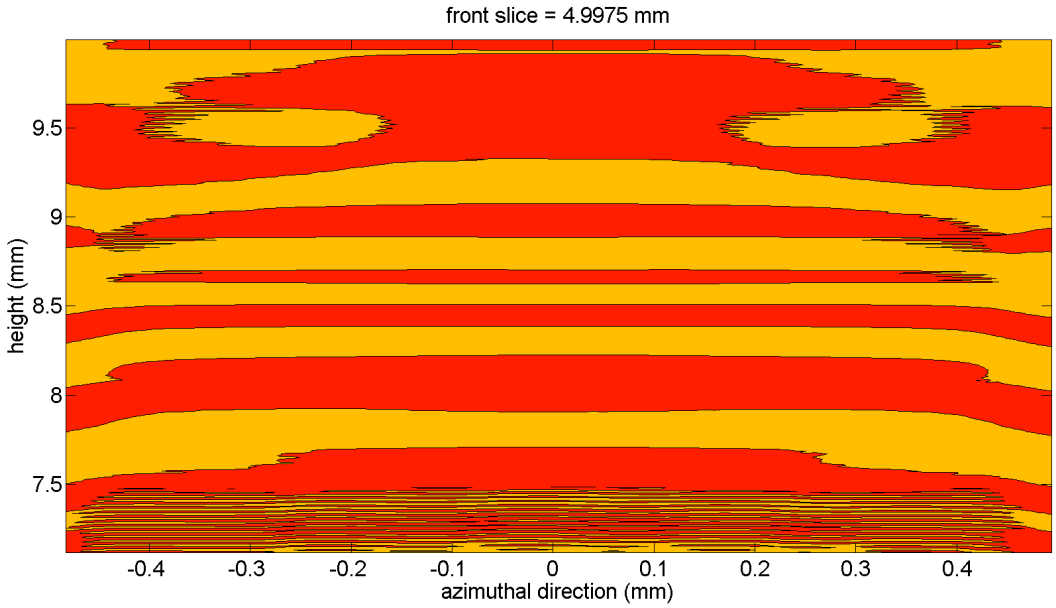

Figure 2.16: Azimuthal structure of the electric field in a 3D simulation for the 500 um-period grating. Zoom of the upper-side of the domain.

The pattern shown, strongly suggests the existence of higher orders of radiation. This is something which has never been studied specifically, as most studies focus on the fundamental mode while ignoring possible excitation of higher transverse modes. In the experimental chapter, we will show supporting evidence of the possible existence of higher modes of Smith-

Purcell radiation.

2.4 Polarization

In this last section on the degree of polarization of cSPr is considered. Interest to study polarization of Smith-Purcell radiation is motivated by the fact that no comprehensive experimental studies of the cSPr degree of polarisation is available and its understanding should help with the design of a single shot beam profile monitor. One of the contributions of this thesis was measurement of background radiation polarisation and its comparison with degree of polarisation of cSPr as well as the confirmation of the research conducted in 2012 by the team. A full and comprehensive study of polarization, which would require to build a single shot bunch profile monitor, is beyond the scope of this work. Rather, this work on polarization is meant to complement and confirm the theoretical predictions and experimental data observed previously, thus underlying possible ways to continue such studies in the future. The aim of this section is therefore to provide some simulation results to shed light on the experimental data described in the chapter 5. Basically, polarization can be described using the *degree of polarization*:

$$P = \frac{P_1 - P_2}{P_1 + P_2} \tag{2.10}$$

where P_1 and P_2 are the two polarization components. From a numerical point of view, we must define this quantity in the most general case and for various directions of radiation emission. If we consider a specific direction of observation defined with

$$\overline{n} = (\sin\theta\cos\phi, \sin\theta\sin\phi, \cos\theta) \tag{2.11}$$

we first construct the following two unit vectors

$$\begin{aligned} \overline{\varepsilon}_{\parallel} &= (\cos\theta\cos\phi, \cos\theta\sin\phi, -\sin\theta) \\ \overline{\varepsilon}_{\perp} &= (-\sin\phi, \cos\phi, 0) \end{aligned} \tag{2.12}$$

The two vectors are perpendicular to the vector $\overline{n}$, but $\overline{\varepsilon}_{\parallel}$ will be parallel to the plane $(\overline{n}, \overline{z})$, while $\overline{\varepsilon}_{\perp}$ will be perpendicular to the plane $(\overline{n}, \overline{z})$. The $\overline{G}$ quantities in the equations 2.6 used for the computation of the efficiencies, will now be separated into two distinct values $\overline{\varepsilon}_{\parallel} \cdot \overline{G}$ and $\overline{\varepsilon}_{\perp} \cdot \overline{G}$ respectively, allowing the decoupling of the previously defined grating efficiency factor R^2 into two separate contributions, that finally yield the two polarization components. This full computation is undergone in the GFW code using the numerical integration routines from NAG. The code GFW calculates the components needed, where I have used the bunch parameters displayed in the Table 2.1. The figures 2.10.1, 2.10.2 and 2.10.3 show the angular dependence of the degree of polarization for the different grating periods. We can notice a few interesting features:

- The signal is predominantly negative at small θ's (highly polarized in one of the two components), and predominantly positive at large θ's (that is, highly polarized in the other one of the two component).

- At large θ's, the components become more uniform in the values taken in azimuthal direction. This will be an important thing to remember when experimental data is analysed in the chapter 5: since the detectors average over all their aperture, it is more difficult to confront with theory if there are fluctuations across this aperture.

- In general, the amount of fluctuations across the azimuthal direction ϕ depends on the grating period. The comparison between the three figures 2.17-2.19, shows that the longer the grating period is, the more uniform is the azimuthal distribution. Another result revealed by the surface-current simulations of polarization behaviour, is that the degree of polarisation does not depend on the bunch length. In the figures 2.18, 2.20, 2.21, I show the degree of polarisation for three different bunch lengths, in the case of

1 picoseconds, 3 picoseconds and 6 picoseconds for a 1 mm beam-grating separation on a 500 microns-period grating. For the three bunch lengths, the degree of polarization has exactly the same angular structure.

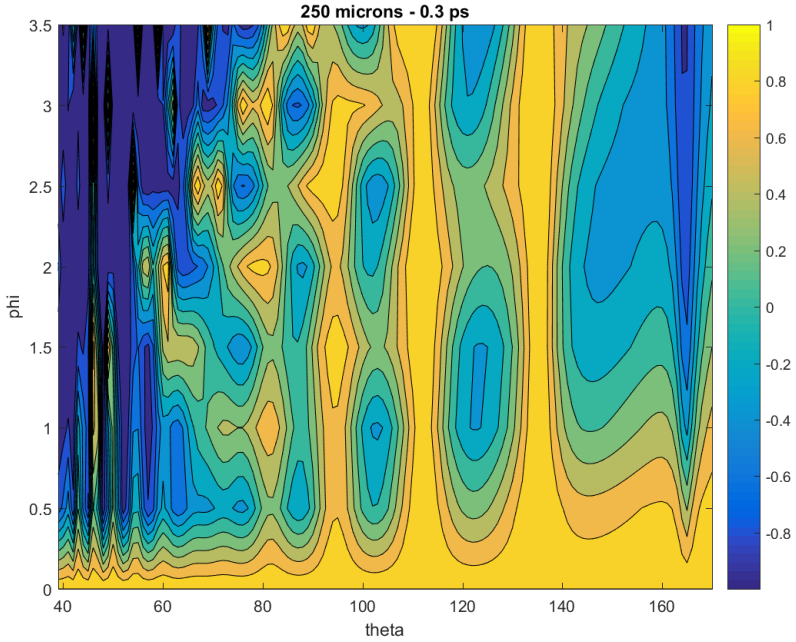

Figure 2.17: Degree of polarization of the 250 um-period grating

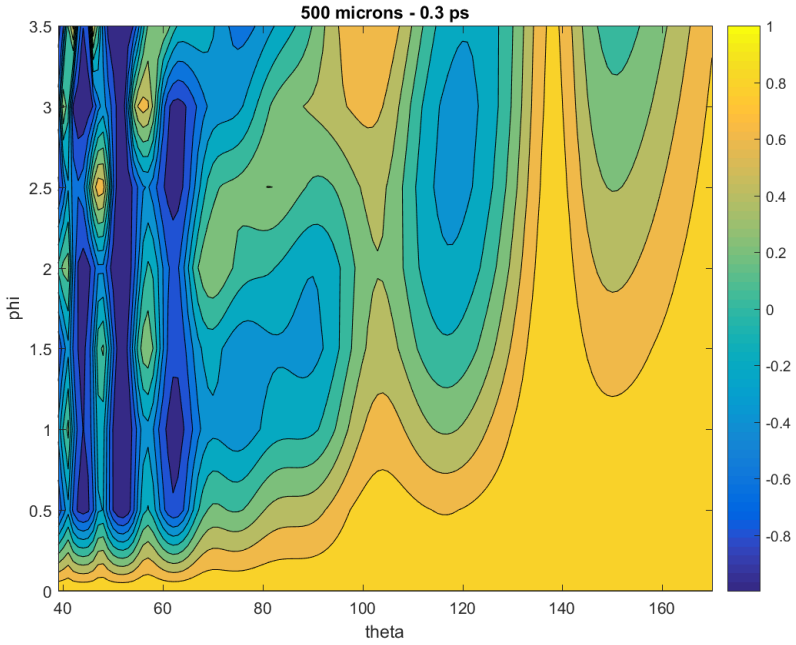

Figure 2.18: Degree of polarization of the 500 um-period grating

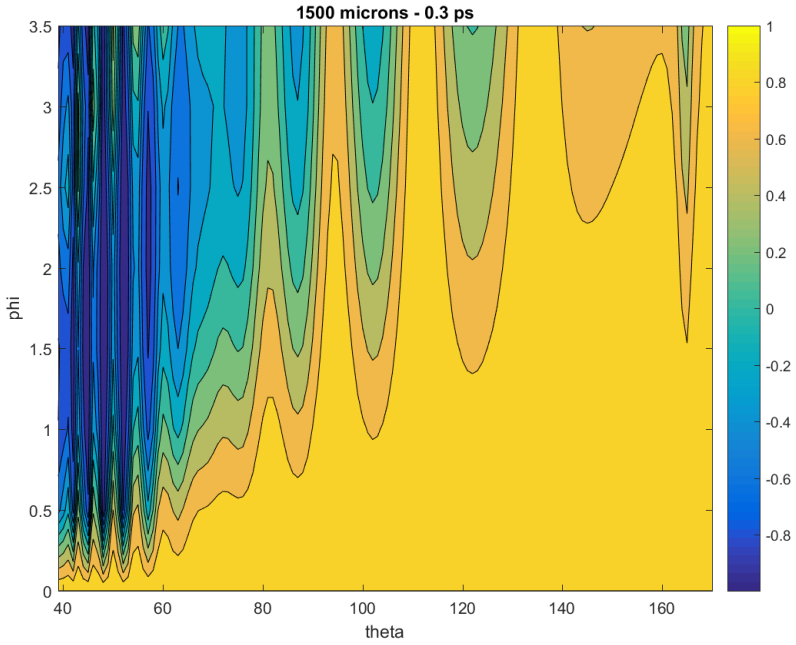

Figure 2.19: Degree of polarization of the 1500 um-period grating

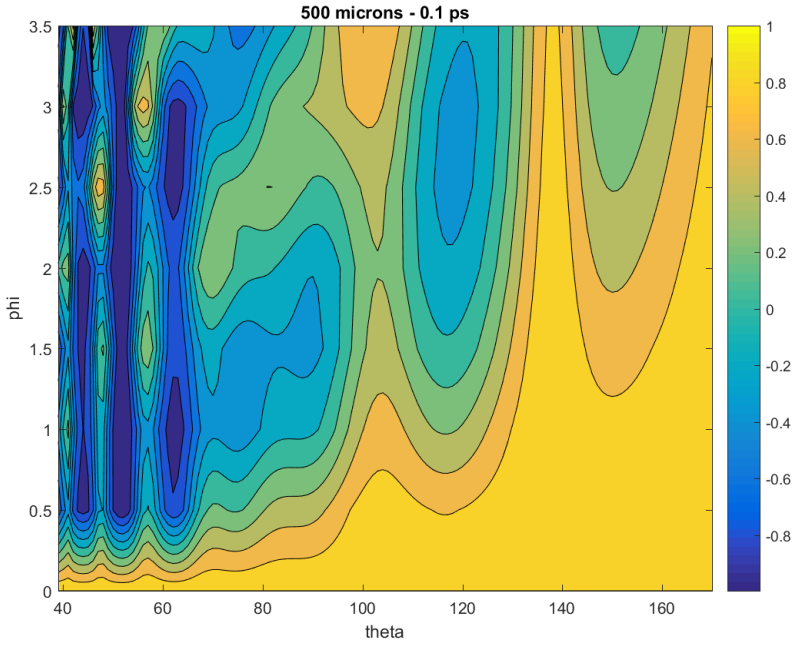

Figure 2.20: Degree of polarization of the 500 um-period grating from a 0.1 ps bunch length

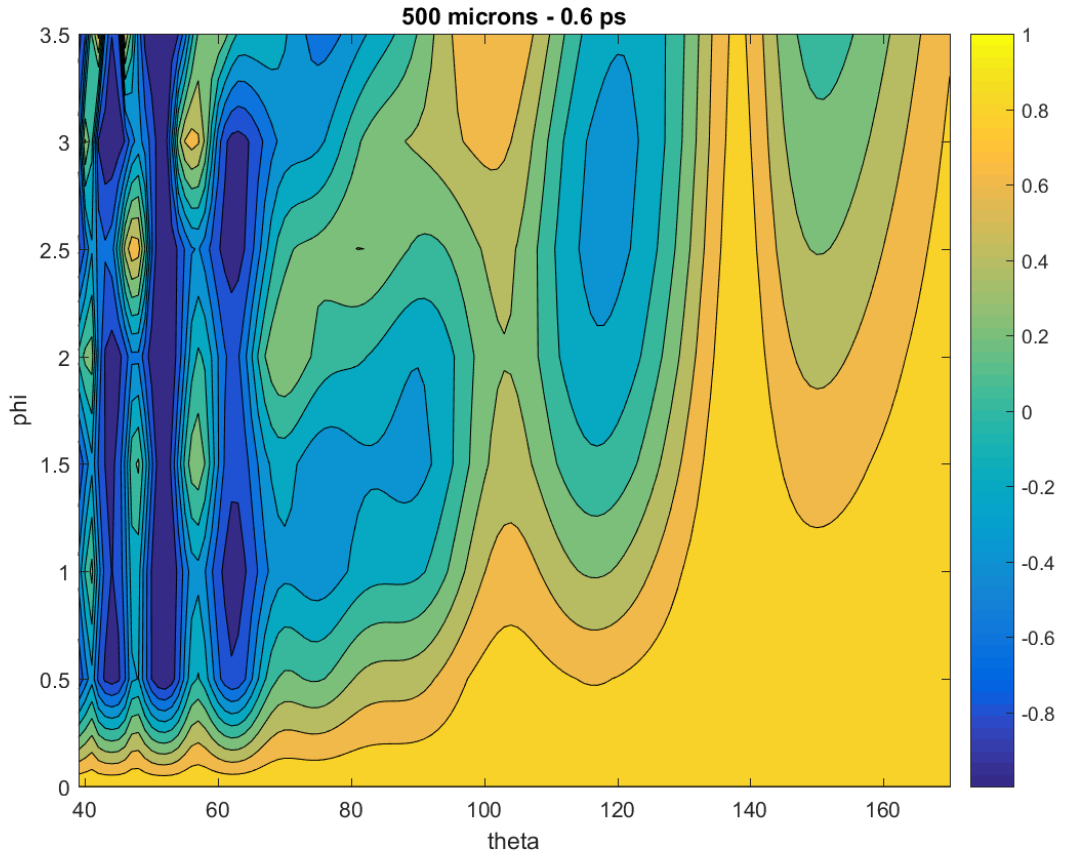

Figure 2.21: Degree of polarization of the 500 um-period grating from a 0.6 ps bunch length

We can now study the degree of polarization, using 3D PiC code *VSim*. The analysis is considerably more straightforward than in case of semi-analytical model, because the particle-in-cell simulation provides the outputs of the components of the electric field and hence, the degree of polarisation can be calculated immediately . The Figure 2.22 shows the degree of polarization in the frequency domain at $\phi = 1$ degree for a 500 microns-period grating. Because we are so close from the azimuthal middle-plane $\phi = 0$, the Smith-Purcell radiation is highly polarized in one of the components. It is interesting to compare this with the GFW simulation that was presented earlier in the figure 2.18, 2.20 and 2.21: in the latter, at $\phi = 1$ degree, we can already see that some of the frequencies corresponding to $\theta \in [40^o, 85^o]$ have a negative degree of polarization, while the angular region $\theta \in [85^o, 170^o]$ have a positive degree of polarization, while here for the particle-in-cell simulation, virtually all the frequencies carry the same component, i.e. the positive one.

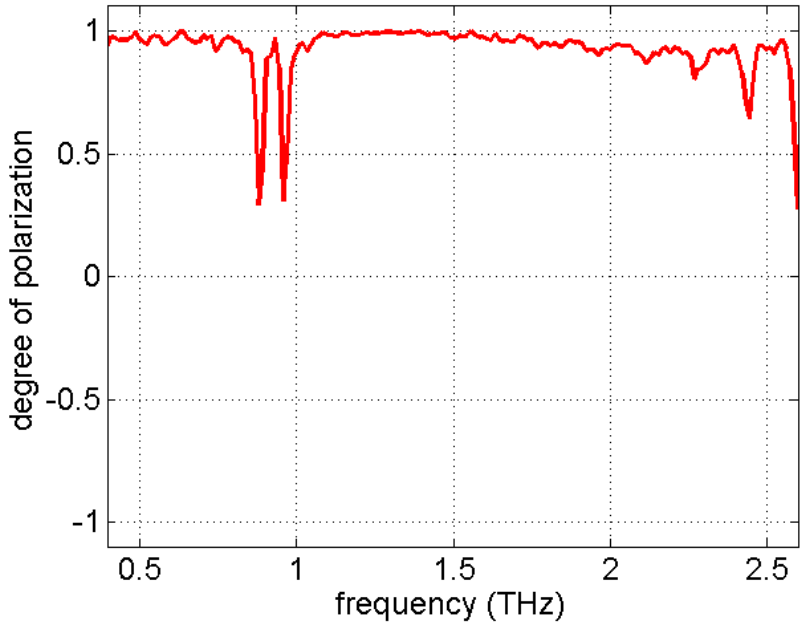

Figure 2.22: Degree of polarization of the 500 microns-period grating, at 8 mm of the grating surface and $\phi = 1$ deg

2.5 Summary of chapter 2

In this chapter, the theoretical foundations of the surface-current theory have been reviewed, and they will be the core tool of the analysis that will be carried in this work. Using the semi-analytical model based on surface-current theory the frequency-dependent behaviour has been presented for the spectrum and polarization, and compared with the data calculated using the particle-in-cell code *VSim*. The spectrum compares well between the semi-analytical and PiC models, and delimitates well-defined frequency ranges for each grating. It has also been shown that the degree of polarization clearly depends on the radiated frequency, but not on the bunch length. The azimuthal structure of the Smith-Purcell signal has also been presented and analysed, and it was shown that the far-field radiation exhibits a double-peak structure. Using PiC numerical studies it was shown that in the near-field the radiation indicates evidence of higher transverse modes.

Chapter 3

Phase reconstruction

3.1 The phase retrieval problem

In the previous chapter, we discussed some of the major properties of coherent Smith-Purcell radiation, and were able to make quantitative predictions on the spectrum we could expect. In order to do so, a certain structure for the bunch was assumed (Gaussian shape, specific length, etc.), and we deduced the relevant information on the radiated energy and spectrum. In practice however, one must deal with the opposite situation: instead of knowing the bunch structure and calculate the spectrum, experiments actually provide a spectrum first, and the task is to deduce some of the bunch properties that are not necessarily known beforehand. In our case, this requires us to determine the longitudinal profile $S(z)$ given by:

$$S(z) = \int_{-\infty}^{\infty} F(\nu) e^{2i\pi\nu z} \mathrm{d}\nu \tag{3.1}$$

In this expression, the form factor $F(\nu)$ has the complex expression:

$$F(\nu) = \rho(\nu) e^{i\Theta(\nu)} \tag{3.2}$$

where $\rho(\nu)$ is the square-root of the detected intensity, and $\Theta(\nu)$ is the phase.

Since the radiated intensity is proportional to the conjugate product $F * .F$, the phase cannot be known. It is thus important to work out a method that allows one to recover the missing phase in order to perform the Fourier Transform. This requirement, of mathematical nature, is completed with a physics motivation: the phase is well known to carry a significantly larger amount of information than the magnitude, and this can be illustrated in the example shown in the figure 3.1 inspired from an original example presented by Fienup [50], where two different pictures are Fourier-transformed into the frequency space, and then, their phase and magnitude are then separated individually. The two of them are reconstructed by recombining the phase of one with the magnitude of the other: we observe that, the information of the final picture originates dominantly from the image where the phase comes from. In performing Fourier Transform of images, one has to convert pictures into a mathematical functions. The traditional approach ("rgb" approach) is to build a coordinate matrix whose dimensions are those of the number of horizontal and vertical numbers of pixel. Each pixel in the picture has a color that can be modeled numerically by the weighting of green, blue and red. This constructs a function of the form $(f_r(x,y), f_g(x,y), f_b(x,y))$ which can be treated as mathematical map from the space of pixel coordinates (x,y), which is a subset of $\mathbb{R}^2$ to the space of numerical red-green-blue weights, which is a subset of $\mathbb{R}^3$. Programming by hand the Fourier Transform of such objects is not trivial but can be done using build-in *MATLAB* FFT functions for images, which is what I used.

Along the lines of previous published work [47] [48], this motivates the interest of investigating the physics that can be recovered through phase reconstruction methods. One of the most widely known phase retrieval technique in the accelerators beam diagnostics community is the Kramers-Kronig algorithm, which is presented in the next section. It calculates the minimum phase that is mathematically compatible with the observed spectrum, and provides accurate results when the minimum phase is the actual phase, such as in the case of single Gaussian-like functions. In real experiments however, typical longitudinal distributions do not follow a simple ideal shape, and their bunch distributions are usually not well-defined. They tend to have a fast-rising shape and a higher population of electrons in the forward-direction ("bunch head"), followed by a slow decaying population at the end

("bunch tail"). This leads to situations where the actual phase can differ from the minimum phase calculated by the Kramers-Kronig method, and this difference between the two phases is called the Blaschke phase. This limitation of Kramers-Kronig retrieval approach, justifies the investigation of algorithms that could help to retrieve better profiles, when the longitudinal bunch distribution is more sophisticated than just a simple Gaussian.

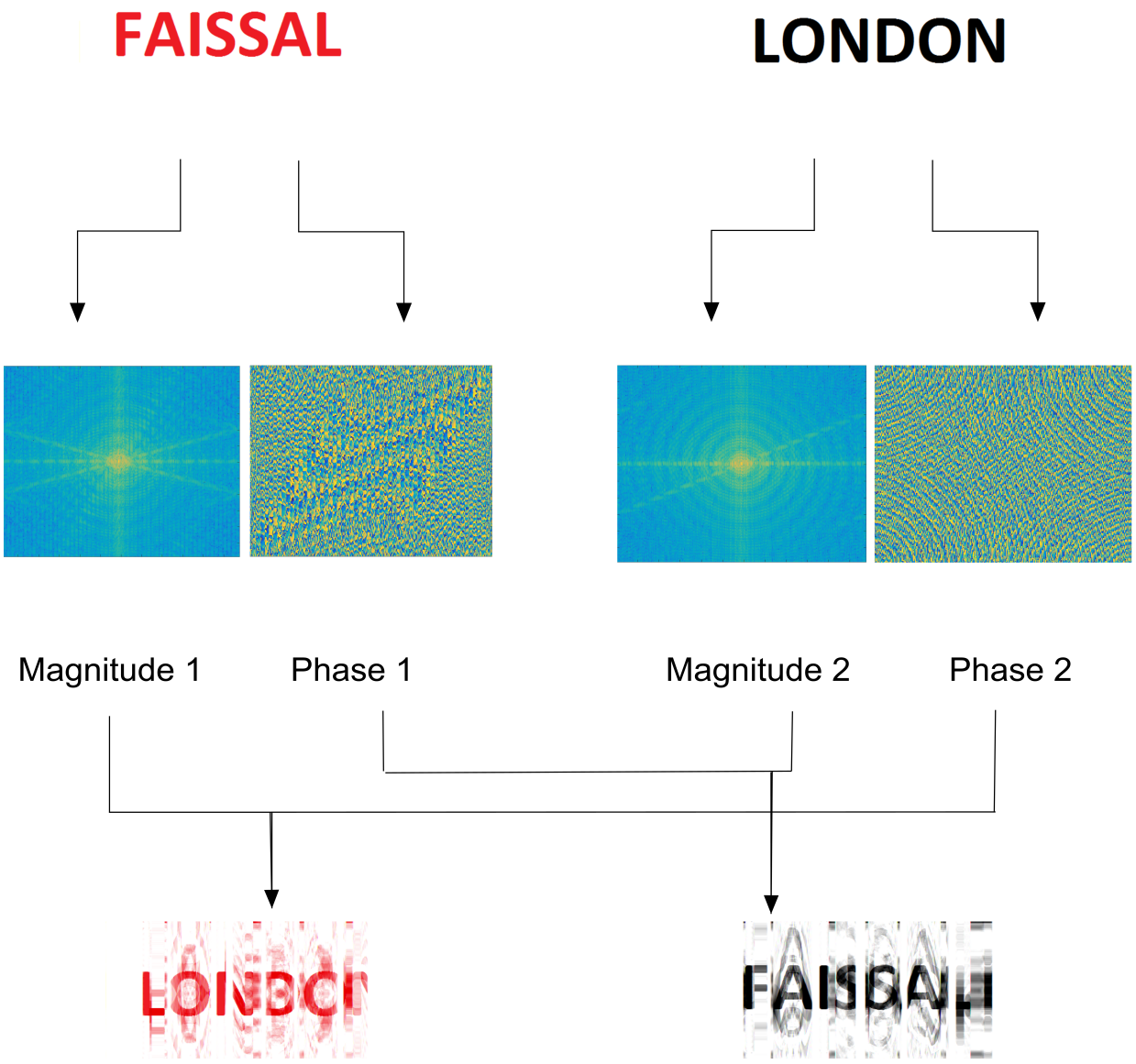

Figure 3.1: Illustration of the amount of information in the phase content of a signal

3.2 Iterative algorithms

There are various approaches to the problem of phase retrieval, but they can be categorized into three main families:

1. Projections algorithms: these are iterative algorithms that evolve through a series of Fourier Transforms alternating between the time and frequency domain. Typical examples are the Gerchberg-Saxton method, the Input-input, Output-Output, or a combination of these last two called Hybrid-Input-Output algorithm.

2. Optimization algorithms: here, instead of evolving between the time and frequency domains, the algorithm remains confined within the time domain, but with a set of constraints constructed from the spectrum information. These constraints change throughout the iterations, and a profile can be considered as solution if the constraints reach a minimum value. This family of algorithms is numerically very intensive, and the disadvantage is that the number of constraints required is very large. Typical examples of optimization algorithms are the steepest descent method and gradient-search algorithms.

3. Direct methods: direct methods are different from the projection and optimization techniques, because direct methods are non-iterative. Here, the phase is obtained through a direct one-off computation on the spectrum. The typical example is the Kramers-Kronig method. This thesis will be concerned with a new type of iterative projection algorithm that uses the information known of the Kramers-Kronig computation. This new technique will be called Phase-Constrained Iterations algorithm (PCI). It will be shown that it improves existing iterative methods and has convergence properties that are well-defined.

3.3 The Phase-Constrained Iterative algorithm (PCI)

3.3.1 Presentation and general idea

PCI is a very complex algorithm, and when describing it later in this chapter, it would be very easy to lose track of its mechanism for anyone unfamiliar with phase reconstruction literature. Therefore, before presenting it in detail, it is helpful to first outline the main concept behind it. The aim of this section is not to detail the algorithm (this will be done in the next section), but to outline the basic concepts, so that the rest of the chapter will be easier to follow. The starting point of the work in this thesis, was a recent paper [8] suggesting that the combination of two different well-known iterative projection algorithms (Gerchberg-Saxton and Hybrid-Input-Output, described in section 3.3.2) was potentially more promising than using each of them individually. Despite this improvement, there were still three challenging issues:

1. Sophisticated profiles such as combination of Gaussians still couldn't be reconstructed in a completely satisfactory way by a combination of Gerchberg-Saxton with Hybrid-Input-Output, even if the reconstruction was already better than using just one of these algorithms alone.

2. The reconstructed profile was not unique: running the "combined" algorithms twice, with exactly the same set of parameters, would not necessarily bring the same output profile. The problem comes from the fact that these algorithms are seeded with an initial random estimate, which consequently yields an unpredictable output. The traditional solution was to average over a large number of runs, or go through a visual post-selection of a most plausible profile purely based on visual inspection. This approach has obvious problems of consistency.

3. Any error estimation was limited to the usual root-mean-squared computations for theoretical cases where the original function is known, and there was no possibility to quantify any type of error in experimental situations. The idea in our work, is to

improve the efficiency of the combination of algorithms suggested in [8], by imposing the Kramers-Kronig minimum phase as initial and boundary condition. It will be shown that it constrains so strongly the iterative process, that it makes the output solution always unique, and removes completely the need for post-processing. Furthermore, in the specific context of bunch length diagnostics, we will see that it is possible to devise an error analysis method that helps to keep track of the convergence.

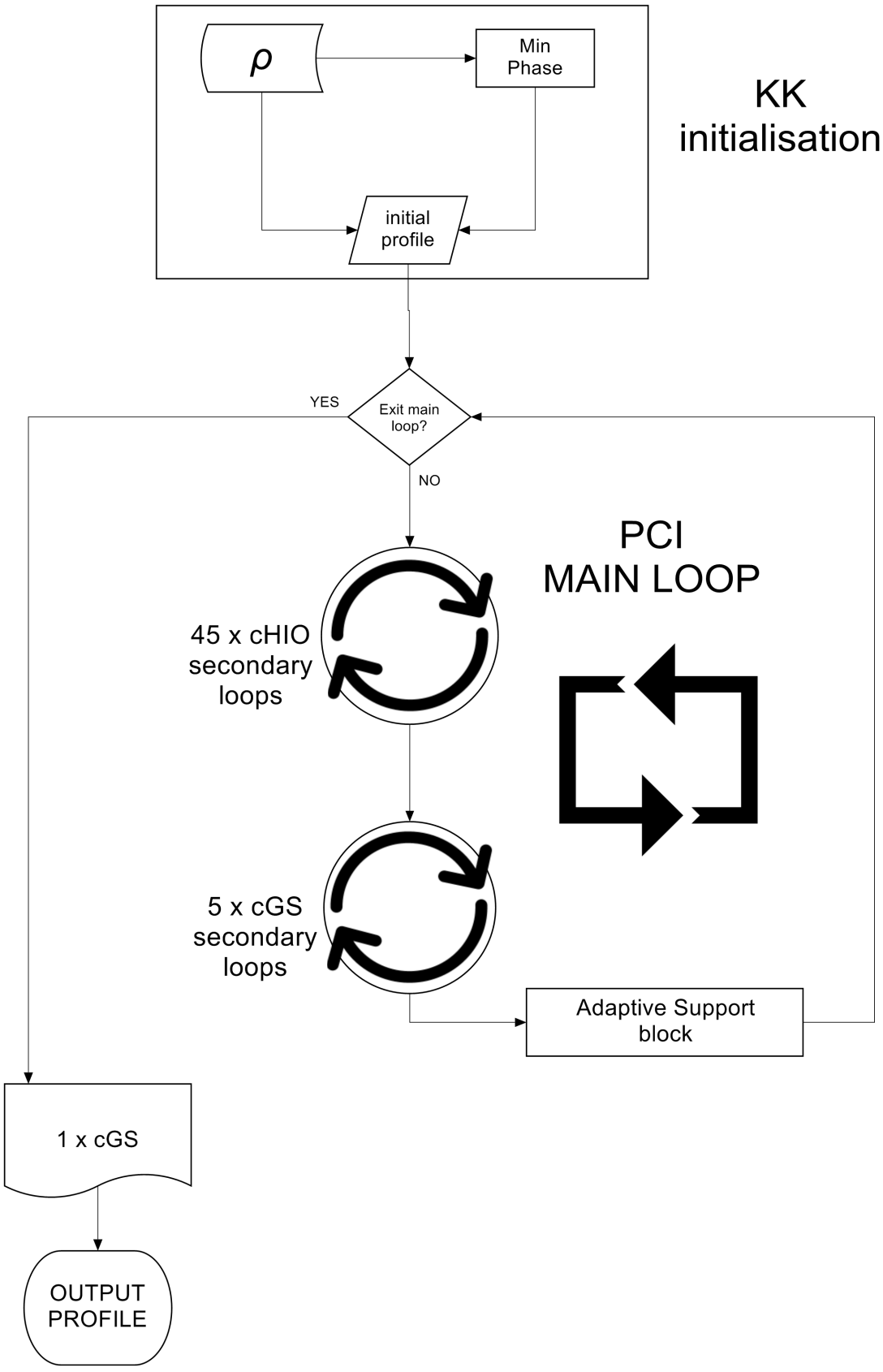

Figure 3.2: Structure of the PCI Algorithm

The core architecture of the PCI algorithm is presented in the figure 3.2. It is worth to have a general overview of the whole mechanism first, instead of going directly into the details of each step, which would be too confusing. The figure 3.2 shows that PCI is organized as follows:

- It starts with a KK initialization block that computes a Kramers-Kronig profile.
- It continues into what is called in the figure the "Main PCI Loop", which itself contains two sets of subloops called cHIO and cGS, standing respectively for constrained Hybrid-Input-Output and constrained Gerchberg-Saxton algorithms. The constrained name means here that HIO or GS, which will both be described later, are being constrained by the implementation of KK boundary conditions. It should be noted that cHIO and cGS share a lot of similarities. They behave exactly the same way in the frequency domain. It is their time domain mechanism that differs, as shown in the next section, when the substructures of cHIO and cGS will be explained, in the figures 3.3 and 3.4 respectively.
- The main PCI loop contains also a block labelled Adaptive Support block, which is a Gaussian filter that will be described too.
- In the figure 3.2, we see that the numbers of subloops cHIO and cGS is precisely defined (there are 45 cHIO subloops and 5 cGS subloops) but no information is mentioned about the number of iterations in the main loop. This is because the number of iterations of the main PCI loop depends on the spectrum we are analysing. It will be shown later that the calculation of a new type of error will help to identify how many iterations are needed. This will then provide an exit condition from the main PCI loop.
- At the exit of the main loop, a final cGS is implemented to stabilize the algorithm, before to obtain the output profile of PCI.

With this general overview in mind, we are now ready to analyse the structure of the PCI blocks in detail.

3.3.2 Structure of the Phase-Constrained Iterations algorithm

The KK initialization block requires the experimental intensity $|\rho|^2$, from which we obtain ρ and calculate the Kramers-Kronig minimum phase using

$$\Theta(\omega_0) = \frac{2\omega_0}{\pi} \int_0^\infty \frac{\ln \frac{\rho(\omega)}{\rho(\omega_0)}}{\omega_0^2 - \omega^2} \mathrm{d}\omega \tag{3.3}$$

where $\omega = 2\pi\nu$. This formula for KK-phase computation is valid if the function does not have any zero. Once the Kramers-Kronig phase has been calculated, one can retrieve an initial profile, and it can be shown [2] that in the ultrarelativistic case, assuming that z=c.t, the expression for the longitudinal distribution is then given by:

$$S(t) = 2 \int_0^\infty \rho(\nu) \cos(2\pi\nu t + \Theta) \mathrm{d}\nu \tag{3.4}$$

This function will be the initial profile for the main PCI loop. When entering the PCI main Loop, the initial KK-profile first stops at the cHIO subloop and will undergo 45 iterations. The constrained Hybrid-Input-Output Algorithm is described in the figure refFig303, and consists in the following steps:

1. It first receives a profile in the time domain: this can be either a profile from the KK initialisation, or a profile from the main PCI loop (see the general map of PCI in figure 3.2), or, if we are operating within the subloop of 45 cHIO iterations, it receives the previous cHIO output. The figure 3.3 illustrates the case where cHIO starts with the output of a previous cHIO iteration of the subloop.

2. That time profile is transformed onto the frequency domain with a FFT

3. We apply the so-called KK boundary conditions to the phase obtained from that FFT, and compare them with the KK minimum phase: for every positive frequency, if a phase obtained through the FFT is below the minimum phase, then it is adjusted to that minimum phase. If the FFT phase is above the KK phase, it remains unchanged, that is :

$$\begin{cases} \Theta_n(\nu) > \Theta_{KK}(\nu) \Rightarrow \Theta_{n+1}(\nu) = \Theta_n(\nu) \\ \Theta_n(\nu) < \Theta_{KK}(\nu) \Rightarrow \Theta_{n+1}(\nu) = \Theta_{KK}(\nu) \end{cases} \tag{3.5}$$

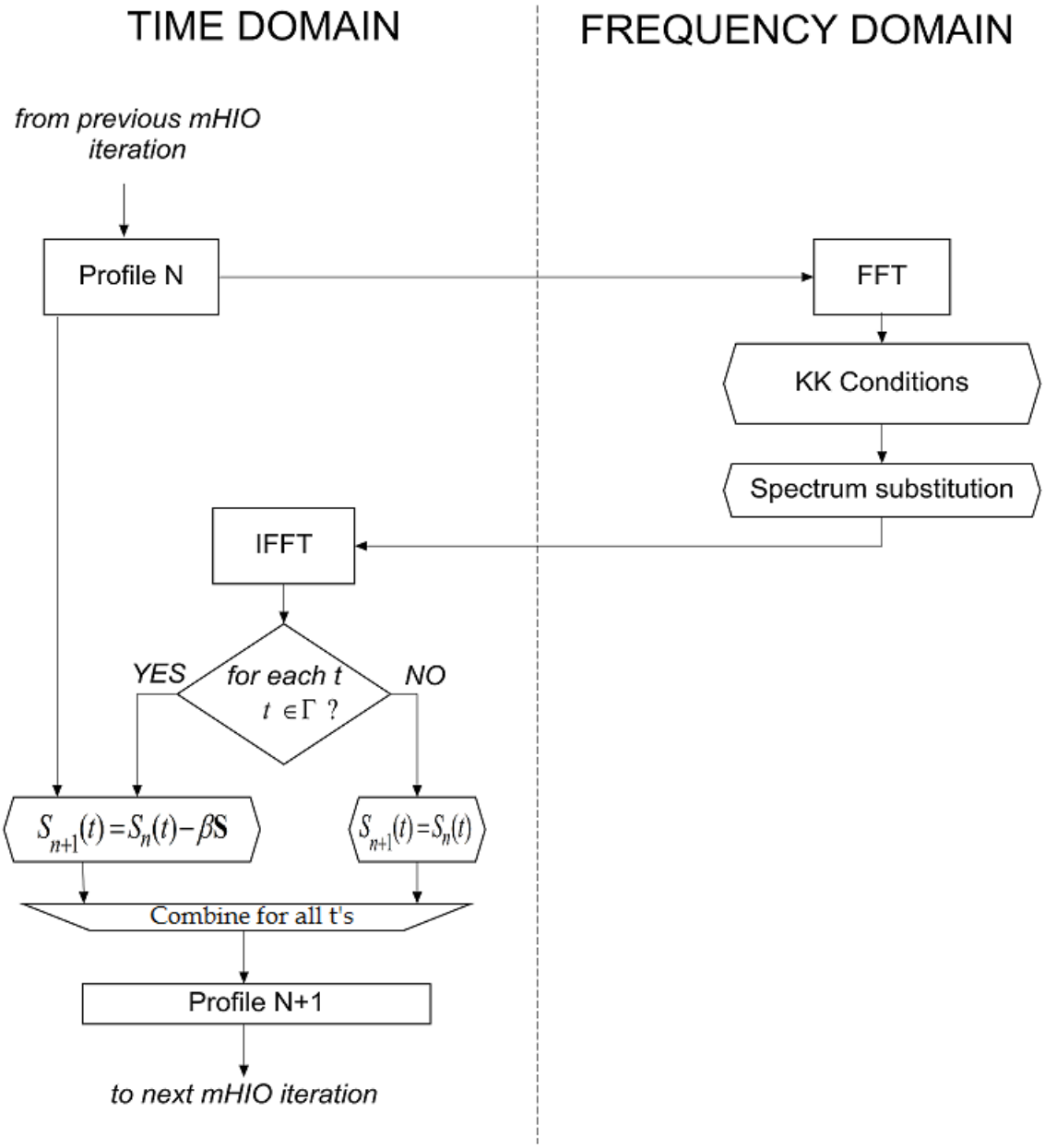

Figure 3.3: Detail of a cHIO secondary loop

4. The spectrum of the calculated FFT is replaced by the experimental spectrum

5. A new time profile is calculated by an IFFT using the experimental spectrum and the phases Θ . We call this time profile $\mathbf{S}$.

6. We must now apply the time-domain constraint, detailed in the figure 3.3 too. Following the terminology widely accepted in phase retrieval literature, we define Γ as the set of all non-physical points in the time-domain, that is, the t points where the time profile $S_n(t)$ is negative. The time-domain constraints are then chosen as

$$\begin{cases} t \notin \Gamma \Rightarrow S_{n+1}(t) = S_n(t) \\ t \in \Gamma \Rightarrow S_{n+1}(t) = S_n(t) - \beta \mathbf{S} \end{cases} \tag{3.6}$$

   is the output of the loop, namely the profile at the end of this cHIO iteration. Here is a parameter commonly called feedback parameter, which we shall comment about. This is changed at each iteration of the main PCI loop, in the "Adaptive Support" block, but remains constant within all the iterations of a cHIO subloop.

The next stage of PCI is the cGS subloop, executed for 5 iterations only. This subloop consists in the following steps:

1. The start of a cGS iteration is a time profile which is either received from the output of cHIO (see figure 3.2) or from a previous iteration of the same cGS subloop

2. The FFT of that time profile is performed, and the frequency part of the cGS is exactly the same than in cHIO: the KK boundary conditions are implemented, the spectrum of the FFT is replaced by the experimental spectrum, and an inverse FFT is calculated to obtain back a time profile.

3. When the cGS process arrives back in the time domain, positivity is imposed over the whole time domain. This is done by forcing all the negative points of the time profile to zero. With the same notations than in cHIO, this means:

$$\begin{cases} t \notin \Gamma \Rightarrow S_{n+1}(t) = S_n(t) \\ t \in \Gamma \Rightarrow S_{n+1}(t) = 0 \end{cases} \tag{3.7}$$

Finally, we see in the figure 3.2 that the *Adaptive Support block* comes after the execution of cGS subloops. The Support is defined as the interval t in the time domain where the reconstructed function has non-zero values. The idea of an Adaptive Support process was first described by Marchesini, who noted in [37] that the convergence of iterative algorithms could be improved by the introduction of small perturbations on a few fundamental parameters. The idea was initially applied to two-dimensional problems, and more recently, applied to one-dimensional problems too [8]. The one-dimensional implementation of an Adaptive Support mechanism consists in the three steps. First, the output of cGS is convolved with a Gaussian that acts as a blurring function. Secondly, the value of the feedback parameter is shrunk by multiplying it by 0.98. As a result, when the Main PCI loop arrives back at the block of cHIO subloops, it will run with a different value of β . As a third and final step, the standard deviation of the Gaussian used for the convolution, is multiplied by 0.99 and undergoes a small shrinking.

The shrinking of β and the Gaussian used for convolution, is the reason why Marchesini initially referred to this method as "shrink-wrap" in his 2-dimensional study [37]: shrink the parameters, and wrap up to the next iteration.

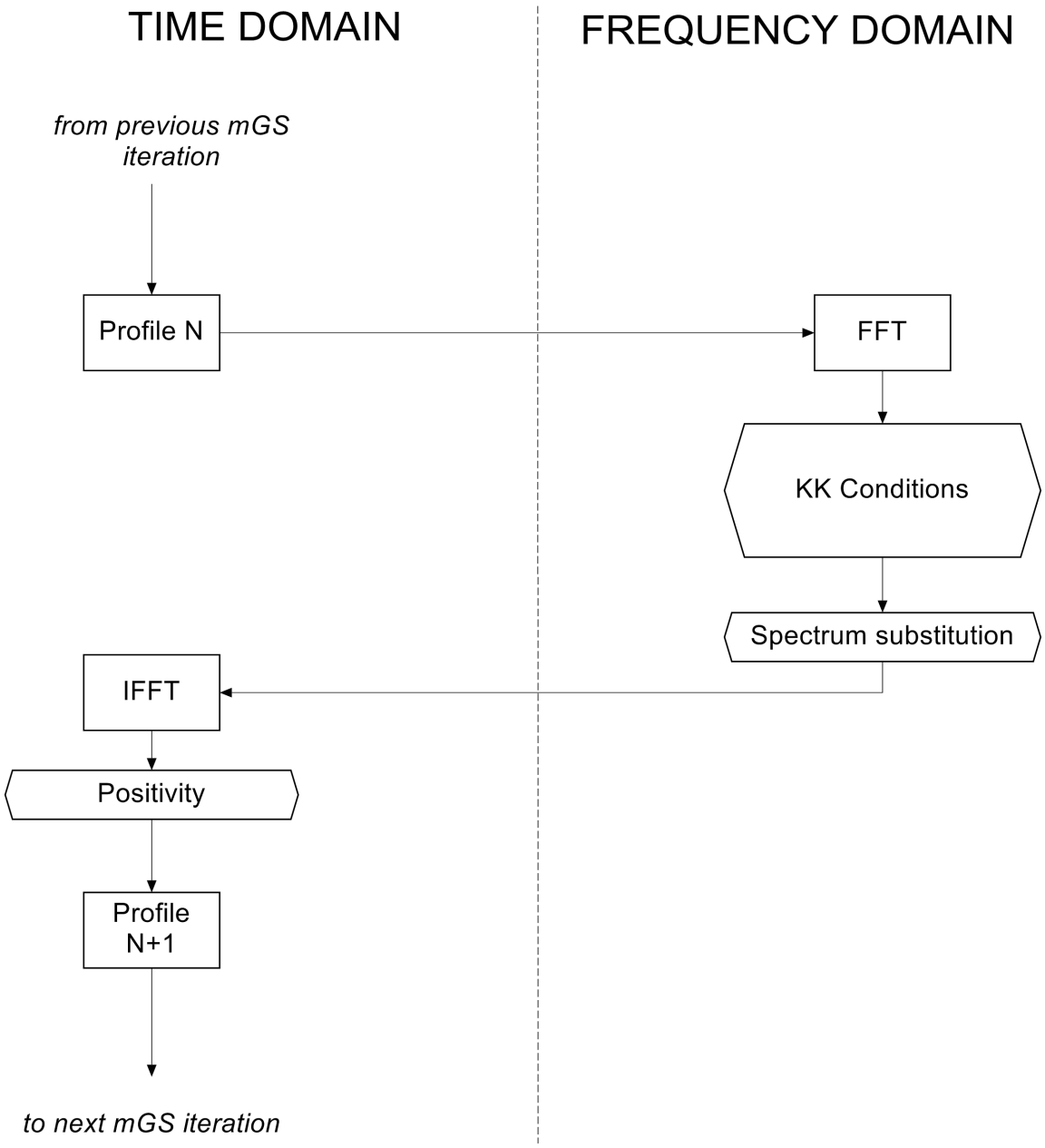

Figure 3.4: Detail of a cGS secondary loop

It is worth to briefly compare cGS and cHIO to appreciate the importance of the feedback parameter. Historically, the GS algorithm (that is, cGS without its KK initial and boundary conditions) was developed in Cambridge in 1972. It was tested on synthetic functions, and errors were estimated by calculating the rms. It was then noticed that the convergence could be subject to stagnation: the rms stabilized at a specific value. It is the investigation of this problem that motivated the introduction of the parameter . Various algorithms were introduced, all of them trying to avoid stagnation using an extra-parameter , with only

limited success. The original version of the HIO algorithm, designed by Fienup in 1982 [47] [48] is the first that improved the issue in simple cases, even though the specific problem of convergence for complicated functions remained unsolved.

The last part of the PCI Main Loop is an exit condition to decide whether the Main Loop is completed, or whether another "cHIO-cGS-Adaptive Support" sequence must be executed. That exit condition consists in checking that a sufficient number of iterations N has been carried out. The number N is not known in advance and depends on the profile to be reconstructed. To determine it, it is natural to require the PCI algorithm to run long enough to converge to a solution, that is, to ensure that some sort of error is within a specified tolerance. This leads us to one of the central features of PCI: how do we define an error? Since the actual function is not known in experimental cases, one cannot use the traditional root-mean-squared approach. The idea is to compensate this lack of information, by using another extra-information: in the experiments I underwent, even though the final bunch profile is usually not known, the total charge present in the bunch is a known quantity. Because a typical profile is actually a plot of the current density against time, the integral of the final reconstructed profile is the experimental charge. In practice, the integral can be normalized to unity. Knowing this, it is possible to devise the following two convergence criteria. If is the known integral of the longitudinal distribution, and that we note the reconstructed profiles at iterations n and n+1 respectively, we define two errors δ_1 and δ_2 with:

$$\begin{cases} \delta_{1,n+1} = \frac{\int_0^\infty |f_{n+1}(t) - f_n(t)| \mathrm{d}t}{F} \\ \delta_{2,n+1} = \frac{|\int_0^\infty f_{n+1}(t) \mathrm{d}t - F|}{F} \end{cases} \tag{3.8}$$

Here, $\delta_{1,n+1}$ and $\delta_{2,n+1}$ are the calculated errors δ_1 and δ_2 at iteration $n+1$. The first formula is mathematically consistent and has the structure of a Cauchy sequence: it ensures that the profile converges if this error integral goes to zero. The second integral is a required condition too, to distinguish between actual correct convergence, from potential pathological situations where the longitudinal profile would converge (and then the first integral error

would be satisfied), but would converge toward a wrong solution. With these two errors now defined, we can decide that the exit condition for the Main Loop of PCI will be satisfied for a number of iterations N such that these two errors become smaller than some pre-defined tolerances ε_1 and ε_1 :

$$\begin{cases} \delta_{1,n+1} = \frac{\int_0^\infty |f_{n+1}(t) - f_n(t)| \mathrm{d}t}{F} & < \varepsilon_1 \\ \delta_{2,n+1} = \frac{|\int_0^\infty f_{n+1}(t) \mathrm{d}t - F|}{F} & < \varepsilon_2 \end{cases} \tag{3.9}$$

When the exit condition of the Main Loop is satisfied after these N iterations, a final cGS is applied just once, and the final profile is then obtained.

In the next section, I shall describe in detail the processing of a synthetic function through PCI. The application of PCI on the time profile reconstruction from experimental data will be studied in the chapter 5.

3.4 Detailed treatment of an example

3.4.1 General comments on the profile reconstruction of a double Gaussian

The example studied here is a double Gaussian g(t) of the form

$$g(t) = A_1 \exp(-\frac{(t-\mu_1)^2}{2\sigma_1^2}) + A_2 \exp(-\frac{(t-\mu_2)^2}{2\sigma_2^2}) \tag{3.10}$$

Where the parameters A, μ and σ are the amplitude, mean and standard deviation respectively, and take the following values:

$$A_1 = 1$$

$$A_2 = 0.2$$

$$\sigma_1 = 0.0085$$

$$\sigma_2 = 0.4247$$

$$\mu_1 = 0.0425$$

$$\mu_2 = 0.5425$$

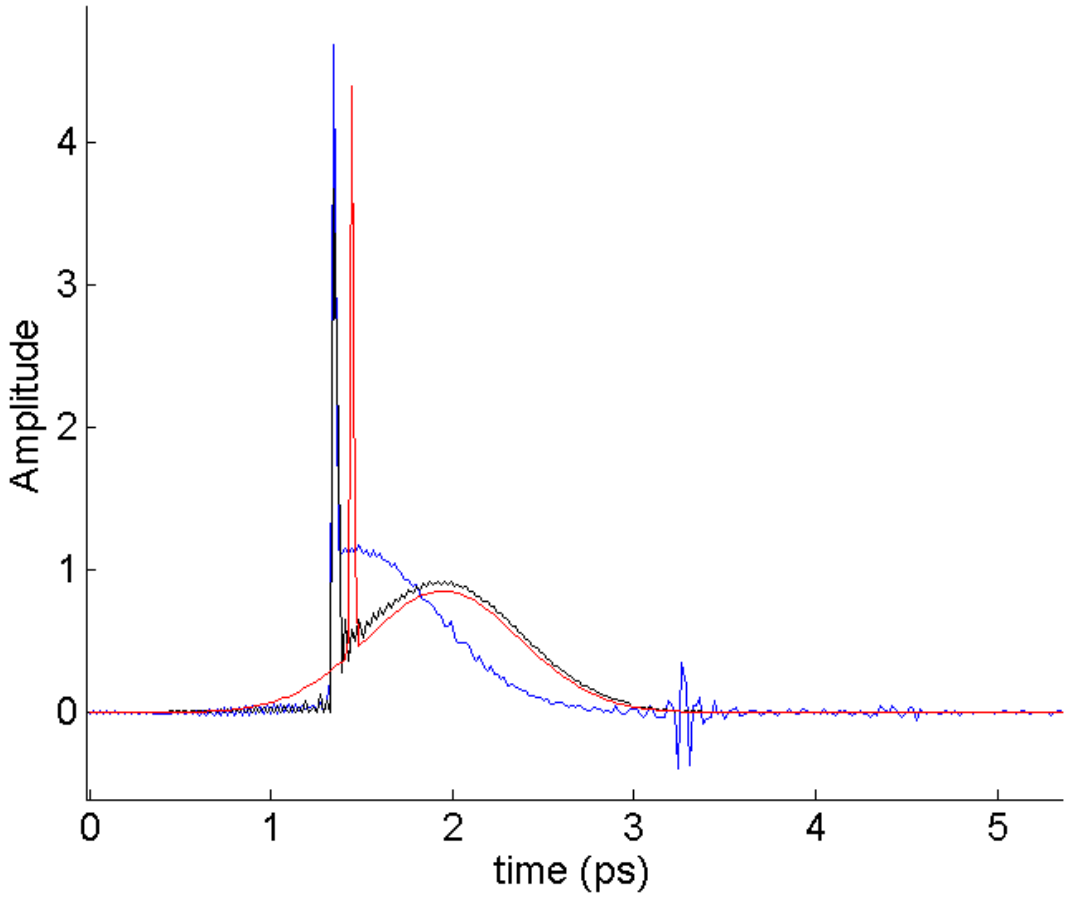

Figure 3.5: Comparison of the outputs. Red: the original profile - Blue: The KK reconstruction - Black: The PCI reconstruction

The function shown above has two features which make it difficult to reconstruct namely: large variation of amplitudes and widths of the two Gaussians. The figure 3.5 compares the output from Kramers-Kroning and PCI with the original profile. There we see that the sharp-peaked Gaussian disrupts the KK-reconstructed profile by

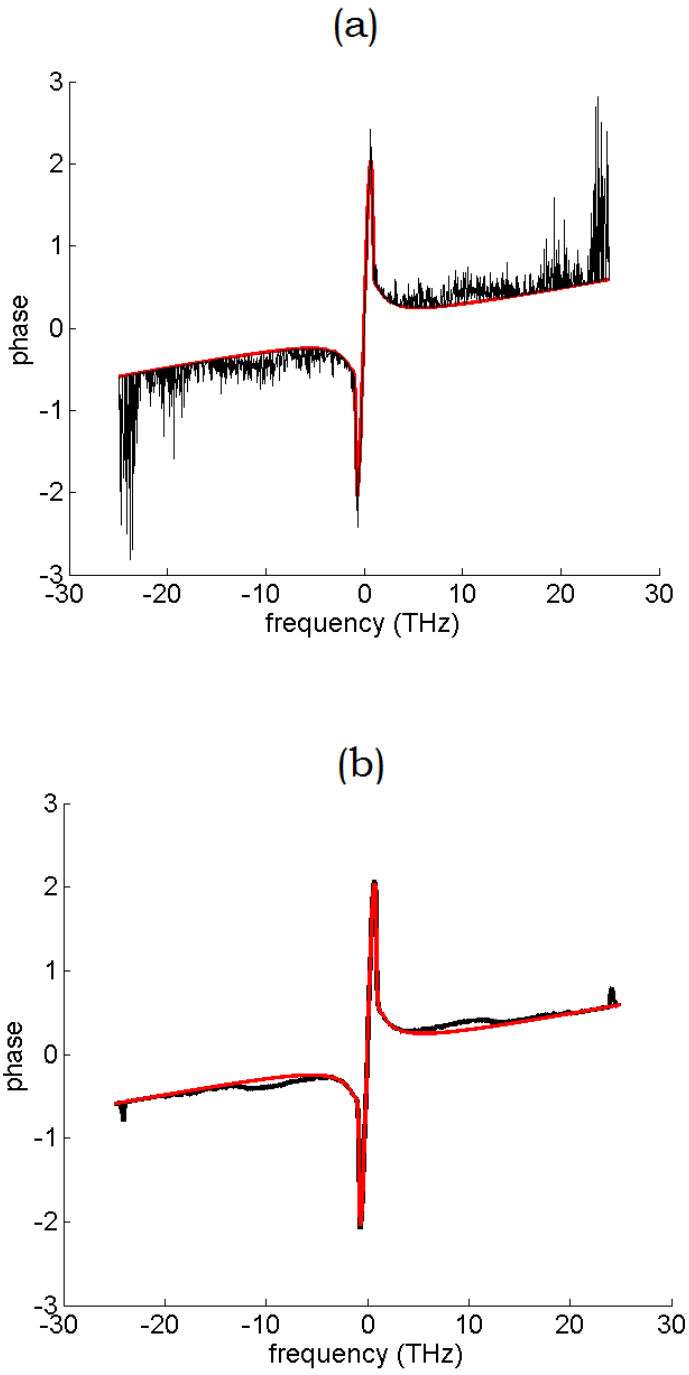

Figure 3.6: Dynamics of the phase retrieval. The KK phase is in red, and the PCI phase is in black. (a) Phase plot during the execution of PCI – (b) Final phase output

imposing a steep rise in the reconstruction, making it essentially discontinuous, and a failure to retrieve the main Gaussian of the original function. We also see that the KK profile is flawed with numerical oscillations originating from the sampling of the spectrum: a higher sampling rate decreases the number of these unphysical oscillations, but at the cost of a longer computational time. In the figure 3.5, we see that the PCI profile manages to reconstruct the combination very well compared to KK: unlike KK, it succeeds very well in rebuilding the main Gaussian. We can see that a small sharp-rise is still present, but the discontinuity induced in the overall curve is much less damaging than in the KK case.

3.4.2 Dynamics of the phase retrieval

After having observed how PCI reconstructed the profile, it is interesting to have a closer look at the reconstruction process of the phase itself. The inset a of the figure 3.6 shows the phase during the execution of the algorithm, and the inset b shows the output phase after completion. We observe that, while the PCI phases seems to have a random behaviour during its run, they seem to stabilize at the end toward a phase plot which is not so different than the KK, while still having distinct features from the KK phase. The final phase plot can therefore be seen as a perturbation of the KK phase. The phase pattern shows clearly a stabilisation in the sense that the random behaviour is considerably less pronounced in the figure in the inset b of the figure 3.6 than in th inset a.

3.4.3 Convergence pattern and role of the KK conditions – The problem of uniqueness

The convergence of profile retrieval through the progress of PCI iterations, can be studied using the errors defined in the section 3.3.2. In the figure 3.7, we can see that for this particular function, the integral error follows a pattern where the reconstructed profile oscillates between situations where the two errors are very small, down to 2%, and situations where the error can be larger. The figure 3.7 further reveals that a minimized error is obtained at

specific iterations: we have a minimum near 50, at 92, at 130, near 180, etc. The figure 3.8 shows that the final PCI profile reconstructed at these different minima of the integral error, are essentially the same. A final feature that can be noticed in the figure 3.7 is the existence of a plateau in the first few iterations (from 1 to 6 iterations), where the integral errors are low. I shall show later that this initial plateau is due to the behaviour of β .

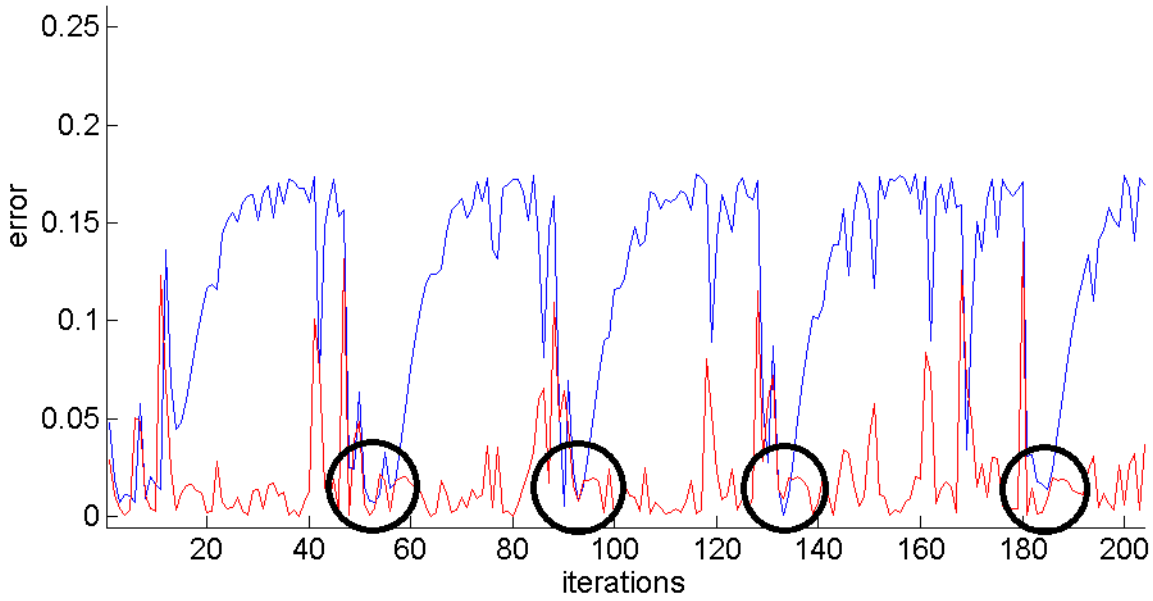

Figure 3.7: Evolution of the two errors with PCI iterations. Blue: the error δ_1 - Red: the error δ_2 The optimal profiles are reconstructed for simultaneous minimization of δ_1 and δ_2

It is possible to understand the role and importance of the KK-constraint by examining what is the dynamics of PCI when the KK-conditions are relaxed. This means two things:

1. Instead of being initialised with KK phases, PCI starts with the generation of a random number for each frequency (initial seed).

2. In the frequency domain, the KK boundary conditions are not implemented: if a phase reaches a lower value than the KK-phase, it is then accepted.

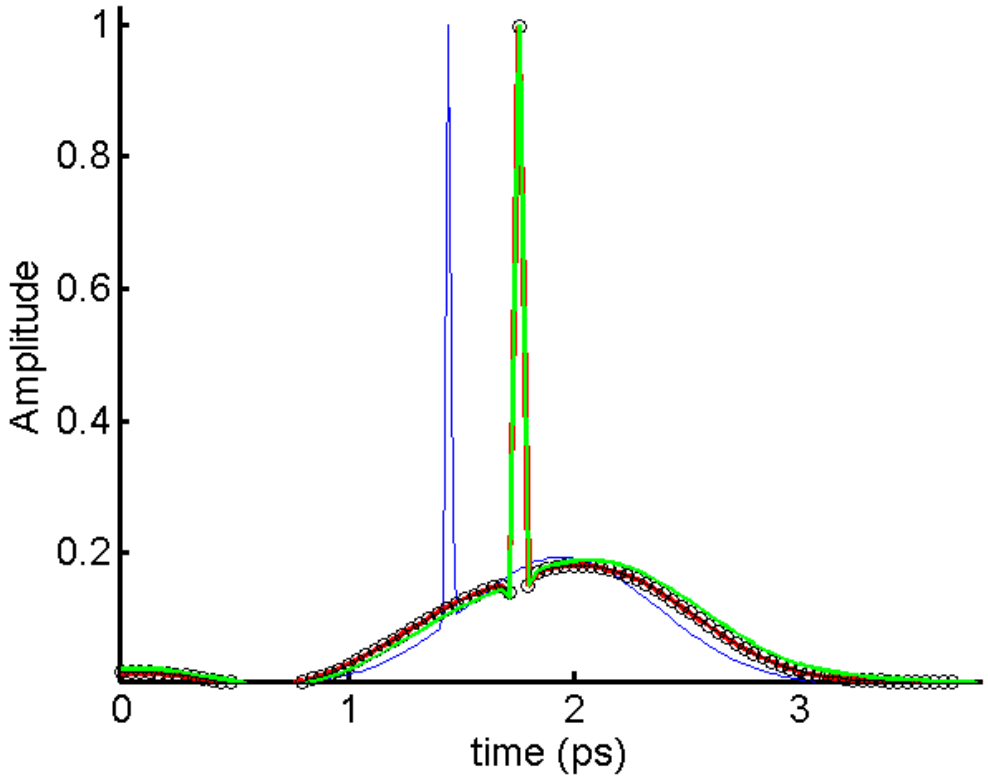

Figure 3.8: Reconstruction at the points of simultaneous minimization of δ_1 and δ_2 Blue: original profile - Red: 92 iterations - Black: 130 iterations - Green : 185 iterations

The figure 3.9 shows the outcome of the processing of the KK-relaxed version of PCI, where the initial condition combines the known spectrum with the generated random seed. The reconstruction of this profile made use of the post-processing method described in [8]. It clearly fails to recover the original profile.

Another non-trival consequence of relaxing the KK-conditions is that the error does not follow a regular path like in the phase-constrained version of PCI. In the figure 3.10, we see the behaviour of the integral error as displayed through three distinct runs of the algorithm: the result of the PCI pattern is unchanged, while every time we feed it a random seed and do not implement KK-conditions, the error function changes. In two of the three KK-relaxed runs, we see that the convergence is attained at different iterations (130 and 172) while a third run has still not converged after the

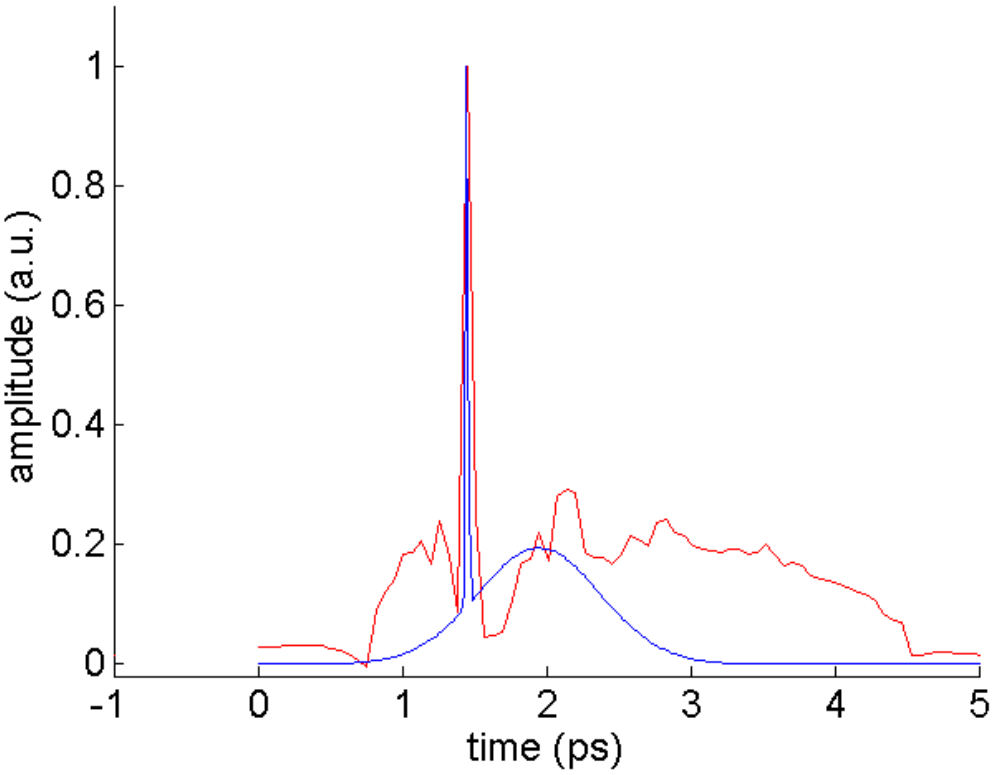

Figure 3.9: Blue: original profile. Red: output of PCI relaxed from its KK-conditions (this plot is a joined work from James Cowley and I)

run ceased. This sheds a light on two well-documented aspects of iterative algorithms based on a random seed, are - they produce several profiles as output depending on the initial phase randomly generated. - The requirement of a post-processing is usually needed to help determine a possible candidate among all the outputs, for example by performing an averaging of a large number of solutions, or select a plausible subset of solutions [22].

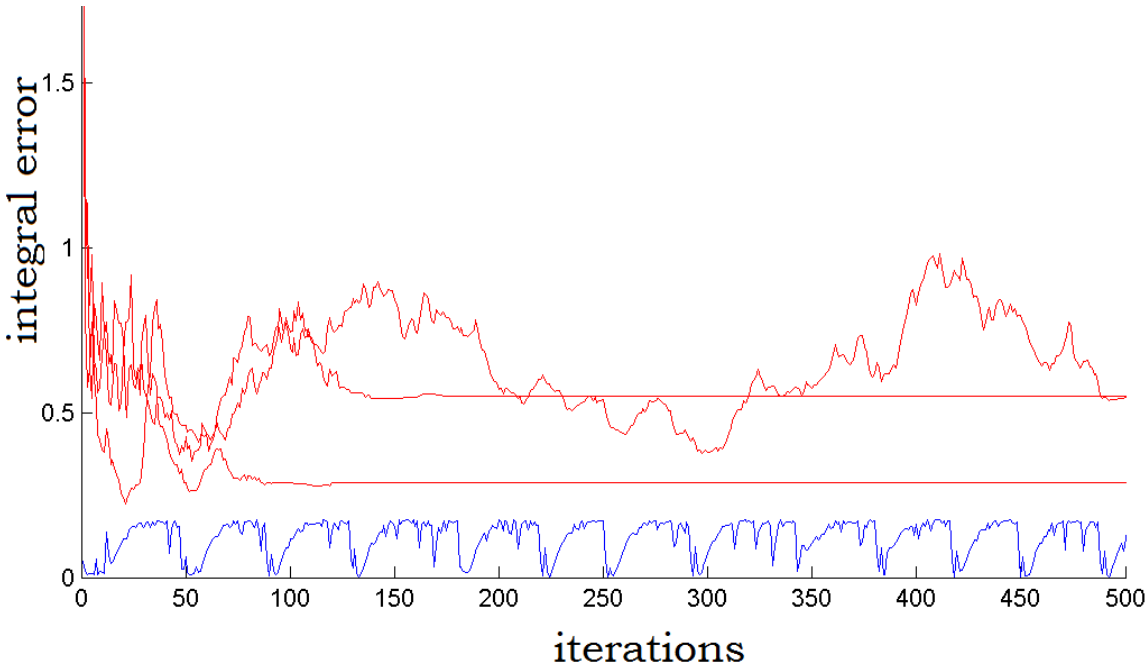

Figure 3.10: Convergence pattern of the δ_1 integral error for PCI, with and without the KK conditions

The integral error method illustrates these problems very well, because we see that a non-PCI solution converges to a profile which is still different from original distribution. This can be clearly seen from the previously shown figure 3.9. The previous considerations highlight another advantage of PCI compared to other traditional iterative algorithms: the amount of post-processing is kept to a minimum, and instead of being executed several hundred/thousand times, the code is run at most twice: a first time to understand the pattern of the error, and identify for how many iterations δ_1 and δ_2 are simultaneously minimal, and a second time, to display the profile for that optimal number of iterations.

Another advantage of PCI is the repeatability and reproducibility of the algorithm. Namely, for a given number of iterations, PCI will always yield exactly the same profile. We have seen in figure 3.10 that this is clearly not the case when the KK constraints are not present, and the uniqueness is therefore really a consequence of the implementation of initial and boundary conditions. This uniqueness we obtain is not a trivial result, because the KK conditions implement only a lower-limit on the phase, not a higher limit. When the algorithm overshoots a phase, it is not possible to detect it. This explains the residual error of the final output. However, this potential limitation does not affect the convergence pattern, and the

KK-conditions are sufficient to describe the convergence.

3.4.4 Behaviour for large β

We have seen that, in the figures 3.7 and 3.10, a plateau of the $\delta - 1$-values was present for the first few iterations. The existence of this plateau is due to the combination of three factors:

- The choice of the initial value of β
- The number of iterations progressed through
- The rate of decrease of β in the Adaptive Support block

The effect of this phenomena is illustrated in the two insets of the figure 3.11. Both pictures show the behaviour of the integral error with a large beta value starting at 20, and then decreasing through the adaptive support block like previously described. In the inset *a* of figure 3.11 , the two errors for the 120 first iterations is shown. The behaviour is stochastic and does not follow any pattern. Moreover, the two errors δ_1 and δ_2 never reach simultaneously a minimum as neatly as in the figure 3.7, and the integral error δ_1 stays most of the time around 10 %. In the inset *b* of the figure 3.11 however, which shows the integral error across the 400 first iterations, an interested behavior can be observed: around the 170th iteration, the stochastic regime observed in the inset *a* of the figure 3.11 turns into an oscillation regime, and becomes the one we have described in the figures 3.7 and 3.10. The "oscillation regime" starts when $\beta \approx 0.9$. This value of 0.9 is interesting as it has been noticed before that this value was stabilizing the HIO algorithm [47]. Now, we can understand why we had that small plateau we saw in the figures 3.7 and 3.10: they correspond to the end of the iterations 150-165 in the inset *b* of figure 3.11: in the figures 3.7 and 3.10, the plateaux were present because PCI was started with $\beta = 1$. This plateau corresponds thus to iterations for which β was decreasing but did not reach the transition value 0.9 .

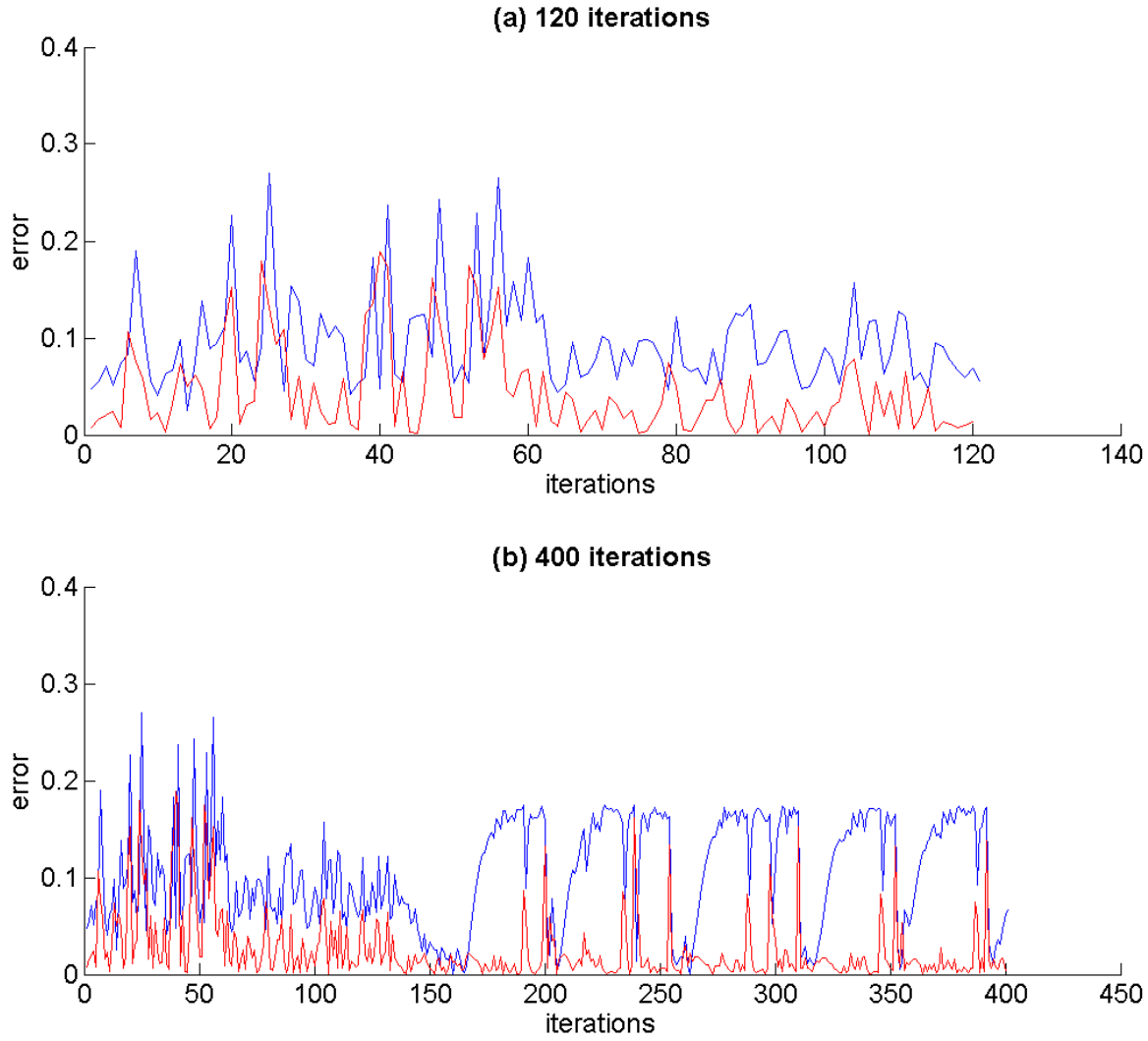

Figure 3.11: (a) The errors (in blue) and (in red) with a starting value of β =20 for 140 iterations – (b) The errors (in blue) and (in red) with a starting value of =20 for 400 iterations.

Another feature to note is that, when β is above the critical value of 0.9, we cannot state anymore that a good recovered profile would correspond to a minimization of the errors. To understand why, let us have a look at the figure 3.12. It illustrates the output of PCI after the 120 iterations of the inset a of 3.11, that is, when beta was still above the transition value. The figure 3.12 shows the final output phase, and the figure 3.13 shows the reconstructed profile. We see that the reconstruction is very accurate, but with many additional ripples that add up, and explains why the error was so large

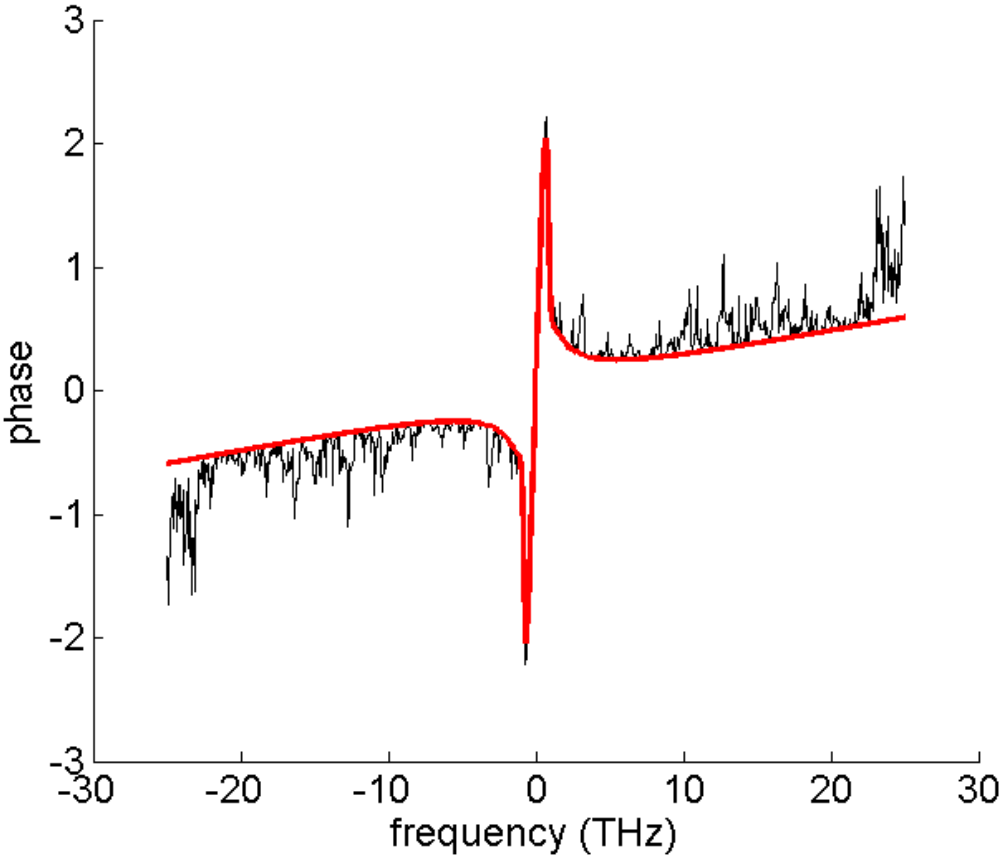

Figure 3.12: Output phase for a β starting at 20, after the 120 iterations of 3.11(a)

at the end of the 120 iterations of the inset a in 3.11. As a result, if we want to use the two error criteria properly, and state that "good profile=minimization of δ_1 and δ_2 ", we must make sure that PCI runs long enough to cross the transition value 0.9 .

3.4.5 Other examples of reconstruction

I will conclude this chapter by illustrating PCI briefly on some other examples of profile. Of particular interest I have studied the reconstruction of a Lorentzian function. Lorentzian functions have the form

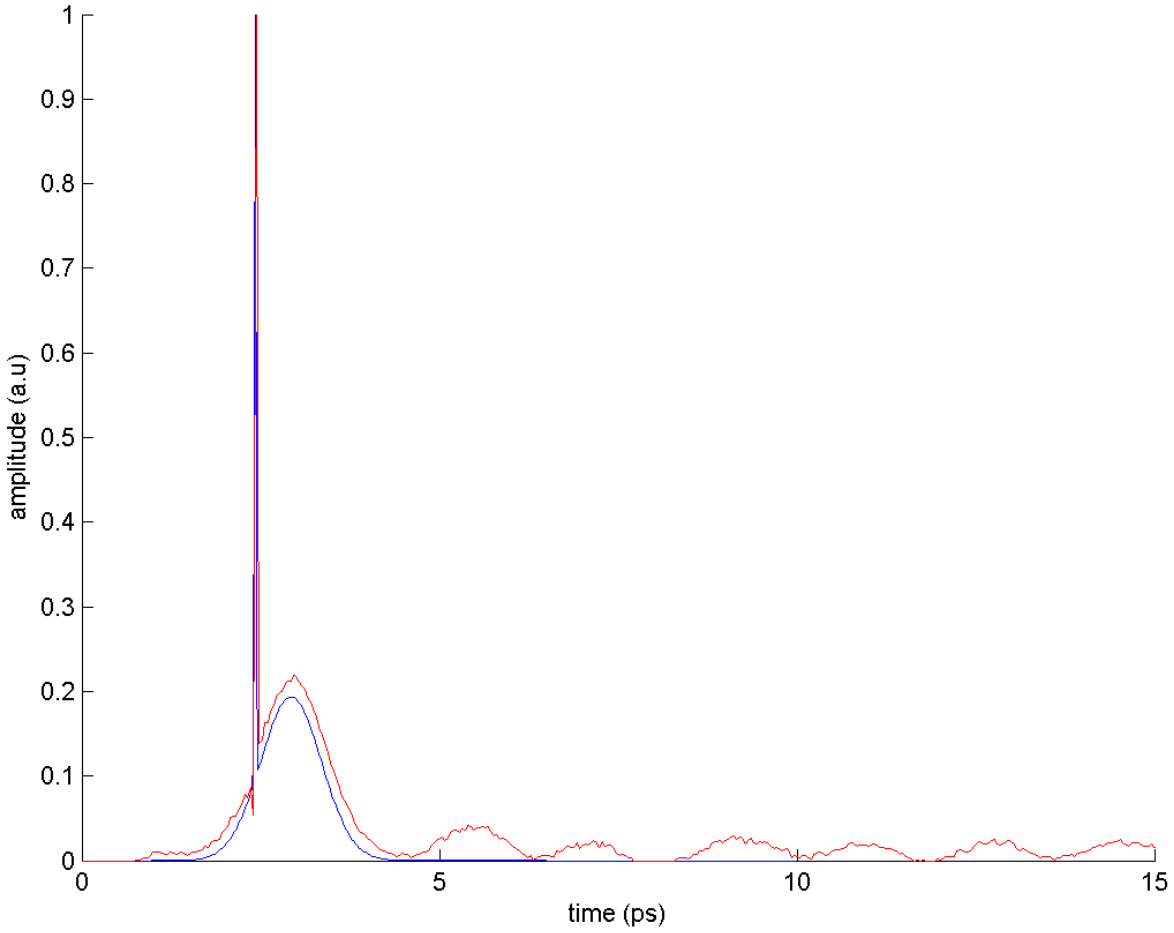

Figure 3.13: Output profile for a starting β of 20, after 120 iterations. Parasitic oscillations that extends up to 15 ps are present, and contribute significantly to the error, despite a good reconstruction

$$f(t) = \frac{1}{\pi} \frac{\alpha}{(t-\eta)^2 - \alpha^2} \tag{3.11}$$

From a rigorous point of view, they are not physical because they extend to infinity in both t-directions. They are called Breit-Wigner functions and play an important role in Particle Physics experiments, and as such, there is interest in their study. In this case, the profile to be investigated had the parameters $\alpha = 0.3, \eta = 0$

The results of PCI is shown in the figures 3.14 and 3.15. We see that the algorithm converges very quickly, and PCI gives a considerably better estimate of the profile than KK.

Another type of function of interest is the double Gaussian of a more traditional shape that

the sophisticated case we analysed in detail in this chapter. The set of parameters

$$A_1 = 1$$

$$A_2 = 0.6$$

$$\sigma_1 = 0.13$$

$$\sigma_2 = 0.21$$

$$\mu_1 = 0.64$$

$$\mu_2 = 1.64$$

defines a double Gaussian such as those that can be produced through a notched collimator at SLAC: the bases of the two Gaussians are not fully separated but their individual

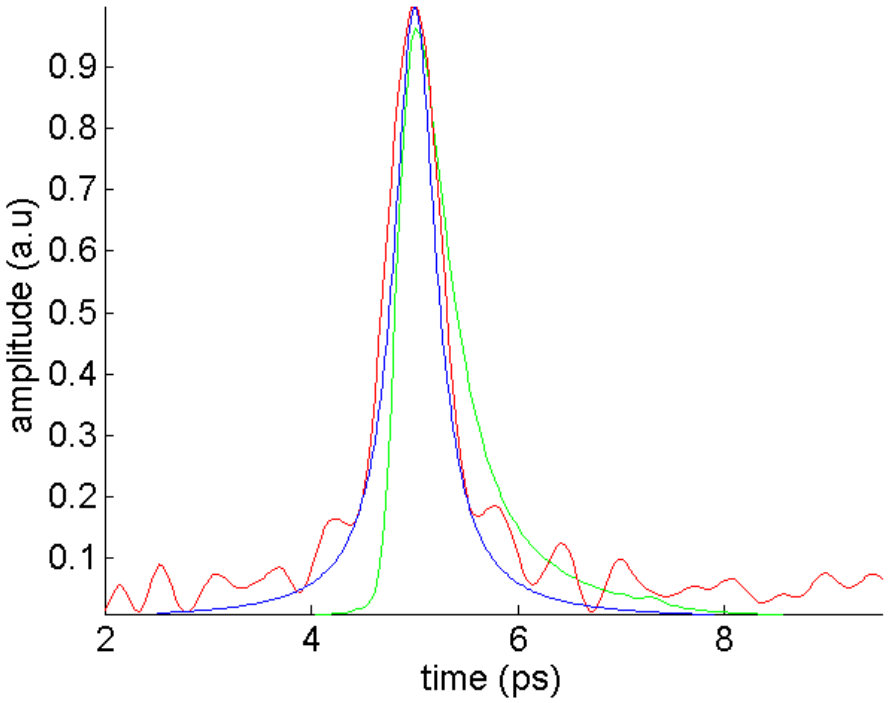

Figure 3.14: Reconstruction of a Lorentzian profile. Blue: Original Profile – Green : KK retrieval – Red: PCI retrieval

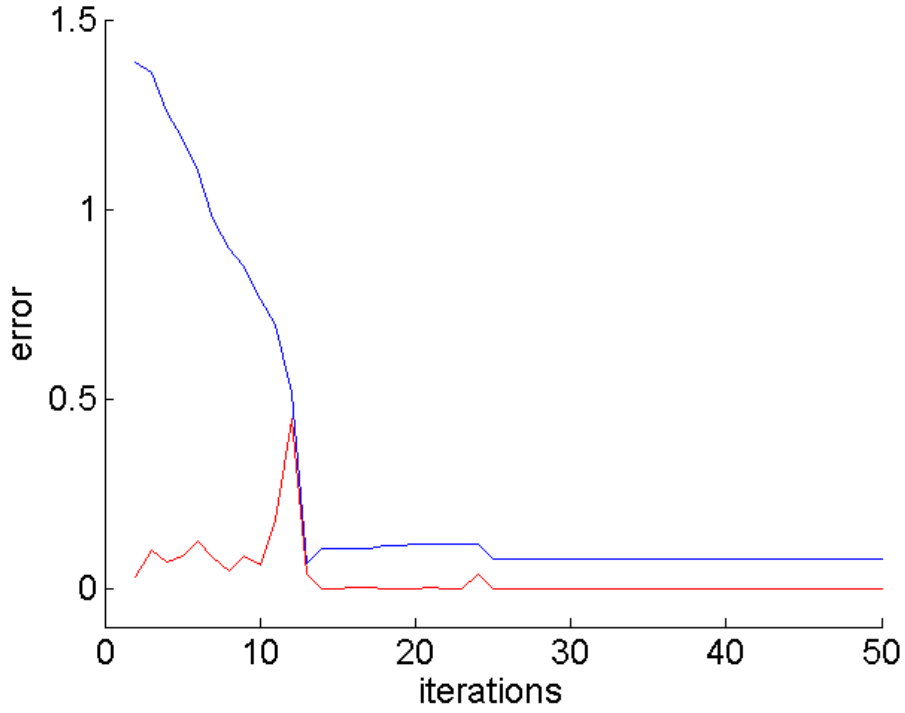

Figure 3.15: The integral errors. Blue : δ_1 - Red: δ_2

length is clearly resolved. Their profile is illustrated in the figure 3.16, as well as the KK and PCI reconstructions. We see that KK provides already an excellent recovery of the original profile, and the outcome of PCI shows that for cases where KK works, PCI does not deviate from the existing solution. From this, we conclude that PCI always provides a solution that is of same or better quality than KK when a Blaschke phase is present, but if the investigated function has no Blaschke phase, PCI can perturbate the KK solution and provide a slightly less accurate solution than PCI.

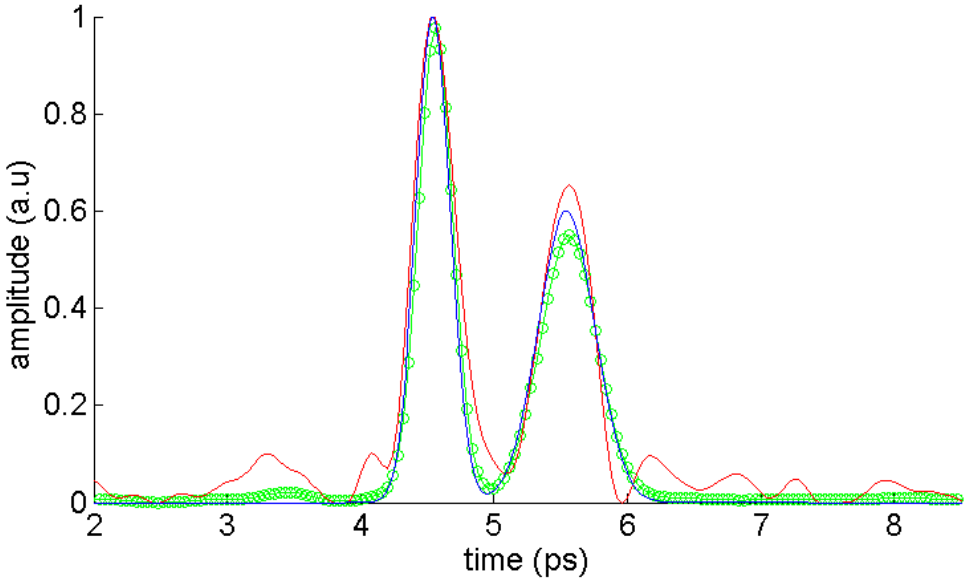

Figure 3.16: Reconstruction of a Double Gaussian profile at 27 iterations. Blue: Original Profile – Green : KK retrieval – Red: PCI retrieval

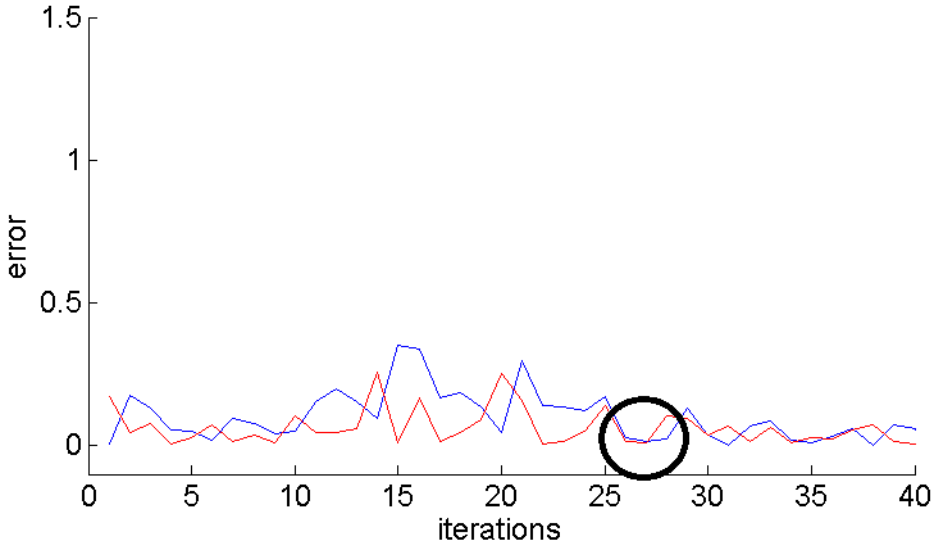

Figure 3.17: The integral errors. Blue : δ_1 - Red: δ_2

3.5 Summary of chapter 3

In this chapter, a new algorithm was constructed, called PCI. It implemented the information extracted from the Kramers-Kronig minimum phase, as initial condition and boundary condition to an iterative projective algorithm. It was shown that such a combination addressed

several of the issue previously identified in the literature with respect to one-dimensional phase retrieval. Sophisticated profiles could be reconstructed with a good degree of accuracy, and the estimate of this accuracy was provided with a new type of error that made use of experimentally known information about the charge.

Chapter 4

The experimental set-up

4.1 The FACET facility at SLAC

4.1.1 The SLAC National Accelerator Center

The set of experiments which will be discussed and their presented results, were carried out at SLAC, Stanford. Founded in 1962 under the name Stanford Linear Accelerator Center, it is the largest linear accelerator in the world, with the main linac having a length of 3.2 km. It has played a major role in the landscape of particle physics of the era ranging from the 1970-2000, with three Nobel Prizes in experimental particle physics. After the early 2000's, SLAC underwent significant changes with a gradual drift toward several projects dedicated to Accelerator Research as main goal, and not only as support for experimental particle physics anymore.

4.1.2 The FACET facility

The SLAC National Accelerator Laboratory has four Accelerator Test and Research facilities. One of them uses the main linac beam, and is the Facility for Advanced Accelerator Experimental Tests (FACET), and the three others are decoupled on separate sites. The FACET facilities are located on the first two-third length of the main linac, and is then

followed by a last third consisting in another facility called LCLS, as shown in the figure 4.1 below.

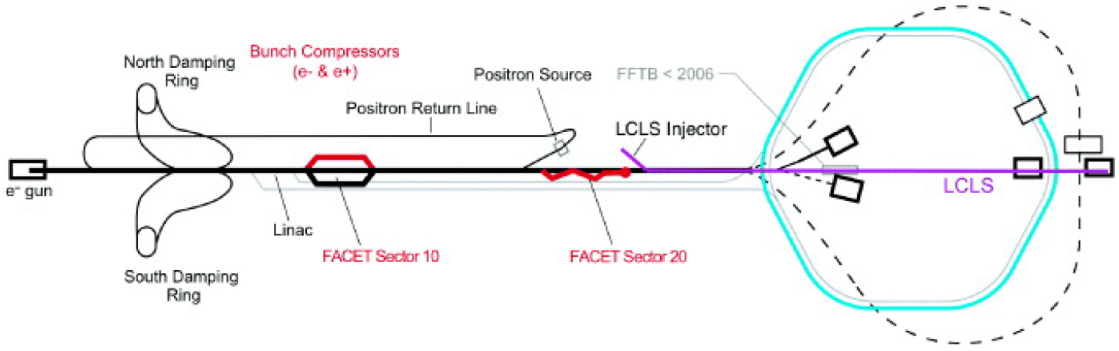

Figure 4.1: Overall view of the SLAC linac and highlight of the Sector 20 where is located the diagnostics experimental area. (Credits: SLAC)

The figure 4.2 shows the beamline elements and diagnostics of the main experimental area of FACET, located in what is called the "Sector 20". The total span in that picture 4.2 is approximately 90 metres long. During experiments, the beam is focused with a minimum waist in the region called the Interaction Point area (IP Area, see figure 4.2). FACET has five main areas of research:

- Plasma wakefield acceleration: the main program which motivated the current design of FACET.
- Dielectric wakefield acceleration
- Radiation generation, with a focus on THz range
- Ultrafast process in magnetic solids
- Beam diagnostic at THz scale

The experimental studies of Smith-Purcell radiation which I undertook, falls into the last category. The experimental set-up, and set of experiments conducted using this set-up, were identified as Experiment 203, or "E203" and this is how it will be referred to for the rest of this work.

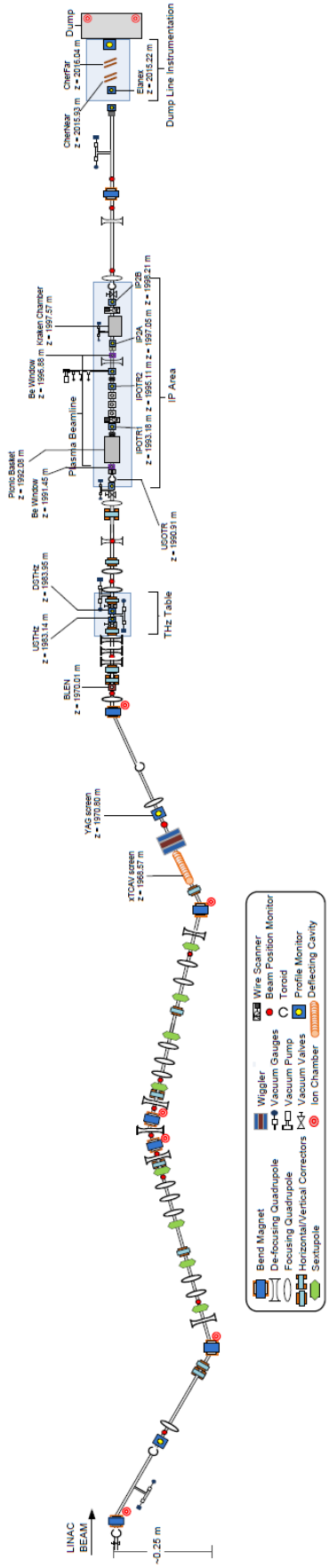

Figure 4.2: The Sector-20 section of the FACET facility at SLAC. The total length is approximately 90 m.(Credits: SLAC)

Because FACET also investigates the general problem of bunch diagnostics, the Sector 20 where my experiment was carried out, provides the possibility for the measurements of the longitudinal bunch length through two other experimental techniques, which were used to compare with the results observed from of E203:

a) A first experiment is similar to E203 technique, based too on coherent radiation spectral analysis in the THz range, but using transition radiation instead of Smith-Purcell. The THz radiation measurement device was known as a "THz table" and was located 10 meters upstream the IP Area. It consisted of inclined thin foil used to generate coherent transition radiation when the electron beam propagated through the foil. The radiation was collected by a complex system of off-axis parabolic mirrors and directed to a specially designed spectrometer with a pyroelectric joule-meter to calculate the energy, and a Michelson interferometer to calculate the frequency spectrum. The bunch profile was then reconstructed through the Kramers-Kronig technique. That experiment has been thoroughly described in [23].

b) Another device used to compare the bunch length yield with E203, is a Transverse Deflecting Cavity (TCAV). Its design has been extensively described in [24], [25]. A sinusoidal voltage V(t) is applied and, if the centre of bunch is synchronized to pass through the cavity at zero crossing, the front-end of the bunch will receive an upward-kick, while the back-end will receive a downward-kick. This will cause the bunch to longitudinally rotate as it propagates, and will hit a screen. The TCAV device is calibrated such that the deflection trajectory causes the bunch to hit the screen against its length (see figure 4.3). The length of the screen trace can therefore be used as an estimate of the longitudinal bunch length. A typical TCAV measurement can take from 30 min up to 1 hour, because the calibration of the deflection and trajectory must be adjusted to the current experimental conditions. Consequently, due to time constraints, it is not always possible to perform TCAV measurements: they are usually done at the start or the end of a shift, or when the bunch length must be changed during the experiment (for example if a change of bunch compression is planned during the shift).

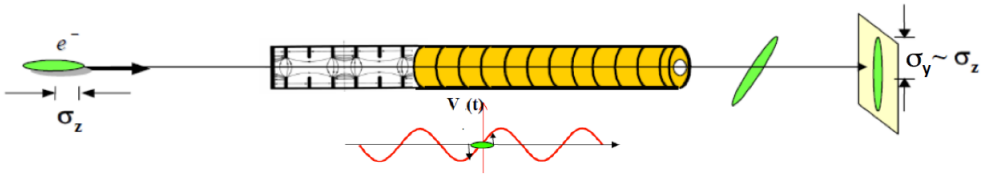

Figure 4.3: Principle of the transverse cavity bunch length measurement. (Credits: SLAC)

4.2 The Smith-Purcell monitor

I am going now to describe the Smith-Purcell monitor. Its main parts are:

- The vacuum chamber: where the beam interacts with the gratings.
- The optical system: it collects the radiation.
- The data acquisition system: converts the radiation into readable information.
- The control system: to allow the remote operations on the monitor.

4.2.1 The vacuum chamber

The vacuum chamber, pictured in the figure 4.4, is a sealed metal cage with eleven silicon windows ranging from $\theta = 40$ to $\theta = 140$ degrees. Its interior parts, pictured in the figure 4.5, consists in the three gratings and a blank. All four of them are mounted on a carousel. In order to measure accurately the beam-grating separation, a wire-scan was mounted too on the carousel: this was motivated by the fact that SLAC's two nearest wire-scans were located several metres away from the E203 monitor, and their precision did not allow precise determination of the beam position with respect to our grating. Mounting a wire-scan over the carousel solved this issue, and the detailed determination beam-grating separation will be described in the section 4.3.4.

The rotation mechanism of the carousel consisted of a main wheel with a set of metallic fingers, and a driver allowing accurate rotation in one direction only, by increments of 90

degrees. It is managed through a one-directional stage motor governed by the remote control system that will be described in the section 4.2.4 of this chapter.

Figure 4.4: The vacuum chamber with its 11 silicon windows, during a hardware operation I undertook with a SLAC technician (Juan Cruz, on the photo)

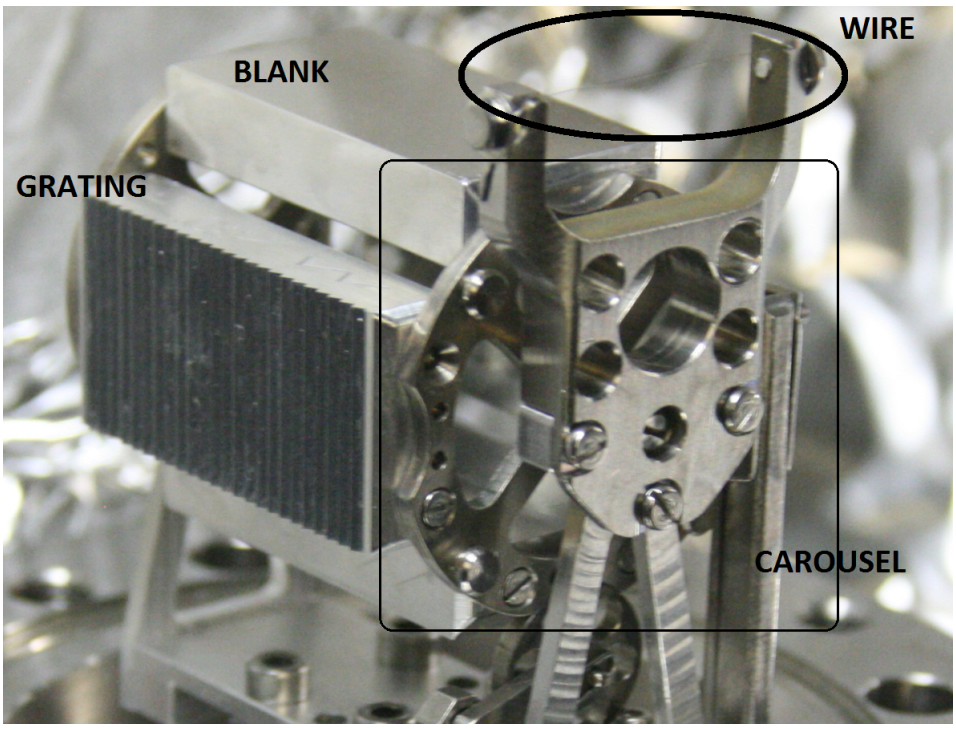

Figure 4.5: The inner parts of the vacuum chamber after unsealing: a grating, the blank, the wire-scan

The combination of gratings studied have varied through the years. The following table gives an indication of those that have been covered:

Table 4.1: combinations of grating studied

year	grating periods in microns
2013	50,250,1500
2014	50,250,1500
2015	250,500,1500

4.2.2 The optical system

The optical components of the Smith-Purcell monitor consists of three parts:

1. A remotely controlled ladder, illustrated in the figure 4.6, with five rows of filters. Four of the rows had a set of eleven filters, each one of them associated with a specific grating, and a fifth row is left empty. The filters of each row were positioned at 10

degrees of angular separation from each other, from 40 to 140 degrees. They were all located along a circular arc of 22 cm radius. The filters are designed to limit the background radiation, allowing only narrow band radiation to pass to the detectors. The filters were either waveguide-array-plates (WAP) filters, mylar or silicon-based thin films filters.

2. Winston cones. The Winston cones are non-imaging optical devices, used to act as light concentrator in order to maximize the collected energy to the detector. In the figure 4.7, we can see that their design consists of a parabolic profile with a cylindrical symmetry over a vertical axis, ending with a 2 mm diameter hole at the parabola vertex. Winston cones also act as filters, allowing only light arrays incident on the cones at ± 3 degrees to reach the detectors, ensuring that the detected radiation is essentially parallel.

3. Pyroelectric detectors of the ELTEC-400 family. These commercially affordable detectors are usually preferred for their performance over a wide frequency range. They are capable of detecting wavelengths from 0.1 microns, up to mm-scales. Two limitations of these detectors is their sensitivity requiring large signals, and the fluctuation of responsivity which can reach a maximum 50% uncertainty of any nominal measurement, as stated by the manufacturer. Both the sensitivity and the responsivity are sources of systematic errors, which must be taken into account in the analysis, in addition to the statistical errors originating from the counts distribution during a data taking.

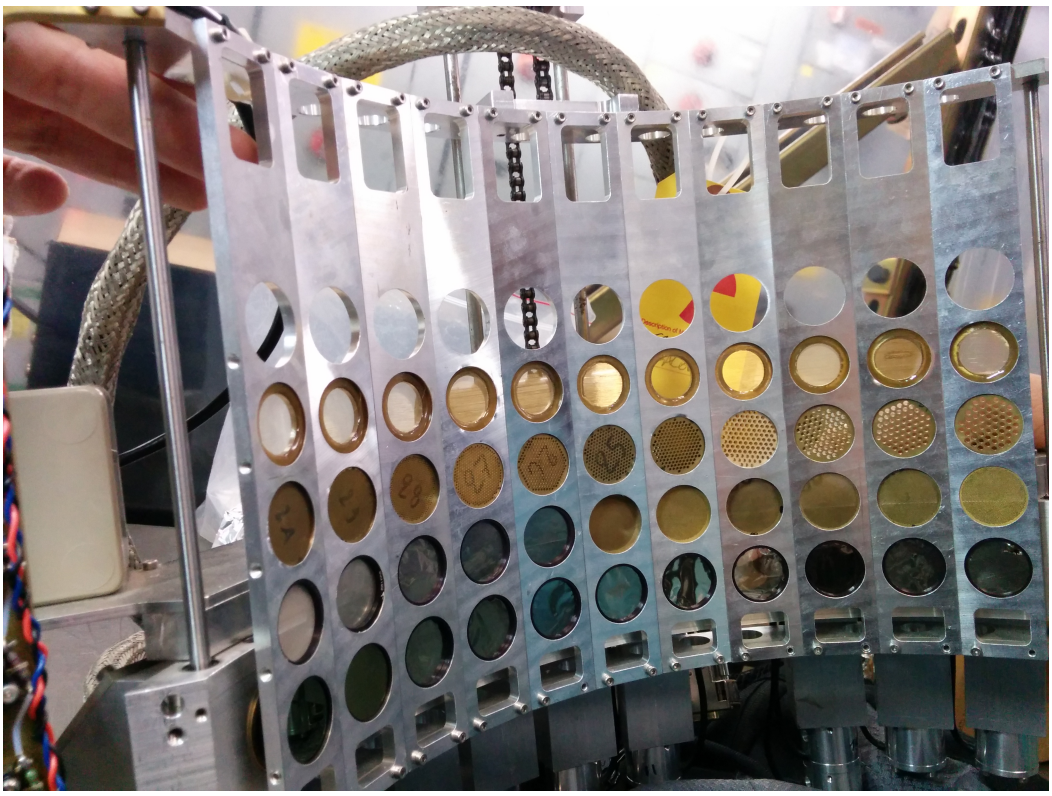

Figure 4.6: The 11 filter ladders

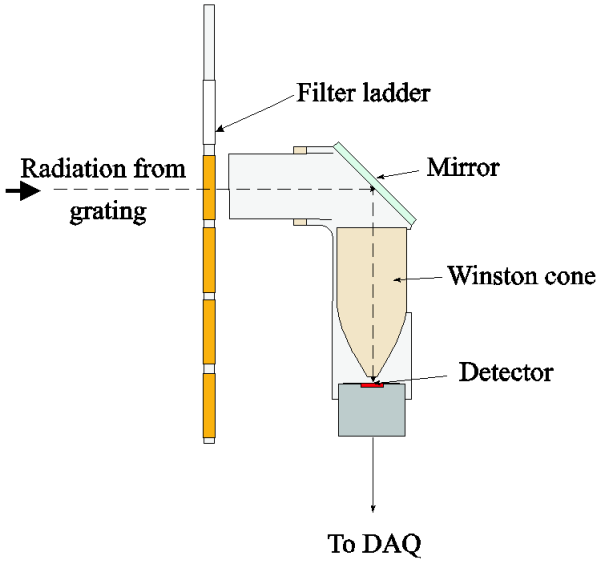

Figure 4.7: Schematic of the optical system (Courtesy E203 Archives [52])

4.2.3 The data acquisition system

The data acquisition system consists of a Field-Programmable Gate Array (FPGA) board designed in Oxford, whose main task is to allow beam-synchronous measurements. Since

the FACET facility at SLAC can operate at various repetition rates (1 Hz/5Hz/10 Hz/ 30 Hz for bunch lengths smaller than 1 picoseconds), the FPGA must accommodate the fact that the repetition rate is not necessarily known in advance. In order to do this, the FPGA data taking rate is synchronized to the FACET repetition rate at the beginning of each shift, through the following two-step process:

1 When the FPGA is switched on, a temporary data taking is activated at a very high rate of 250 kHz, the frequency of the reference internal clock of the FPGA. This temporary data taking is recorded into a buffer in the memory of the board. Because of the large frequency of the clock, only a very tiny amount of temporary data can be stored: 32 values for each detector.

2 In these temporary stored 32 values, the last 16 values and first 16 values are compared: if they record the same amount of counts, this means that no radiation has been detected in the upstream pyrodetector. But if the first 16 and the last 16 exhibits a sharp difference, it means than the mid-value corresponded to the passing of a bunch: this means that the triggering of the FPGA data taking is synchronized properly with the repetition rate of the accelerator.

A natural question that arises is “when do we know that the bunch passing coincides exactly with the middle of the 32 temporary data taking”? The answer is: we don’t know, and we can’t. So an additional mechanism is needed: SLAC gives the possibility to implement a varying “delay” parameter between our FPGA triggering

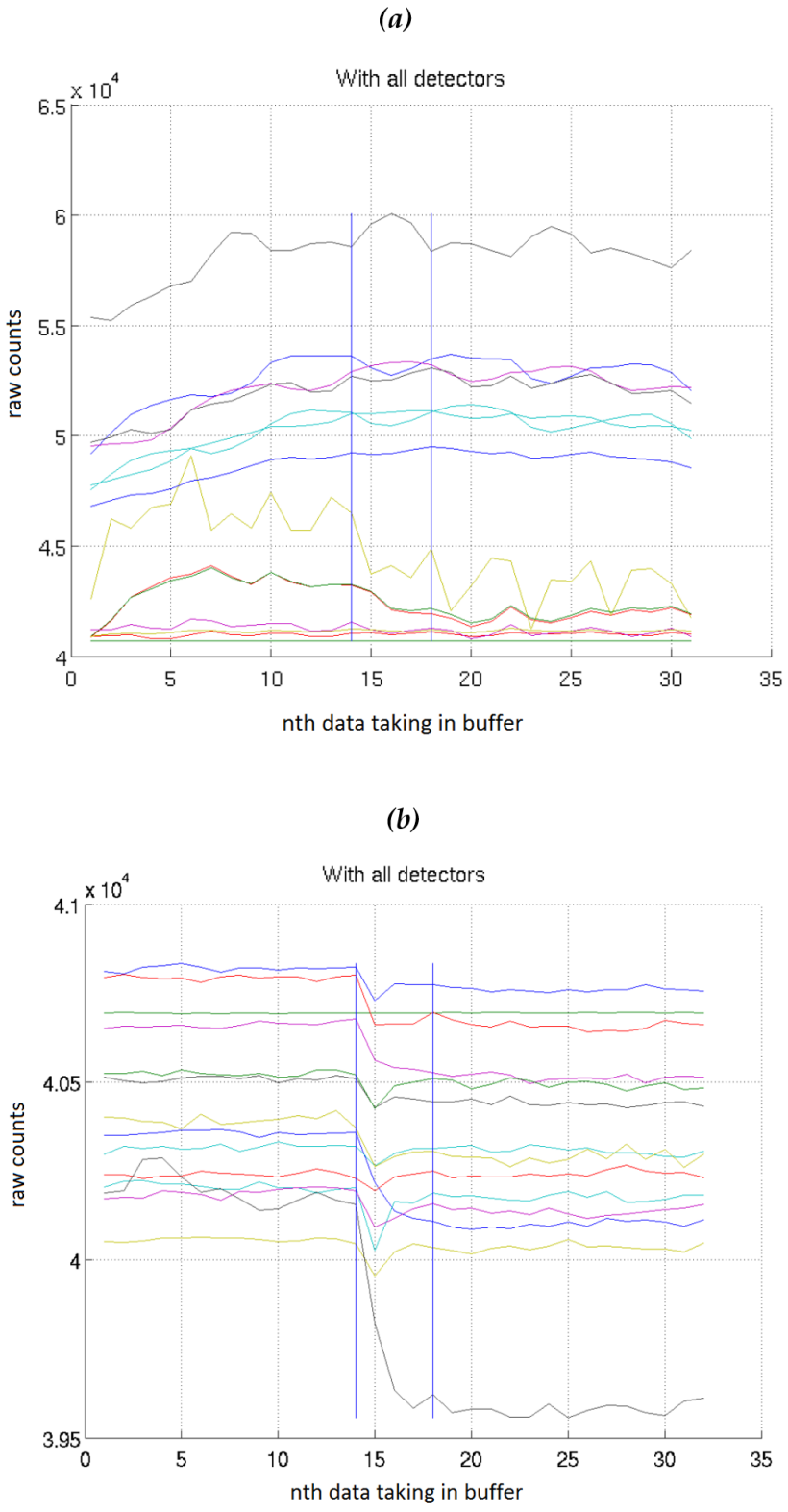

Figure 4.8: Effect on the delay parameter (a) non-synchronized trigger (b) partial synchronization (E203 Collaboration/ May 2015 shift - plots from N. Delerue)

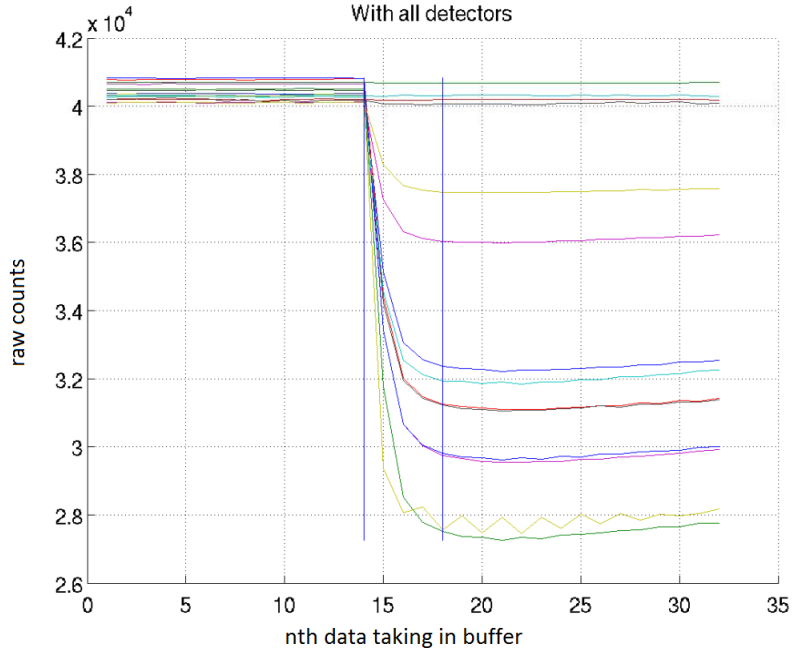

Figure 4.9: synchronized data taking with the bunch (E203 Collaboration/ May 2015 shift - plot from N. Delerue)

and the passing bunch. Using a telnet connection that acts as probe in the DAQ, we monitor the data flow, and analyse it in real time with a MATLAB script, until a value for the "delay" parameter is obtained, for which the FPGA and the passing bunch are synchronized.

This synchronization mechanism is illustrated in the figures 4.8, 4.9: in the inset *a* of thefigure 4.8, the trigger is not synchronized with the bunch repetition rate, so a comparison between the first 16 and last 16 values do not show any difference. The inset *b* of the figure 4.8 also shows a non-synchronized situation for a better delay parameter: here, a slight difference is noticeable and suggests a better triggering than in the inset *a*. An improvement leads to the figure 4.9, which illustrates a beam-synchronous data taking where the optimal delay parameter has been found for the local beam condition: the DAQ is properly calibrated and ready to be used for a shift. To summarize the previous considerations, it is always possible to synchronize the data taking with any repetition rate: one only needs to adjust the delay parameter, using an automated script that analyses the flow of a telnet connection monitoring what happens in the FPGA. The delay parameter is set in an "Event Generator" which is located 200 metres from the DAQ. This Event Generator is networked to the SLAC database, and this makes possible to set up the delay from the E203 experiment control

room, in the beginning of a shift.

At the front-end of the DAQ system, the data collected from the FPGA are written into a series of text files which are subsequently analysed. One of the technical challenges comes from the fact that these data files receive written information, not only from the FPGA, but also from a certain number of other channels communicating with other accelerator diagnostics, such as upstream and downstream toroids or voltage checking signals from a nearby VME Crate. These additional diagnostics information are sent to the file by the SLAC's own control environment, called Experimental Physics and Industrial Control System (EPICS). Despite its name, EPICS manages not only Control systems, but also (like here) DAQ's and distributed databases. Because two different systems write to the datafile (the DAQ and EPICS), we must make sure that the information sent from EPICS does not "jam" the datafile by sending information simultaneously with the DAQ: this is done by using a driver that manages the interaction between EPICS, the DAQ and the Accelerator. This driver, programmed in C++, has been written for E203 by Zenon Szalata.

These raw data files contain the record of ADC counts for typically 100 bunches (more occasionally 20 or 40 bunches), for each of the 11 detectors. A further single output data file is then generated, which provides a unique number for each detector, averaged over all the measured bunches of this particular data taking. It is this "averaged file" that shall be used for analysis. For this purpose, these raw averaged values must be converted to energy. This is done by first correcting them with "transmission factors", then converting through a DAQ calibration of 35 pJ/ADC count. The transmission factors are an estimated correction which should be considered to account for losses and finite distance between grating and detectors. The transmission factors account for the following losses, and for each different wavelength:

1. the transmission through the silicon window of the vacuum chamber
2. the transmission through the filter
3. the transmission through the elbow

4. the transmission through the Winston cone

5. the transmission through the pyroelectric detector

6. after all this, finally a far-field correction is estimated

This makes each data files requiring a set of 66 numbers to reconstruct the actual raw counts before losses. The DAQ calibration factor is applied at the end, to obtain the energy, making this final output ready for data analysis.

4.2.4 The control system

The Control system is the hardware part that governs the remote control of the grating driver motor and the filter driver motor. The central part of the system is a XPS Newport Controller, capable of providing accurate motion despite very high level of noise radiation in the tunnel. A schematic of the control system is presented in the figure 4.10. The two motors of the Smith-Purcell monitor are connected to an electronic board placed in the main tunnel

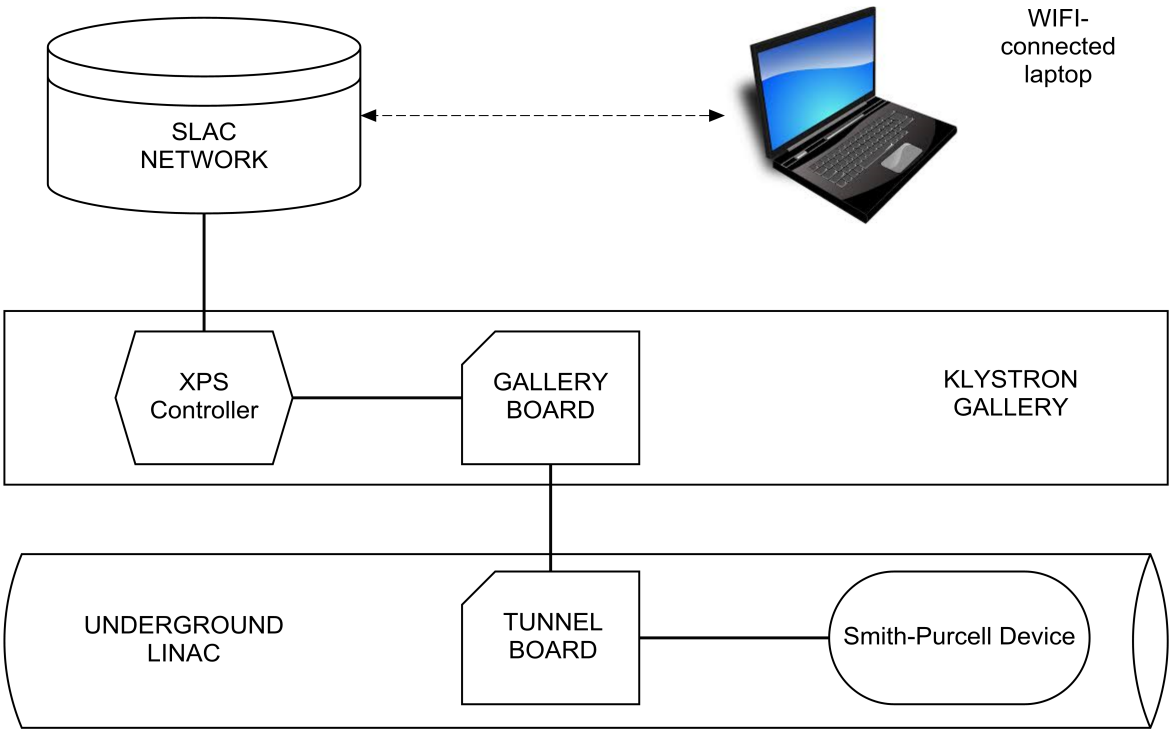

Figure 4.10: Schematic of the control system

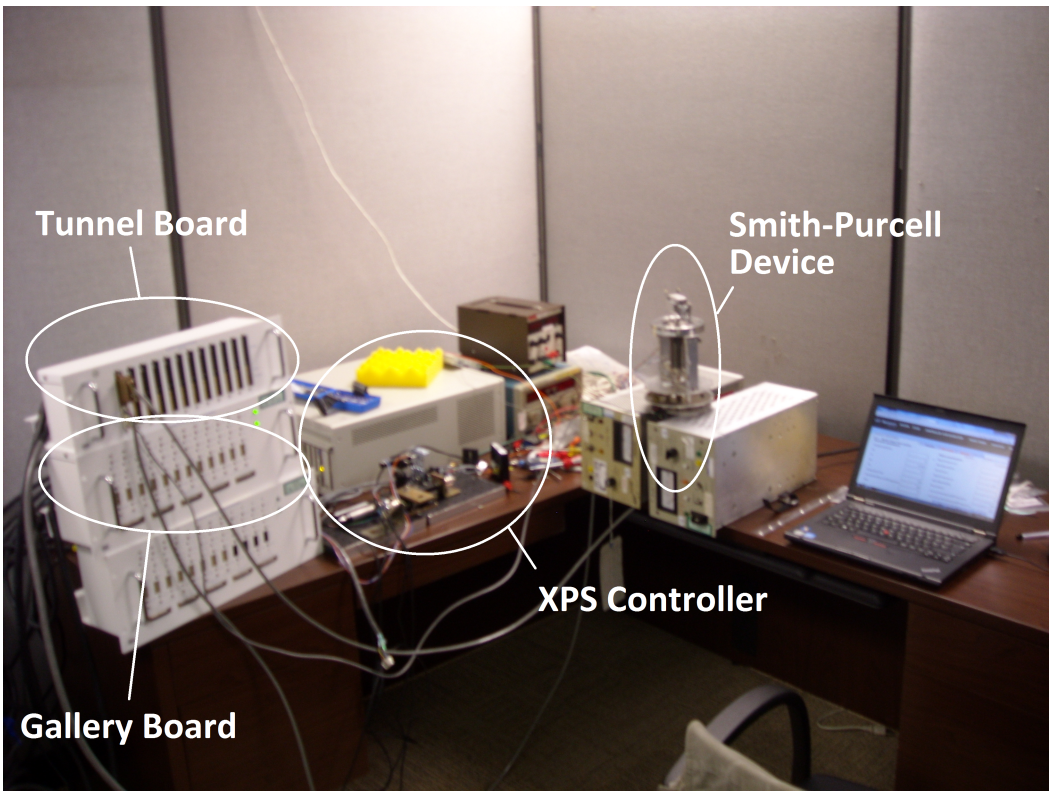

Figure 4.11: The E203 control system in the test-stand of the B34 Engineering Building, in October 2013

of the linac, the "Tunnel Board" of the figure 4.10. That tunnel board is connected to the monitor using thick noise-insulated cables, branched to another electronic interface board located in the klystron gallery, the "Gallery board" of the figure 4.10. The "Gallery board" is located only a metre away from the Controller, which is connected to all the network components : the Event Generator, the Digi Server, the wireless serial controls, etc. If the tunnel and gallery electronic boards are interfaced properly, any laptop with network-access to SLAC facilities can connect to the system, and control the motions of the filter and grating drive. The figure 4.11 is a photograph taken during one of my configuration setting up of the control system, in the test facilities of the Engineering Building.

Once the electronic boards are set-up, the control system operates as following using MATLAB scripts: 1 The user defines a target position to be reached by the motor, with respect to a configured frame of reference. This target position is called the Set Point, and is located anywhere between the two mechanical limit switches of the motor. 2 The XPS Controller compares the Set Point to the Read-Back Value, which is the current position of the motor

in the frame of reference. 3 If the Read-Back value is different from the Set Point, the motor adjusts the current position until it reaches the Set Point. This requires a comparison of Set Point/Read-Back at regular time intervals, through what is called a Feedback Loop, the XPS Controller is fed back with the current Read-Back value for regular comparison with the Set Point, until this Set Point is reached, within a predefined tolerance precision. In theory, the XPS Controller has the capability to reach a target position with a precision of nanometre-scale. But in practice, the precision is strongly limited by the type of motor used. For the E203 experiments, motor of McLennan family were used, and consequently, in good experimental conditions, the XPS could allow micrometre-scale position accuracy.

4.3 Nominal beam parameters

4.3.1 Preliminary comments of the structure of the signal

FACET has a wide range of beam diagnostic devices to monitor the behaviour of the whole machine. In most cases, the required beam parameters were provided during E203 shifts by the accelerator specialists who were overseeing the accelerator operation from the control room. The parameters needed to analyse experimental data are:

- the beam energy
- the beam charge
- the normalized emittance
- the transverse dimensions.
- The beam-grating separation : the only one which has to be determined experimentally, and not provided by the control room operators.

The beam energy at FACET is known from design, and has a typical nominal value of 20.35 GeV. I shall give now some more detail on the other parameters

4.3.2 The beam charge

The beam charge is measured in terms of numbers of electrons, the order of which is typically 1010 . It is provided by two toroids: the first is located upstream of the Smith-Purcell chamber, and the second one is located immediately downstream. The beam charge is a critically important quantity, because the retrieved profile, when integrated over time must be equal to the charge. The cases when charge variation is large are discarded as they result in erroneous profile reconstruction.

The figure 4.12 illustrates a typical situation that can take place during the experiment. It is a screenshot of the so-called "Striptool": a window monitoring the fundamental parameters of interest. The charge of the upstream toroid is indicated by the blue thick line, and we can see that it is relatively constant during the first half of the screen, about 1.8×10^{10} electrons. The long vertical green lines represents the data taking triggers activated at the FPGA by an automated MATLAB script. Toward the middle-right side of the screen, the charge suddenly drops flat because of an unexpected beam loss. Due to human factor, there is a time delay to interrupt the automated data taking. During that delay, data continue to be taken, but they are meaningless. In the example given in the figure 4.12, we see that the DAQ continues to take data twice before it has been interrupted manually. These junk data files are deleted during the post-processing analysis. The records such as this Striptool, help to identify exactly which time-stamped data have to be rejected in the analysis.

4.3.3 Normalized emittance and transverse dimensions

The normalised emittance is usually in the range 56-60 mm.mrad and there has been essentially no change in this quantity during all the years of this thesis. As for the transverse dimensions, they are provided by optical transition radiation screens located near the interaction point, such as the device OTRS:LI20:3075. Unlike the normalised emittance, which was relatively constant, the transverse dimension can fluctuate several times during a shift. For example, the figure 4.13 is a screenshot from the SLAC FACET e-log that shows how the transverse dimensions.

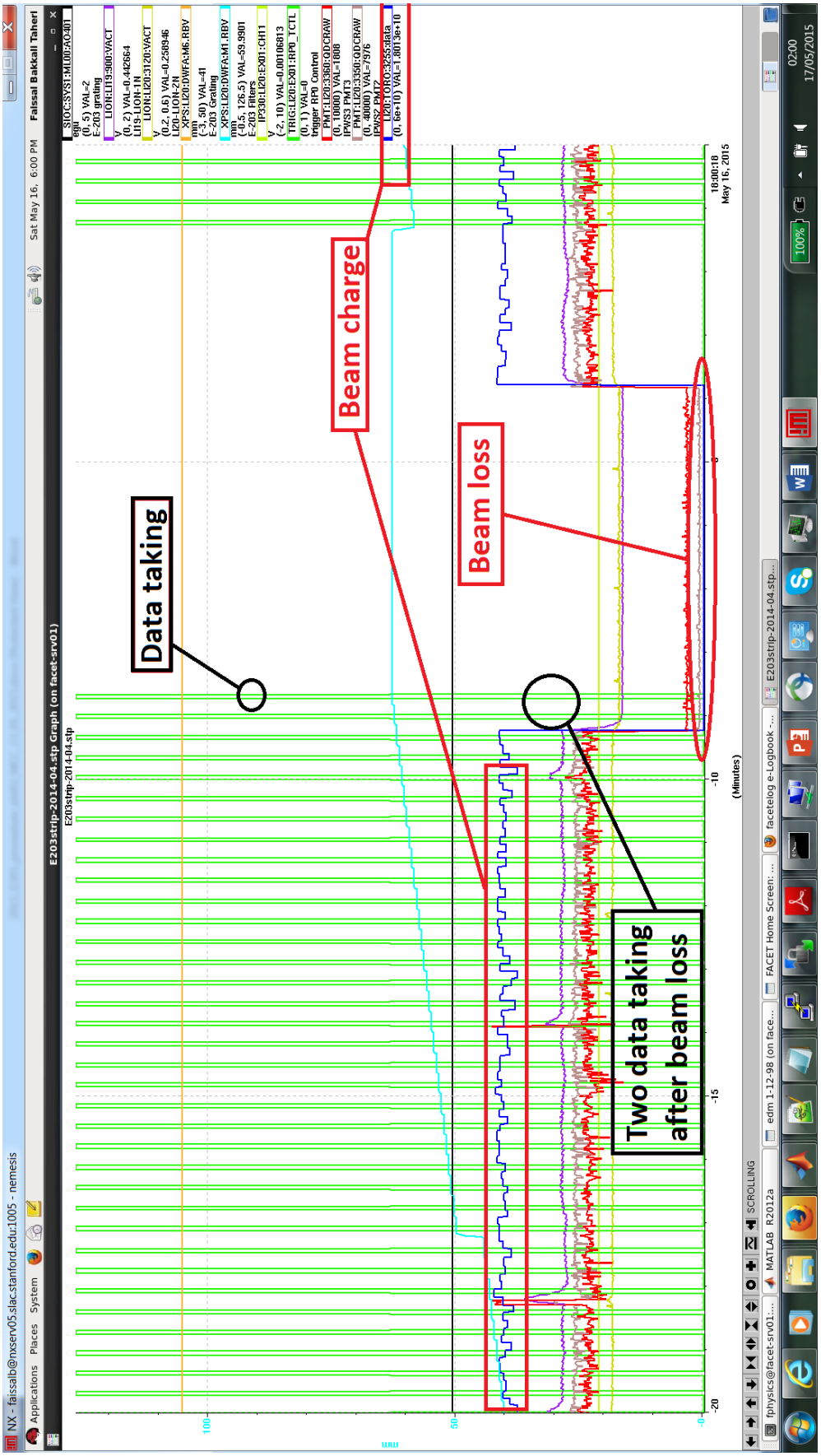

Figure 4.12: Behaviour of the charge (blue line) and data taking: the charge is relatively stable, until a beam loss takes place.

are given by the x-rms and y-rms qantities: we see that within just a span of ≈ 50 min, the rms in the x direction goes from 244 microns at 1.46am to 210 microns at 2.38am, while the rms in the y-direction goes from 84 microns to 155 microns in the same timespan. In general, the pattern that emerges from the various shifts, is that the transverse dimensions stay in the range 50-600 microns.

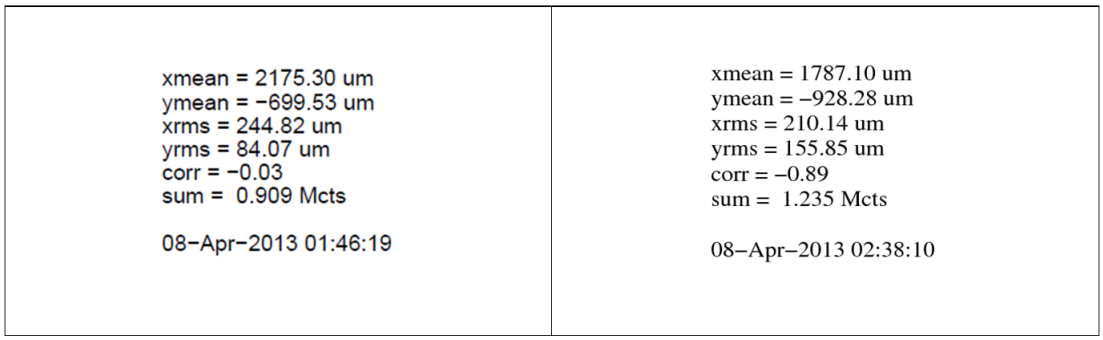

Figure 4.13: Variation of the transverse bunch dimensions in a ≈ 50 minutes timeframe during a shift

4.3.4 The beam-grating separation

The beam-grating separation is another of the most critically important parameters. This quantity is not provided by SLAC but is determined through a wirescan measurement, carried in the three following steps, and illustrated in the figure 4.14:

Step 1: The wire mounted on the carousel is brought forward to the beam at a speed of 0.05 mm/s. This initial stage is the "fast-forward" motion: when the wire crosses the beam, a Gaussian peak appears in the Striptool. This allows an initial estimate of the beam position, with respect to the coordinate system of the grating drive motor.

Step 2: The wire is brought backward slightly above the upper limit of the initial estimate, and from there, the wire is retracted to its initial position occupied at the start of Step 1, at a speed 2.5 times slower (0.02 mm/s), which is why the Gaussian has a larger width in the 4.14. This allows a precise determination of the beam position. The advantage of running the wirescan twice through a fast-forward/slow-backward combination, instead of just one slow motion, is that it helps detecting instability of the beam position at minimum waist: in

such a case, the positions found in step 1 and step 2 would not match. Such beam position instability happened in one of the shifts of the 2014 run.

Step 3: since the wire is separated by the top of the grating by a 9.7 mm distance, the grating motor must be moved near the position previously found by the wire, hence a final forward motion in the figure 4.14: the grating is then near the beam, with a beam-grating position now well-identified.

The determination of the beam-grating separation was a task that exemplifies the teamwork during the E203 shifts: the motion was done through the control system programs I had previously written, and interfaced with the XPS, while the precise determination of the beam position from the collected data was the task of Dr Barros. Her tasks involved also the mounting of the wire-scan on the top of the grating prior to the experiment.

4.4 Summary of chapter 4

In this chapter, we have described the hardware components of the time-profile monitor used in the FACET facility at SLAC: the optical system, the control system and the data acquisition. The communication between the detection of Smith-Purcell radiation and creation of datafiles have been presented, and I have finally overviewed all the parameters needed for data analysis obtained from the SLAC control room, and explained how the beam-grating separation was determined using the E203 setup

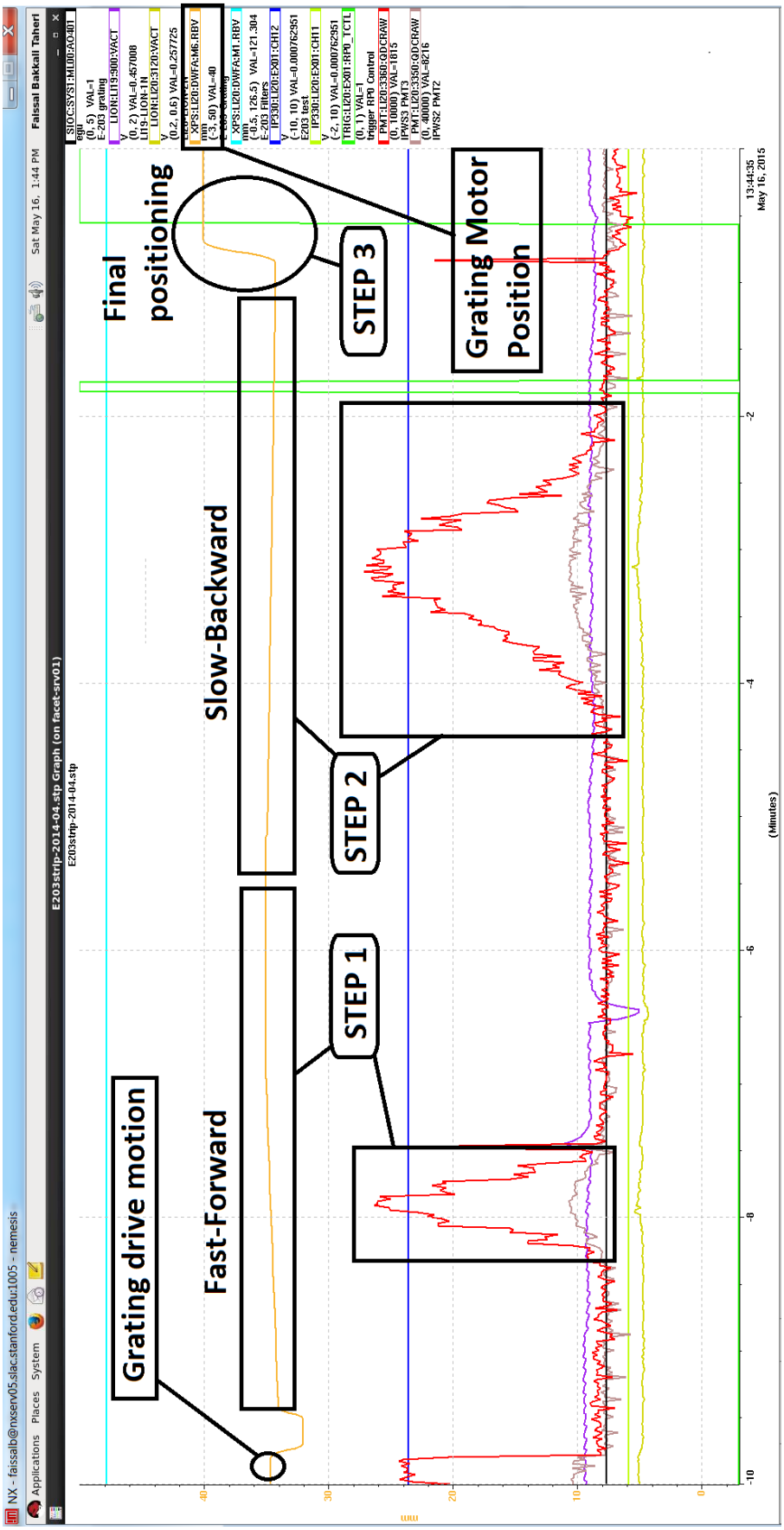

Figure 4.14: Determination of the beam-grating separation through the mounted wire-scan measurement.

Chapter 5

Experimental results

5.1 Bunch length diagnostics

In this section, the main results regarding the bunch length diagnostics will be presented. We start first with the experiment carried in May 2015, because it is the most thorough study we carried out, and the only one during this PhD where reconstructions have been studied as a function of distance. We have taken measurements when the beam was at five different distances from the grating: 2.24 mm, 3.24 mm, 4.24 mm, 6.24 mm, 8.24 mm, for the 1500, 500, and 250 microns gratings. The presentation of those 2015 data will then be completed with results from earlier years, where the aim was to reconstruct the time profile for various bunch configurations.

5.1.1 General preliminary comments

A first question that rises from the data is whether it is meaningful to present the whole set of distance analysed. The figures 5.1 and 5.2 help answering. The insets of figure 5.1 show the ADC counts that are obtained at data taking, in the case of the 0.5 mm period grating: the contributions from the grating alone and the blank are shown in the insets a and b of 5.1 respectively. The subtracted signal is then shown in the inset c. In all these plots, we see that the signal is more intense for the small beam-grating separations, and then decreases

significantly as the grating moves further away from the beam. This behaviour is due to the fact that the coupling between the electron beam and the grating, becomes weaker as the beam is moved away from the grating, and the surface current becomes smaller accordingly, leading to weaker Smith-Purcell signal.

A first feature that appears in the inset c of figure 5.1, is that the subtracted signal is not significantly different at 4.24, 6.24 and 8.24 mm of beam-grating separation: the signals at 6.24 and 8.24 mm are very close to zero, and the 4.24 mm is above them only at very specific regions (90 degrees, 110 degrees). Furthermore, at all these three distances, we see that the error bars are overlapping for many θ angles. To understand if the measurements at large beam-grating separation such as 6.24 or 8.24 are really physically meaningful, it is useful to have a look at the behaviour of the error. Because the arithmetic mean of counts at a given θ changes with distance, we must compare the relative error, instead of just looking at the standard deviation. This information is provided separately in the figure 5.2. This figure 5.2 shows that the relative error becomes very large with distance, up to two orders of magnitude. For this reason, in the following study on time profiles, only the data at 2.24, 3.24, 4.24 mm of beam-grating separation will be presented. This choice will be supported by the fact that, as I will show later in this work, the quality of the time profile reconstruction of a bunch at 4.24 mm from the grating, is much poorer than for the time profile reconstructed from a beam located at 2.24 mm from the grating. All this suggests that we focus on the data obtained at the nearest three distances: 2.24 mm, 3.24 mm, and 4.24 mm of beam-grating separations.

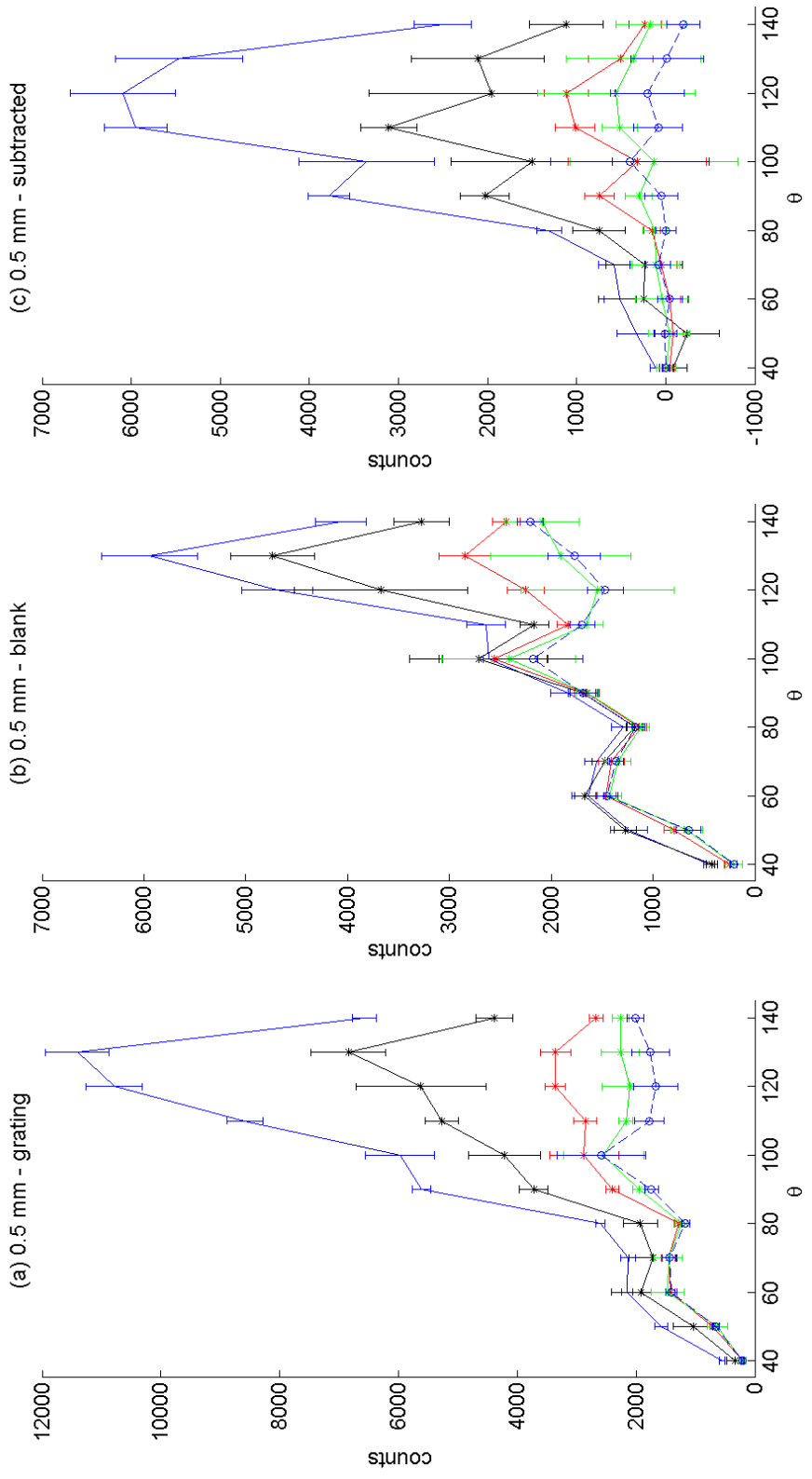

Figure 5.1: measured signal as a function of the beam-grating separation. Solid Blue line: 2.4 mm – Black line : 3.24 mm – Red line: 4.24 mm – Green line: 6.24 mm – Dashed Blue line: 8.24 mm

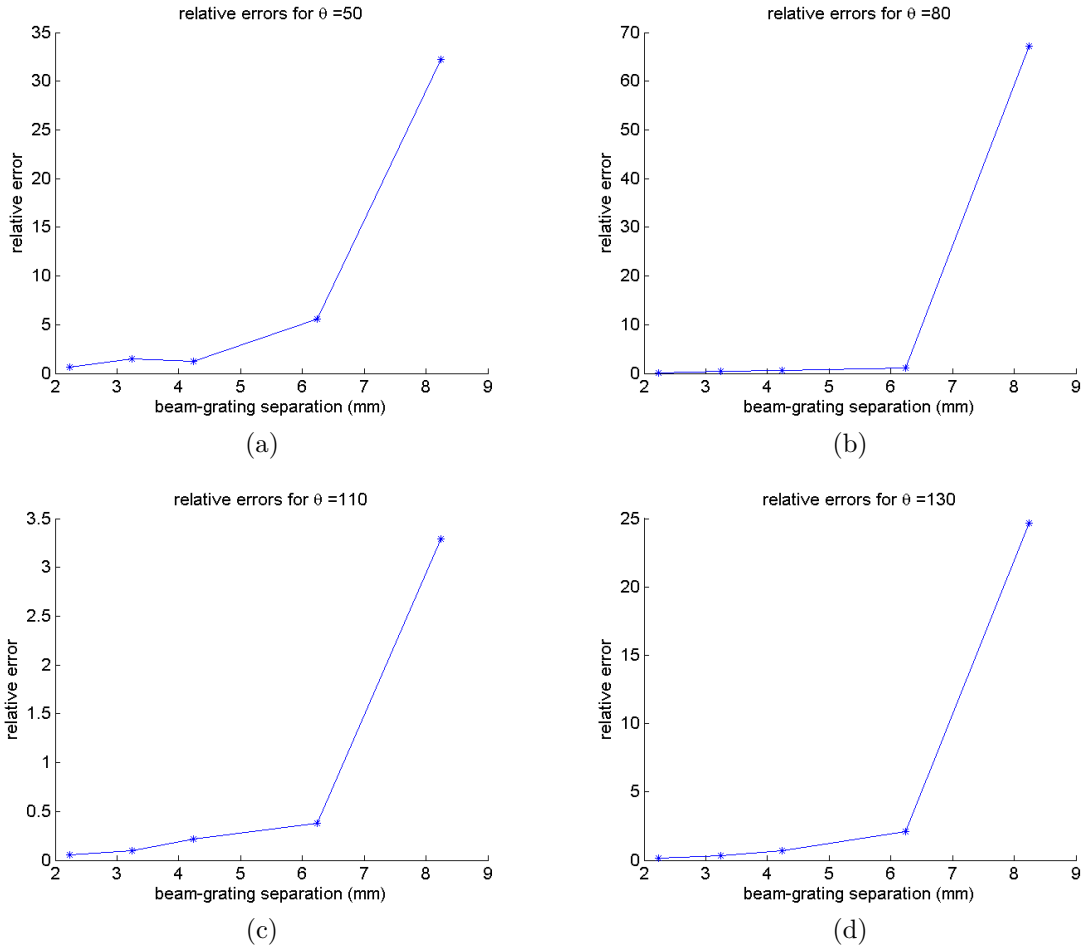

Figure 5.2: Dependence of the relative error with distance, for various θ angles

As we just mentioned, the figure 5.1 shows that the amount of detected Smith-Purcell radiation at each wavelength becomes smaller when the beam is far from the grating surface. This was investigated more closely by examining the dependence of signal intensity with distance, at fixed θ . The figures 5.3, 5.4, 5.5 show the behaviour of the raw counts against distance at three different θ angles, at 70, 90, and 120 degrees respectively, for the net cSPR of the 500 microns grating. First, it should be noted here that, rigorously speaking, pyroelectric detectors used are measuring energy and not counts. But because those plots show situations at a fixed θ , the actual energy measured on one hand, and the raw counts collected by the DAQ on another hand, are only differing by the same multiplicative factor, and therefore any pattern in energy reflects immediately on the raw counts.

Table 5.1: Fitting parameters through a single exponential and a sum of two exponentials. The parameters A and a in the third column, are the same than in the second one.

θ	$A\ \exp(ax)$	$A\ \exp(ax) + B\ \exp(bx)$
70^o	$A = 4319$ $a = -0.8986$	$B = 2.495$ $b = 0.4409$
90^o	$A = 18460$ $a = -0.7045$	$B = 0.1841$ $b = 0.4539$
120^o	$A = 54580$ $a = -0.9836$	$B = 37.34$ $b = 0.2505$

With this in mind, we can now have a closer look to the figures 5.3, 5.4, 5.5. All of them show a fit of the data using a single exponential, compared against another fit with a two-sums exponential. The parameters found for the three fits are presented in the table 5.1. The figures 5.3, 5.4, 5.5 reveal that an exponential fit at 95% confidence interval, follows the data quite closely at short distances from the grating, but relatively poorly at large distances. However, a fit using the sum of two exponentials instead of one, and also at 95% confidence interval, provides a much better fit of the experimental data with an agreement even for large beam-grating separations. It is important to distinguish what it means, both mathematically and physically:

- Mathematically, the sum of two exponentials is equivalent to adding another exponential term in the formula for the angular energy distribution. This would suggest the possibility for the existence of a correction term in the single-electron yield, through a more sophisticated expression for the exponential.

- Physically, such a correction term would be plausible, if high order modes are also excited. In this case each mode would be defined by its own exponential term with very specific evanescent wavelength.

The possibility of a correction term to the exponential implies a correction to the description of that coupling. However, we should be careful because both the single exponential fit and the double-exponential fit, fall within experimental error bars. These plots are therefore

interesting, but do not constitute proof of the existence of higher modes, only a possible supportive evidence.

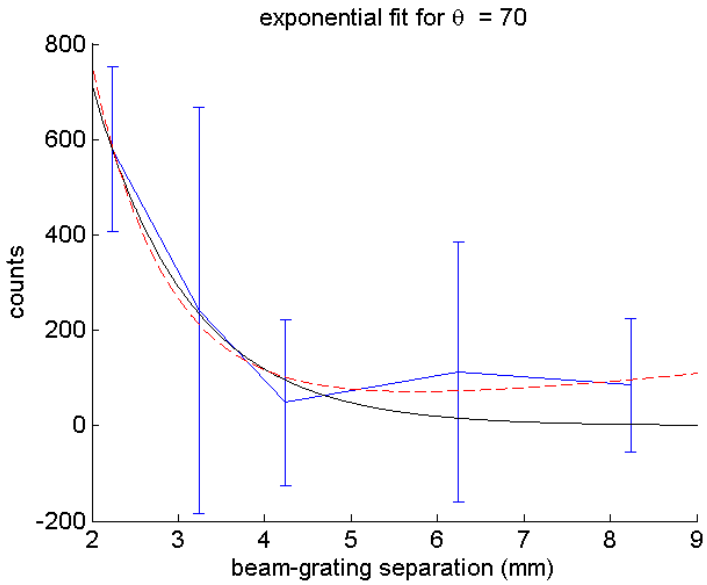

Figure 5.3: Exponential dependence at 70 deg Blue: experimental data – Black : one-exponential fit – Red: Two-exponential fits

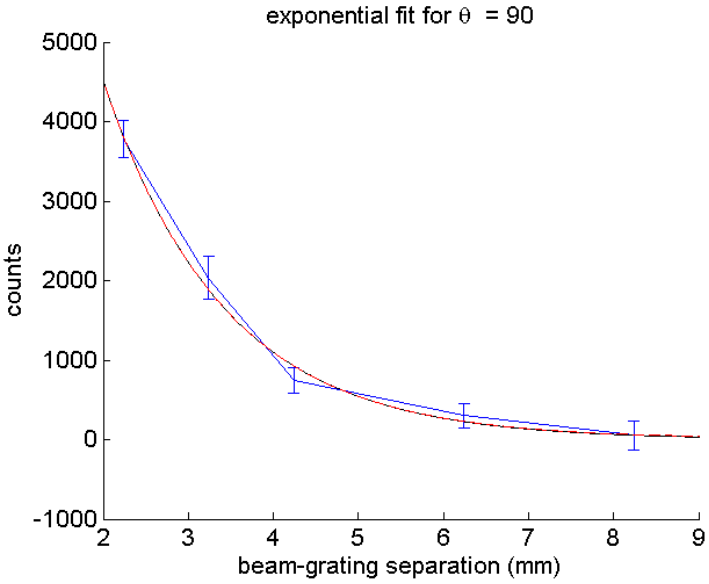

Figure 5.4: Exponential dependence at 90 deg Blue: experimental data – Black : one-exponential fit – Red: Two-exponential fits

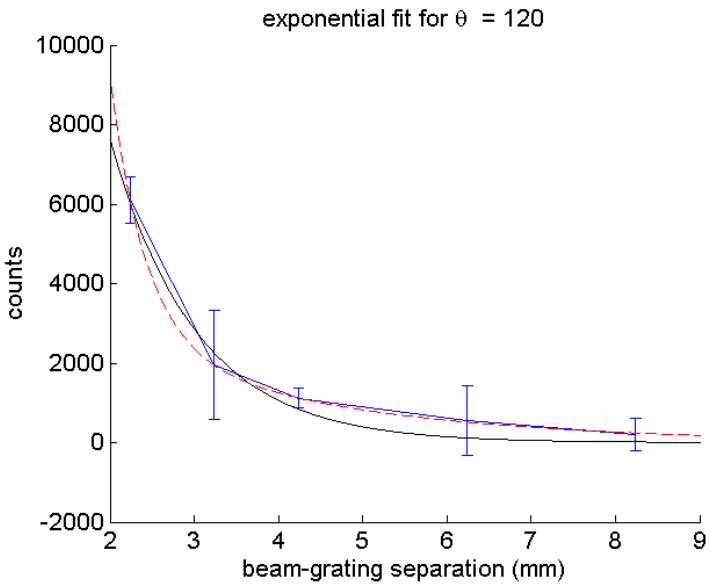

Figure 5.5: Exponential dependence at 120 deg Blue: experimental data – Black : one-exponential fit – Red: Two-exponential fits

To summarize the above considerations, it is clear that at far distances from the carousel, the Smith-Purcell signal is negligible: we have seen on the figure 5.1 that, at 6.24 and 8.24 mm, the yields from the gratings and the background are of similar order. Taking measurements at those large distances is not ideal for bunch length diagnostics purpose. However, distances cannot be arbitrarily short in order to limit the risk of interception from the top of the grating teeth with the halo of the beam. For this reason, our diagnostics from the data above, shall be based on the three closest positions: 2.24, 3.24 and 4.24 mm. This is also in line with general bunch diagnostics experiments, where short beam-grating separations are preferred.

5.1.2 Time profile reconstruction at maximum intensity

We shall start with the reconstruction at 2.24 mm separation. The results are presented in the figures 5.4 and 5.5. The figure 5.4 shows the reconstruction of the time profile, based on the full set of three gratings, as retrieved from the KK algorithm the PCI algorithm that we developed in the Chapter 3, while the figure 5.5 is more detailed, and shows also the reconstructions as obtained from each individual grating. Since it is now the first time that PCI is implemented on experimental data, it is worth to see how good it compares with KK.

A few interesting features emerge from that comparison:

- First, we can see that KK exhibit a certain oscillations, with some of them reaching negative amplitudes. Those oscillations are known to be an intrinsic signature of the KK algorithm itself, that is, they cannot be removed by increasing the meshing of the reconstruction space. They are clearly unphysical, because a negative current density does not have any physical meaning.

- Now from the PCI perspective, it is interesting to note that no unphysical negative current is present. In the case of the reconstruction using the full set of grating shown in the figure 5.4, we also see that all secondary oscillations completely disappear, and only a decaying tail of the bunch survives, apart from the main peak.

It is possible to have some further insight on the origin of these oscillations by looking at the figures 5.7 and 5.8 where the contributions from each individual grating is shown: we see that in the KK case, in figure 5.7, the 250 microns and 1500 microns period gratings generate a lot of these secondary oscillations, and they reach negative values as expected. The 500 microns grating generates a better yield. In all these three cases, the same extrapolation and interpolation method as mentioned in the chapter 3 were used: a decaying exponential at high frequencies, and Gaussian extrapolation at low frequencies. For the PCI cases displayed in the figure 5.8, things are different: it is the 500 and 1500 gratings that generate oscillations, which are also non-physical because they appear as secondary peaks. The 250 microns grating seem to generate a more realistic profile, but the comparison with the reconstruction using all gratings shows that the 250 microns yields a tail that is much larger than the actual one. From all these considerations, it is clear that it is better to use the whole set of three gratings, rather than using one of them and relaying on extrapolation

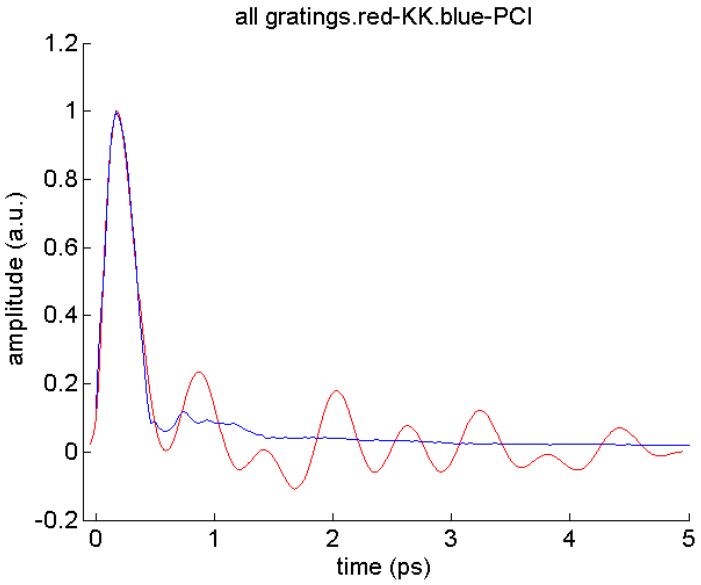

Figure 5.6: Reconstruction using all gratings. Red Line: Reconstructed profile using the Kramers-Kronig formula. Blue Line: Reconstructed profile using PCI

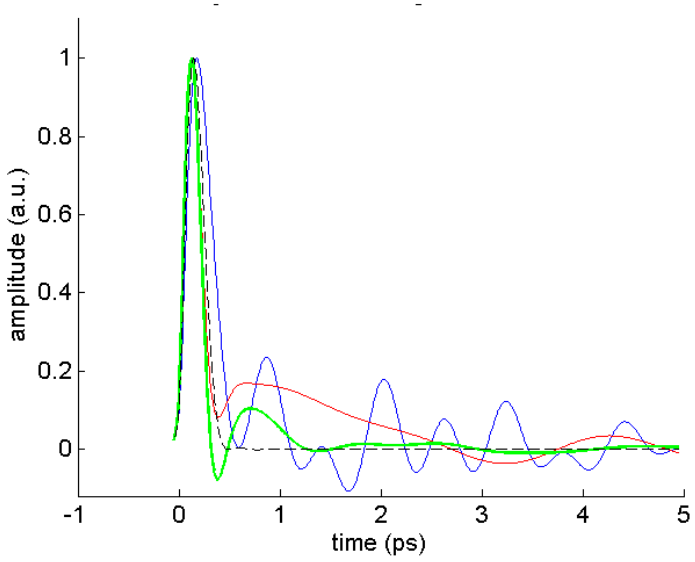

Figure 5.7: KK: Comparison of the time reconstruction from all gratings used together, vs reconstructions based on each individual grating.Blue line: Profile from the full set. Red line: profile from the 250 microns. Green line: profile from the 500 microns. Black line: profile from the 1500 microns

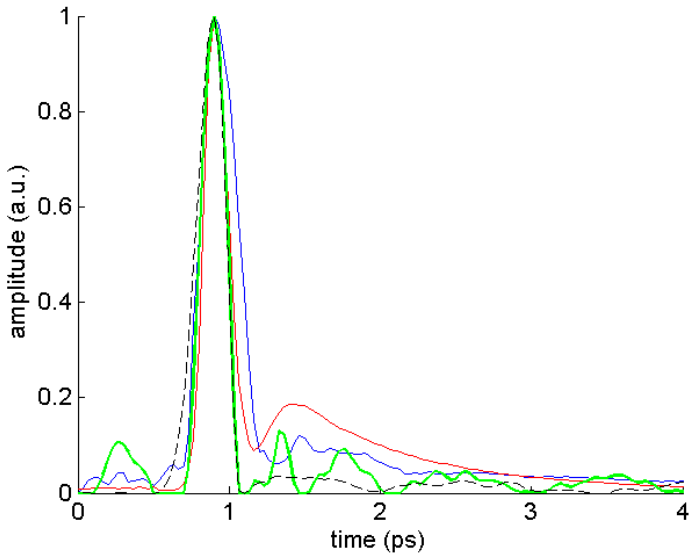

Figure 5.8: PCI: Comparison of the time reconstruction from all gratings used together, vs reconstructions based on each individual grating.Blue line: Profile from the full set. Red line: profile from the 250 microns. Green line: profile from the 500 microns. Black line: profile from the 1500 microns

After this qualitative comparison of the profiles, we can now comment on the bunch length estimations. Bunch length can be calculated using either of the two usual quantities:

– The weighted root-mean-square (weighted rms). It is given by

$$t_{rms} = \sqrt{\frac{\sum_i [t_i^2\, I_i(t)]}{\sum_i I_i(t)} - \left(\frac{\sum_i [t_i\, I_i(t)]}{\sum_i I_i(t)}\right)^2} \tag{5.1}$$

Because the summation index i spans the whole of the time domain used for reconstruction, all points reconstructed profile will be accounted for. This includes any unphysical bumps or oscillations, and even very small amplitudes at large t's.

– Another widely used quantity is the full-width at half-maximum (fwhm). It does not render profile tails very well. However, it has the major advantage of being normalization-independent, and for this reason, it is the quantity of choice at SLAC, and is used whenever results need to be compared.

Table 5.2: Comparisons of the calculated bunch length in fs at maximum intensity position

grating	KK fwhm (main peak)	KK weighted rms	PCI fwhm (main peak)	PCI weighted rms
250 alone	180	415.4	180	349.4
500 alone	171	153	193	158.8
1500 alone	200	79.9	230	84.7
complete set	270	614.7	290	153.6

The table 5.2 summarize the estimated bunch length for each grating individualy, for the whole set of three grating taken together, both in the case of PCI and KK. The results of calculation are shown as weighted rms-values as well as fwhm. Several interesting features can be commented on in that table:

1. The weighted rms-value for the whole set of gratings is more than four times larger through KK (614 fs) rather than PCI (153 fs). This can be understood by looking at the figure 5.6: we see that the KK reconstruction exhibits numerous oscillations that all contributes as additional terms in the weighted-rms summation.

2. If we now do the same comparison, that is, the reconstruction from the whole set of gratings through KK and PCI, but this time through the measurement of fwhm rather than the weighted rms, we see that the estimated bunch length is essentially the same (270 fs for KK rather than 290 fs for PCI). Since the fwhm only takes into account the main peak, the information on any secondary oscillation are outright discarded as unphysical. This is legitimate because the number of bunches can be calculated from the repetition rate, known at the time of the experiment.

3. As a general rule, and for the cases that concern us, we see that fwhm estimations are relatively close both for PCI and KK, whether we consider a single grating or the whole set (200 fs fwhm for the 1500 microns grating for KK, and 230 fs through PCI). The reason why the PCI estimations of the fwhm are very slightly larger, is because all the additional KK oscillations are gradually flattened through the PCI iterations, leading

to a very slight enlargement of the main peak. For some reconstructions however, such as the 250 microns grating, both the KK and PCI estimation of the fwhm are the same (180 fs). To understand why, we can compare the KK reconstruction of the 250 microns in the figure 5.5(a) with the PCI reconstruction of the 250 in the figure 5.5(b) , we see that the KK version exhibits just one large tail of which only a small portion goes to negative values, so most of the profile is actually unaffected by PCI.

As a result, it is legitimate to conclude that the bunches from which all these profiles have been retrieved, do not have Blaschke phase and are single Gaussians. This also means that, if we see disagreement in bunch length estimation when compared with other experiments, the cause will probably not be of algorithmic nature.

5.1.3 Beam-grating dependence of the reconstructions

The longitudinal bunch length is independent of any beam-grating separation and as such, the same profile should normally be retrieved, no matter how far it is located from the grating surface. In practice, as I showed in the figure 5.1, the strength of the signal varies with distance, and this affects the quality of the reconstruction.

The figure 5.9 illustrates this on the time profile reconstruction at three different distances, where the radiation from all gratings has been used. It is remarkable to see how the main peak is independent from the beam-grating separation at 2.24 and 3.24 mm. At the distance of 4.24 mm, the signal strength is much weaker (as we have seen in the figure 5.1) and because of the detectors sensitivity, the high frequencies signals are not correctly detected. This partly corrupts the signal reconstruction. As we can see from the figure 5.9, the main outline of the profile at 4.24 mm and its envelope (defined by low frequency signal) can still be guessed. This is the reason why, in practice, Smith-Purcell measurements for diagnostics purpose are often made within the region ranging from 1 to 4 mm from the grating.

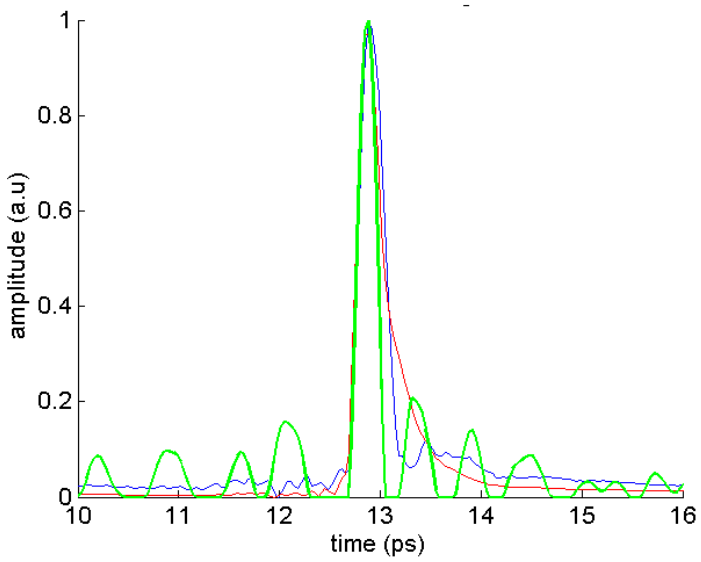

Figure 5.9: Profile reconstruction at several beam-grating separation. Blue line: 2.24 mm – Red line: 3.24 mm – Green line 4.24 mm

5.1.4 Reconstruction for various bunch compressions

The previous profiles reconstructed were mostly typical Gaussians. But during this PhD, the E203 experiment not only covered study of signal against beam-grating separation, but also the reconstruction of profiles for various bunch compressions. High compression bunches have been produced in 2012 and 2013 and are shown in the figure 5.10, while intermediate compression ones have been produced in 2013 and is shown in the figure 5.11. I shall first discuss the results only qualitatively, and the numerical discussion will follow in the next section, when comparing with other experiments.

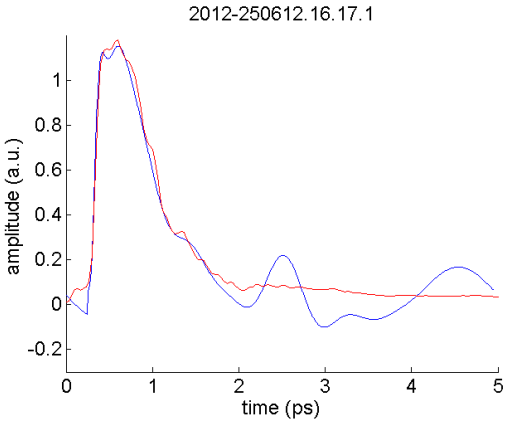

(a)

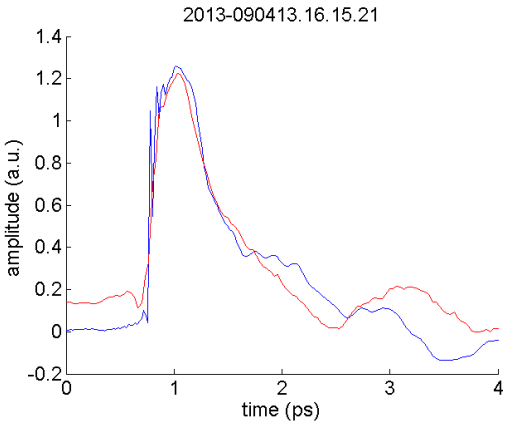

(b)

Figure 5.10: Profile reconstruction at high compression (a) in June 2012 (b) in April 2013 Red line: PCI reconstruction – Blue Line: KK reconstruction

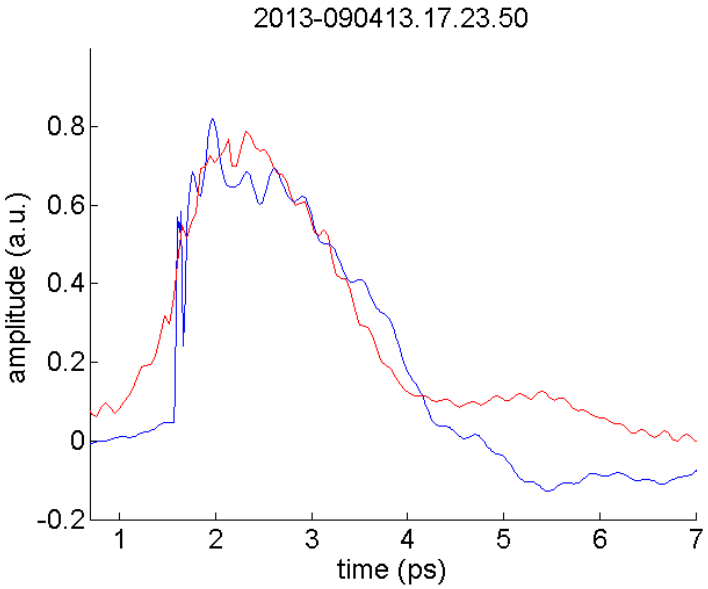

Figure 5.11: Profile reconstruction at intermediate compression in April 2013 Red line: PCI reconstruction – Blue Line: KK reconstruction

The high compression retrievals in the figure 5.10 show that the use of PCI does not bring any significant change to the time profile, that is, there is no Blaschke phase. The same situation holds for the intermediate compression profile retrieved in the figure 5.8. The only difference for the intermediate compression case is that PCI displays a much smoother rise than the abrupt start of the KK profile plot.

5.1.5 Spectrum

It is interesting to see how the experimental spectrum compared to the simulations of the chapter 2. This is shown on the figures 5.12, 5.13 and 5.14, where the values are displayed for the 11 detectors. We see that the E203 data are generally consistent with the theoretical predictions both from the particle-in-cell and the surface-current theory. There is however a noticeable behaviour for the 250 microns grating where the experimental spectrum matches the particle-in-cell simulation quite well, while the surface-current theory behaves differently between 1.8 and 3 THz, with a very poor yield predicted.

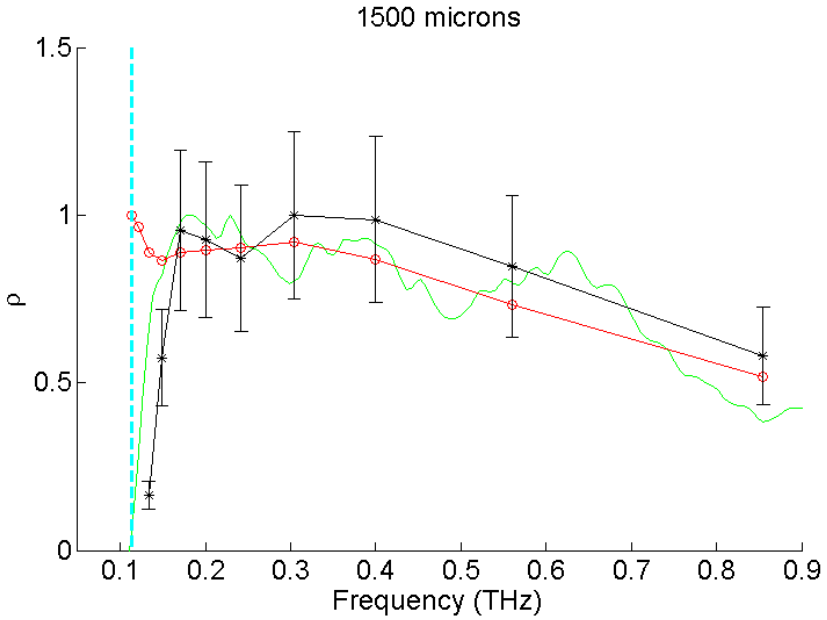

Figure 5.12: Comparison of the experimental spectrum with the far-field and near-field ones for the 1500 microns Black line: E203 experimental spectrum – Green: Near-field from particle-in-cell – Red line: SC Theory

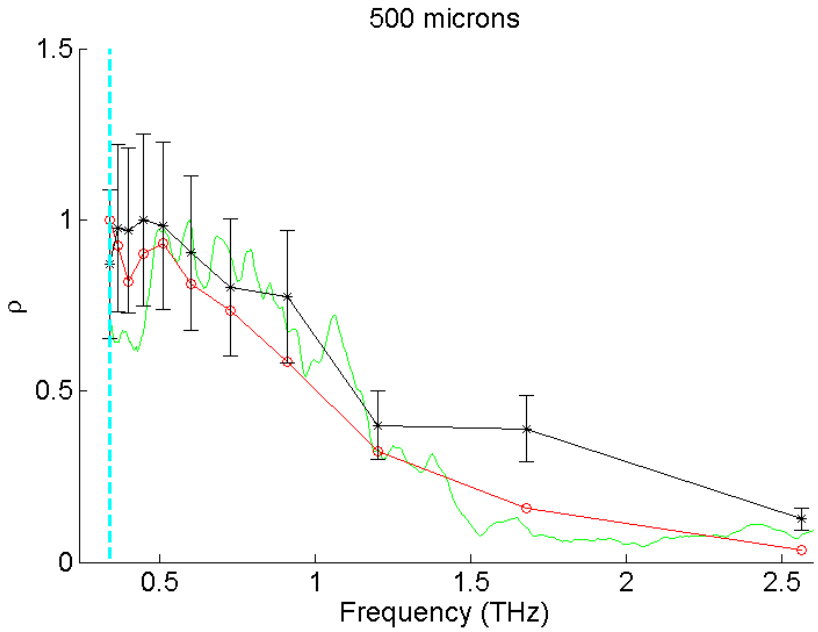

Figure 5.13: Comparison of the experimental spectrum with the far-field and near-field ones for the 500 microns Black line: E203 experimental spectrum – Green: Near-field from particle-in-cell – Red line: SC Theory

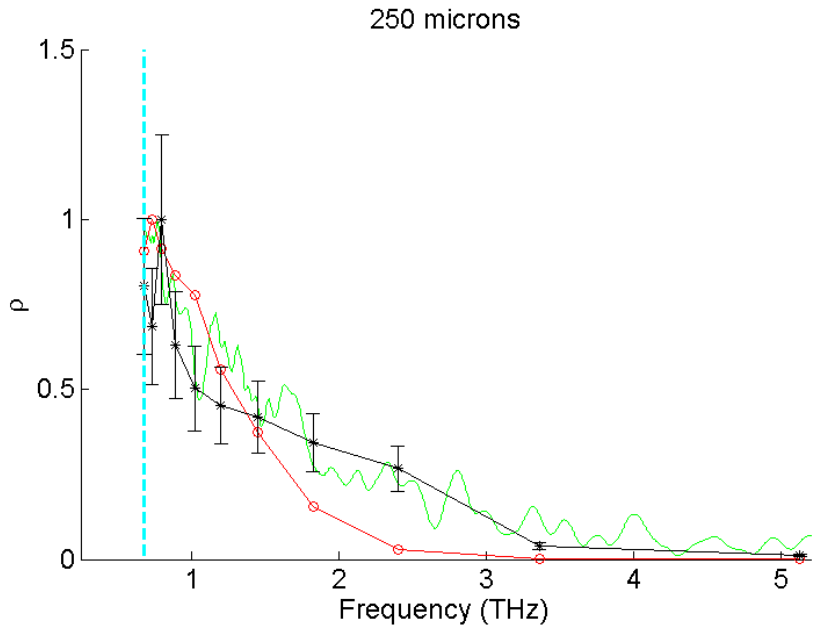

Figure 5.14: Comparison of the experimental spectrum with the far-field and near-field ones for the 250 microns Black line: E203 experimental spectrum – Green: Near-field from particle-in-cell – Red line: SC Theory

5.2 Azimuthal study

5.2.1 Introduction

The azimuthal study has been carried on the 16th of May 2015 at SLAC. The purpose was to investigate the structure of the Smith-Purcell signal at ϕ different from zero and at various beam grating separations. Unlike in the $\phi = 0$ case, the aim here is not to reconstruct profiles, but rather to explore experimentally the properties of the coherent Smith Purcell radiation and compare it with theoretical predictions based on surface current theory. As we have seen in the Chapter 2, the surface-current theory makes predictions of the transverse structure of the Smith-Purcell radiation, and the amount of radiated energy. To our best knowledge these have never been checked carefully against experiment so far. The measurements were conducted at 2.24 mm, 3.24 mm, 4.24 mm, 6.24 mm and 8.24 mm to explore how far a possible signal could be detected. A 15 mm x 4mm slit was used for this directionality study and was located at 155 mm above the grating. This study will be limited to the 2.24 mm and 3.24 mm beam-grating separation cases, for the following reasons:

- In the previous section 5.1 on bunch profile recovery, it has been shown that, for many frequencies, the subtracted signal radiated from grating was very close to noise level at 6.24 mm and 8.24 mm. On this first ground, we had then focused on the three closest distances from grating.

- There is an additional problem with the azimuthal scan at 4.24 mm : due to time constraints, the resolution of the measurements were half of those carried at 2.24 mm and 3.24 mm. At 2.24 and 3.24 mm, the ϕ scan was performed by moving the slit from -10 mm to $+10$ mm in the ϕ direction, by steps of 0.5 mm: the angular ϕ step used in this analysis is thus 0.1848^o . At 4.24 mm however, we moved by steps of 1 mm, and have thus only half the number of measurements made at the two other distances. As a result, it is difficult to make conclusions at 4.24 mm. This is illustrated in the figure 5.15, where the subtracted yield is shown for these three distances, in the case of the 250 microns-period grating. As it can be seen, a clear and visible structure appears

for the two closest distances 2.24 and 3.24 mm. At 4.24 mm however, the structure looks much more blurry, and it could potentially be either because of the beam-grating separation is too large, or because the span of measurements in the (θ, ϕ) plane has only half the measurements taken, compared to the two other distances. For this reason, the azimuthal data at 4.24 mm are not conclusive and we will focus on the 2.24 mm and 3.24 mm cases.

5.2.2 Distribution of the energy

The distribution of energy is presented in the figures 5.13, 5.14 and 5.15 for the 250, 500 and 1500 microns period gratings respectively. For each of them, the data at 2.24 and 3.24 mm of beam-grating separation is shown. Each starred blue line represents the signal for a particular θ .

A few interesting features emerge from these figures:

First, the azimuthal range spanned from each side of the zero are not equal. This shows that the detector was not located exactly at the middle above the grating.

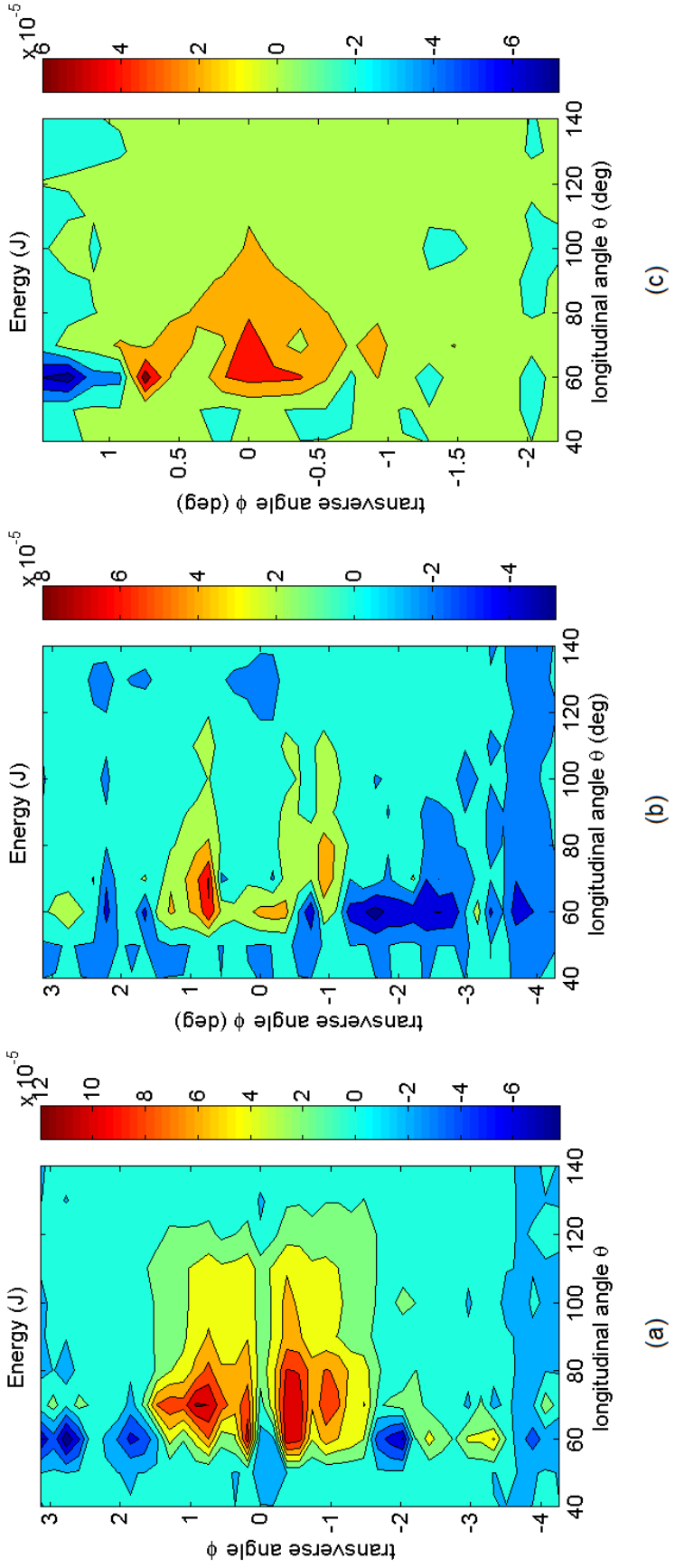

Figure 5.15: Subtracted Smith-Purcell signals for the 250 microns grating for the following beam-grating separation (a) 2.24 mm(b) 3.24 mm (c) 4.24 mm.

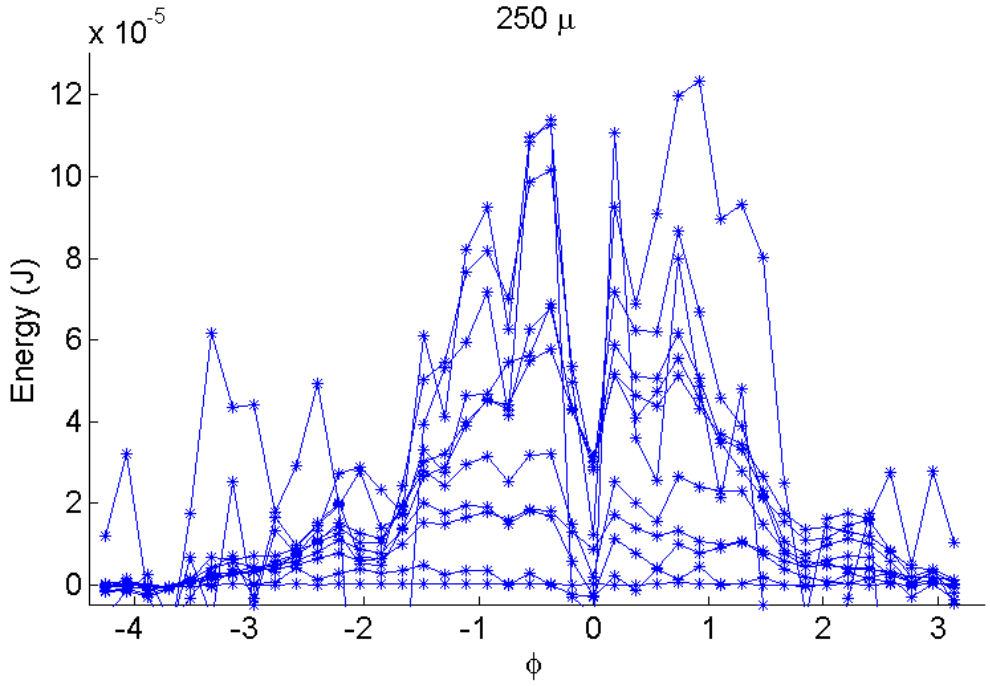

(a)

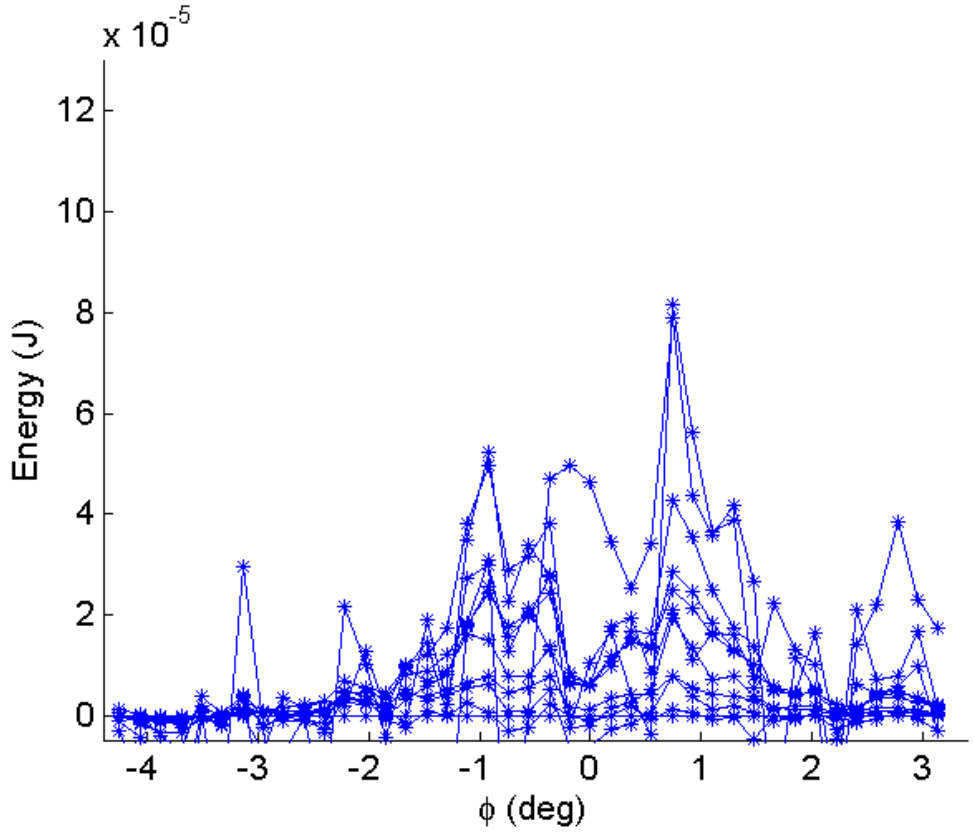

(b)

Figure 5.16: The dependencies of the signal energy on the azimuthal angle for the 250 microns at (a) 2.24 mm and (b) 3.24 mm. Each blue line describes the dependence for a given $\theta \in [40^o, 140^o]$ per step of 10^o.

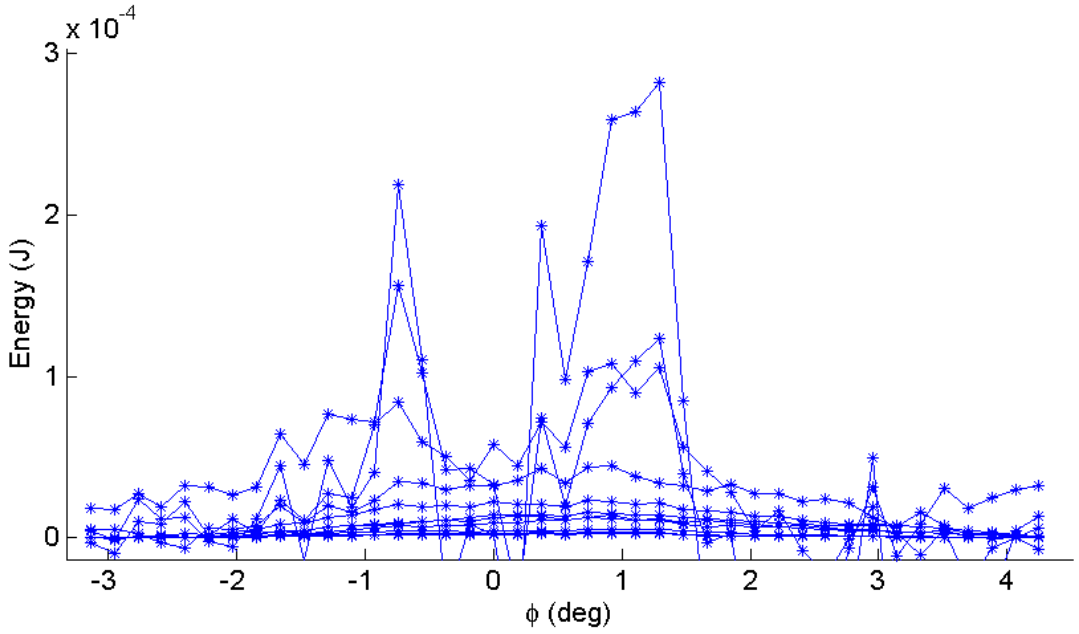

(a)

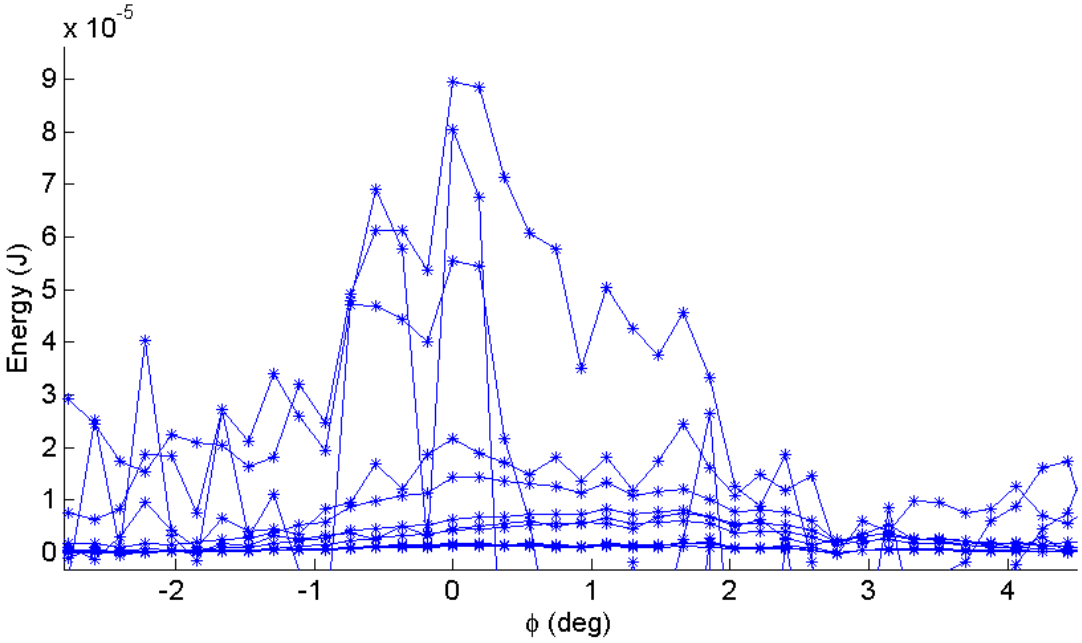

(b)

Figure 5.17: The dependencies of the signal energy on the azimuthal angle for the 500 microns at (a) 2.24 mm and (b) 3.24 mm. Each blue line describes the dependence for a given $\theta \in [40^o, 140^o]$ per step of 10^o.

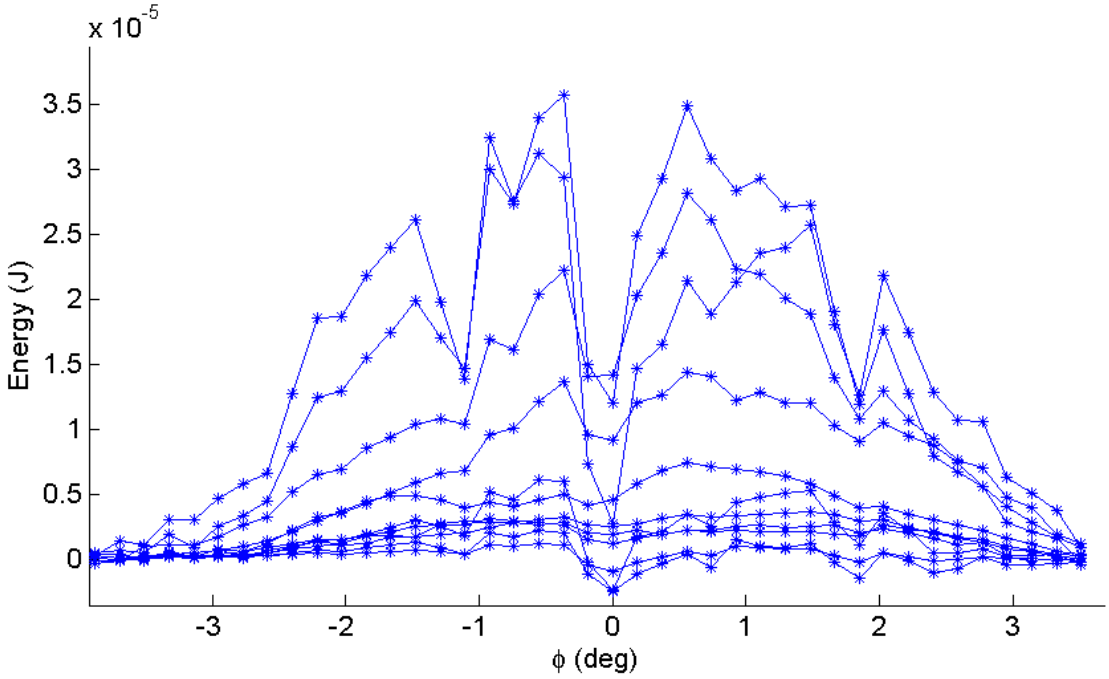

(a)

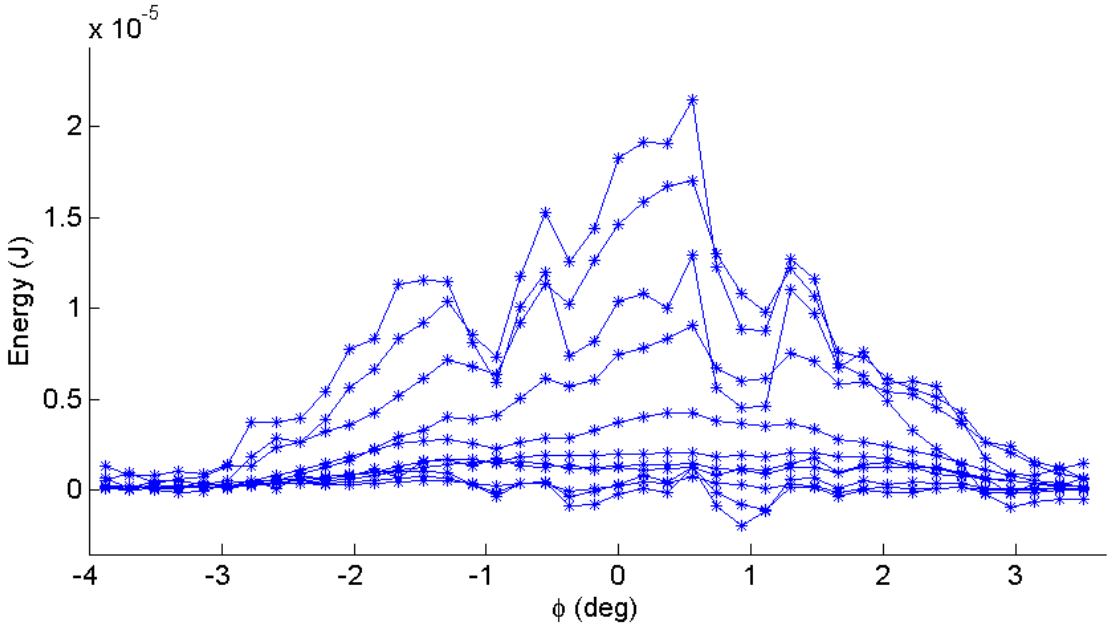

(b)

Figure 5.18: The dependencies of the signal energy on the azimuthal angle for the 1500 microns at (a) 2.24 mm and (b) 3.24 mm. Each blue line describes the dependence for a given $\theta \in [40^o, 140^o]$ per step of 10^o.

Secondly, At 2.24 and 3.24 mm there is a phenomena which is remarkably consistent across the three gratings: at 2.24 mm, a double-peaked structure distinctly appears in the data, as shown in all the insets a of the figures 5.16, 5.17, 5.18. All these plots exhibits a valley

of local minimum at $\phi = 0$ that take place for all frequencies. At 3.24 mm of beam-grating separation, the structure is different and differs from grating to grating: the 250 microns grating has minimum at $\phi = 0$ and two larger peaks at $\phi = 1$ and $\phi = -1$, the 500 microns grating has a large central peak for some frequencies but otherwise has an unclear structure. The 1500 microns grating has however a very clear and precise shape: a central peak with two local minima at -1 and +1 increasing into two larger peaks at +1.5 and -1.5. As explained above, we limit ourselves to the behaviour of the azimuthal Smith-Purcell signal at the two smallest distances. However, even the behaviour at 8.24 mm shows us something interesting. The figure 5.19 shows a view-from-the top of the subtracted raw data (that is, the ADC counts received by the DAQ) for the 1500 microns grating. We see that at $\theta = 100^o$, the plot has fluctuating non-zero values that do not appear elsewhere. This feature is not physical, and is due to the fact that the detector is damaged, and his responsivity is subject to very large error generated by a corrupted repeatability. This explains why all the error bars on the measurements are extremely large compared to others.

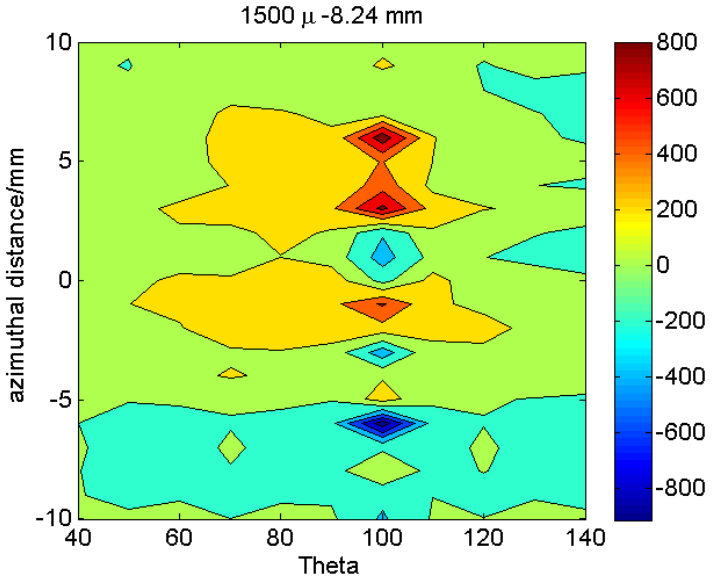

Figure 5.19: Effect of the damaged detector at 100^o on the counts readings, for the 1500 grating. The large errors cause nothing but statistical fluctuations

Our next objective now is to see if the geometrical structure that are observed, can be explained in the context of surface-current theory as predicted from simulations. This will be the topic of the following section.

5.2.3 Comparison with the predictions of the surface-current theory

In the Chapter 2, we had examined the behaviour of the Smith-Purcell radiation in the angular transverse direction ϕ . We can now use these previously obtained results and compare them with the outcome of the experiment. The parameters used as input for the simulation are of two types:

1. The experimental parameters given prior to data taking: the beam charge, the beam energy, the transverse dimensions, and the normalized emittance.

2. The electron bunch length calculated after the processing of the experimental data collected at $\phi = 0$.

Despite the fact that we are going to use theoretical predictions, the surface-current information to be used is not just a transpose of the Chapter 2, but takes into account here the acceptance of the slit placed before the detector, which is 4 mm wide. We will now have a closer look to some of the blue lines from the figures 5.16, 5.17 and 5.18 mentioned previously. We have seen that the behaviour at 2.24 and 3.24 mm are quite different and these two cases need therefore to be treated separately.

In the figure 5.20, selected data for the net (subtracted) radiated energy from the 1500 microns grating at 2.24 mm is shown. The error bars of the experimental data are the statistical errors that originate from the distribution of the raw counts. In order to compare with the surface-current theory as accurately as possible, we have taken into account the responsivity of the pyrodetector as stated in the datasheet: typically it varies from 0.8 to 1.6 of the measured signal. The area consistent with the experimental signal is located between the two curves describing the minimum responsivity and maximum one. We see that for many angles, the predicted result from the surface-current theory lies between the two extremal experimental curves. We can make a few interesting remarks regarding the fine structure. First, at all θ angles, we observe a drop of signal at a local minimum in

$\phi = 0$. This local minimum appears also in the surface-current model at all θ, but having smaller amplitude. For example, if we look at the simulation for 1500 microns grating at $\theta = 140^o$, or $\theta = 110^o$, the dependencies look essentially flat with variation from maximum to minimum of only 1% of the plot's amplitude. As compared with the experimental data, and only zooming over the energy-range values of interest, in the figure 5.23, reveals that both have a minimum at $\phi = 0$.

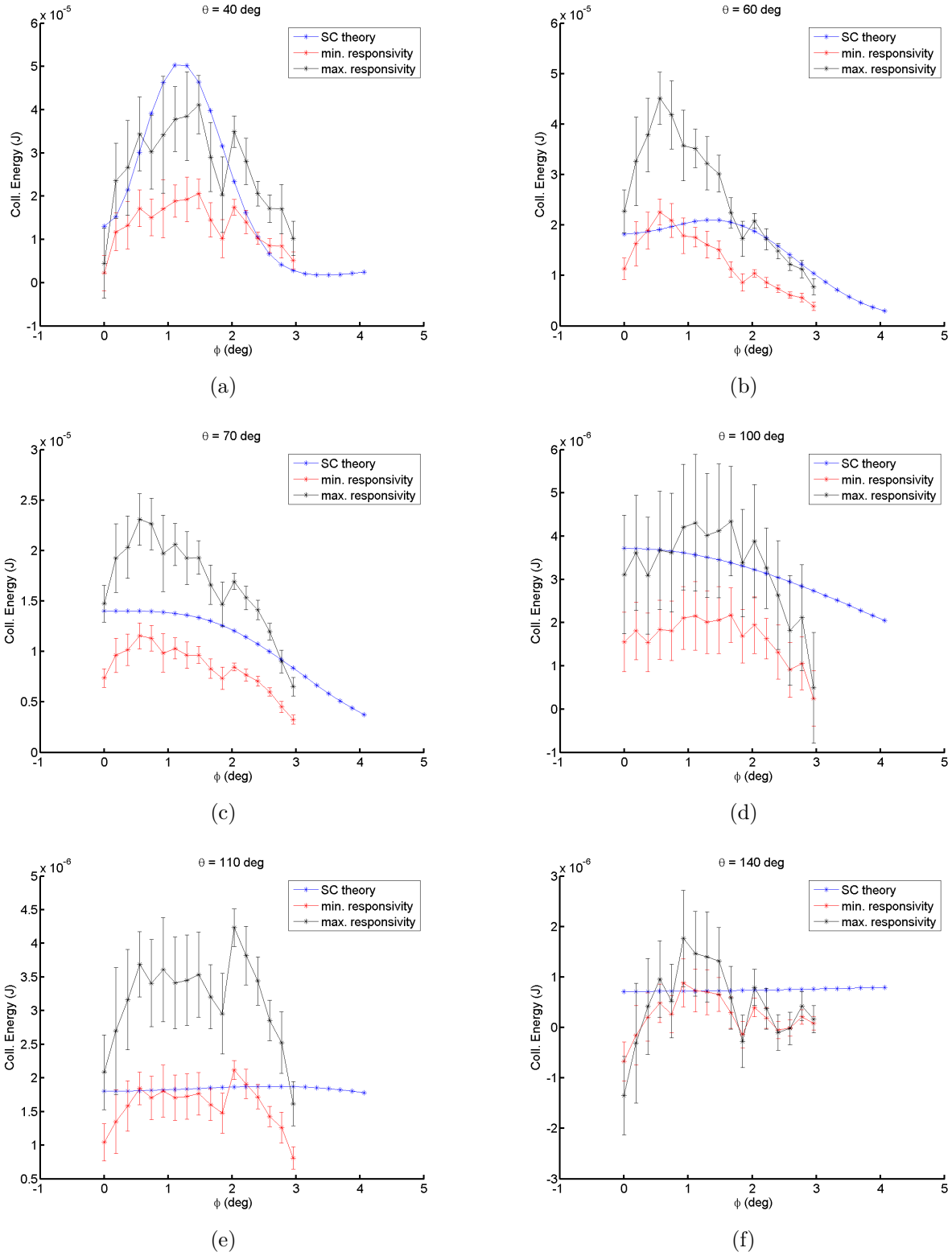

Figure 5.20: Comparison of the azimuthal energy collected at the detector with the predictions of the surface current theory for the 1500 um grating

Conversely, some other type of fine structures that are predicted by the theory, are not necessarily well revealed in the experimental data: at $\theta = 40^o$ for example, the experimental data does not show any real peak of the signal, while the surface-current model predicts a peak located at 1.23^o . This could be attributed to finite angular resolution of the system and thus smearing the fine structures of the peaks.

In general, the ϕ signal predicted by the theory extends further than what is observed. All experimental data show a rapid drop of signal between $2^o and 3^o$, while the theoretical values decrease with a lower slope, and hence extend further. This data can be especially valid to design next generation truly single shot Smith-Purcell monitors.

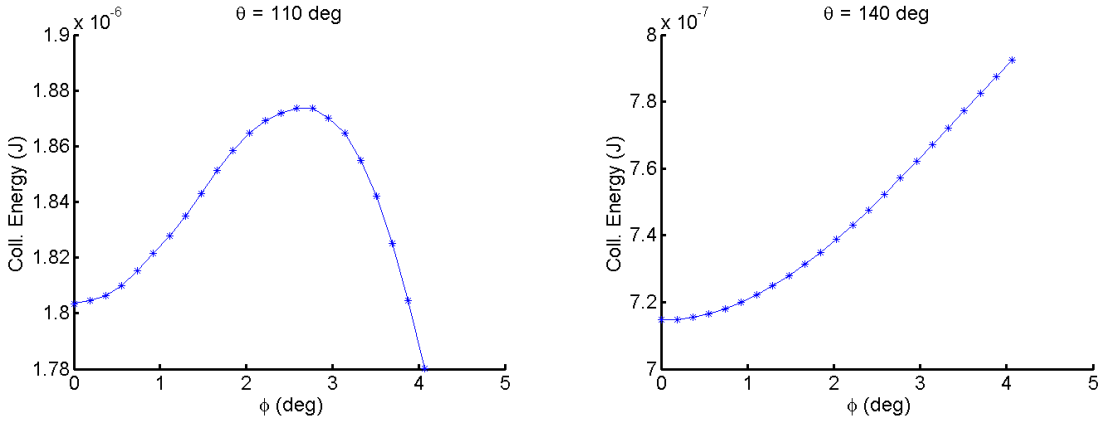

(a) (b)

Figure 5.21: A closer look of the 110^o and 140^o simulations: both reveals a local minimum at $\phi = 0$

If we now make a similar comparison for the 500 microns grating, we see that the outcome is less satisfying for some angles. The figure 5.22 presents the results for the same θ angles than in the previous case. We see a few things:

- At small θ angles, the simulation is usually within the range of the experimental data, that is, modulo the uncertainties.

- At large θ angles however, the simulation does not match the experimental data, whether we take into account the statistical standard deviation, or the systematic uncertainty that comes from the responsivity detector. In the examples I show here:

at 100^o , 110^o , or 140^o , the predicted energy is higher than the maximum values compatible with our measurements.

– At some angles, such as 40^o and 60^o , the simulation seems almost flat, but again, a dedicated plot such as shown in the figure 5.22, shows that the surface-current theory predict the existence of a structure. However, the uncertainties and details of those predictions, are clearly not within what could be seen by our monitor.

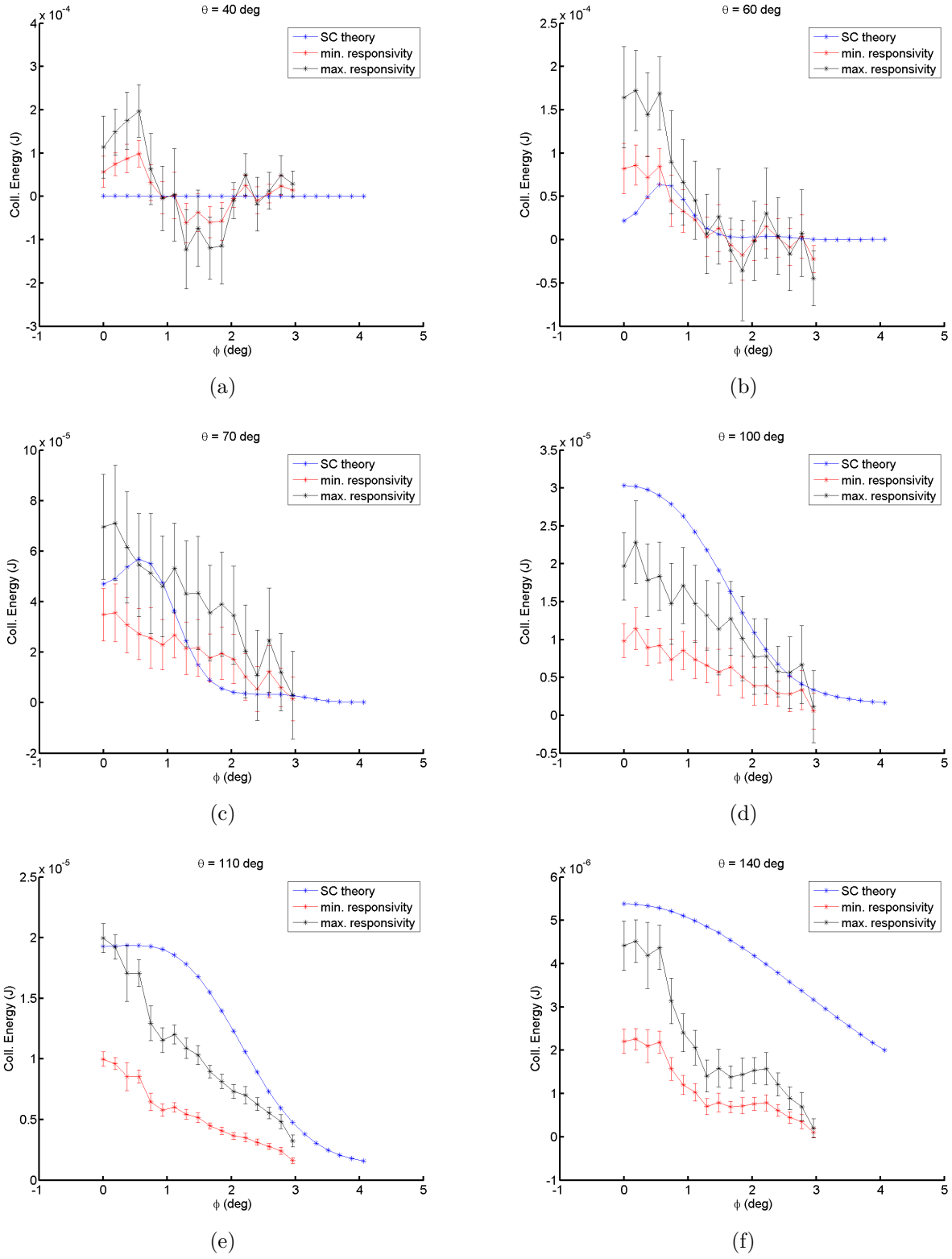

Figure 5.22: Comparison of the azimuthal energy collected at the detector with the predictions of the surface current theory for the 500 um grating

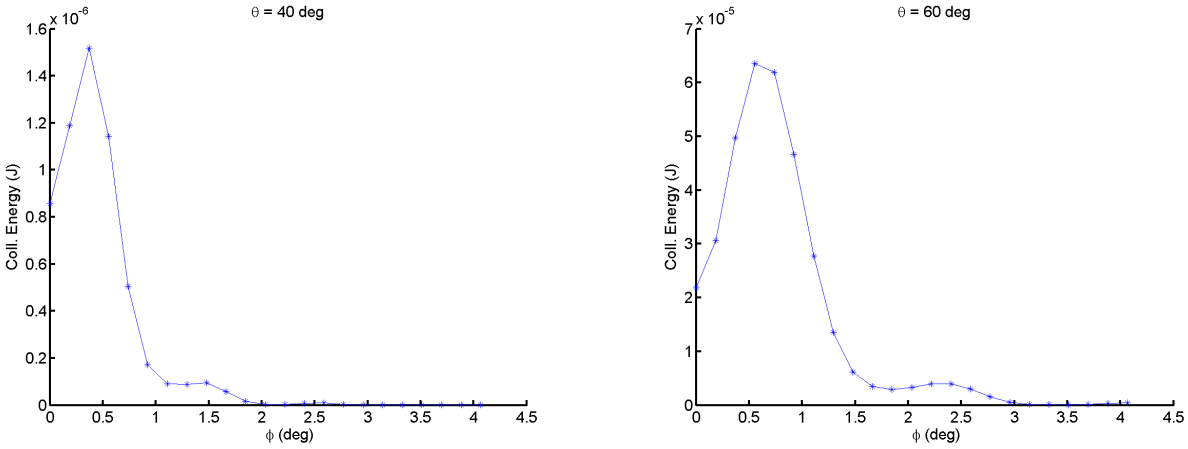

(a) (b)

Figure 5.23: A closer look of the 40^o and 60^o simulations for the 500 um: both reveals a local minimum at $\phi = 0$ and the structure is not flat

To understand what could be the origin of such discrepancy while the agreement was so good with the 1500 grating (and, as I shall show later, with the 250 grating too), the figure 5.17 is helpful: the asymmetry between the peaks at positive ϕ and negative ϕ suggests that the 500 microns grating placed on the carrousel might not have been exactly parallel to the beam. Such possibility is supported by the pattern we see in the inset *b* of figure 5.17 , where the large amplitude curves that peaks near 10^{-5} J, are centered around $\phi = 0$, while the low-peaked curve below 2.10^{-5} J seem to be peaked around $\phi = 1deg$. This could only happen if the grating has a yaw angle with respect to the beam direction.

Regarding the 250 microns grating, generally speaking, the data agree quite well with the simulations. The results are presented in the figure 5.24 , with the figure 5.25 being a zoom on some simulation cases to show that the signal is not flat nor constant. For the 250 grating, in most cases, the simulations are closer to the lower curve as expected as detector sensitivity and responsivity drop with increase of the signal frequency.

It is interesting to note that for almost all angles considered, the simulation predict a quicker drop of signal with phi, than observed (apart for $\theta = 140^o$). In the specific case of the 250 um grating the simulation shows a pattern: as θ increases, the phi signal extends further. In the figure 5.24, we see how the signal reaches noise-level at just $\phi = 1^o$ when $\theta = 40^o$, at $\phi = 1.5^o$ for $\theta = 60^o$ and at $\phi = 2^o$ when $\theta = 80^o$ respectively, and so on. The regularity of

this behaviour might suggest a suitable way to improve the transversal modelling of cSPR in the context of the surface-current theory.

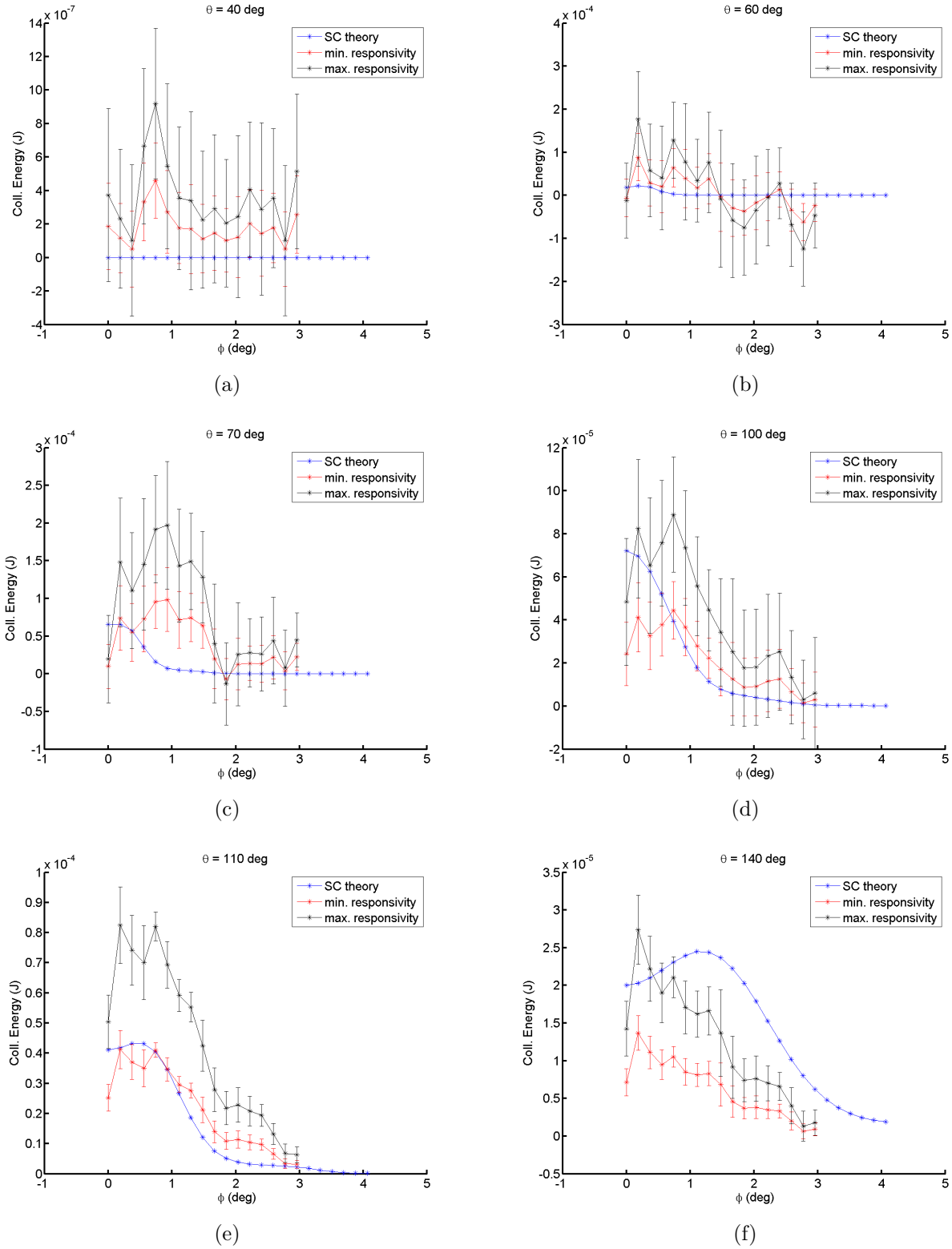

Figure 5.24: Comparison of the azimuthal energy collected at the detector with the predictions of the surface current theory for the 250 um grating

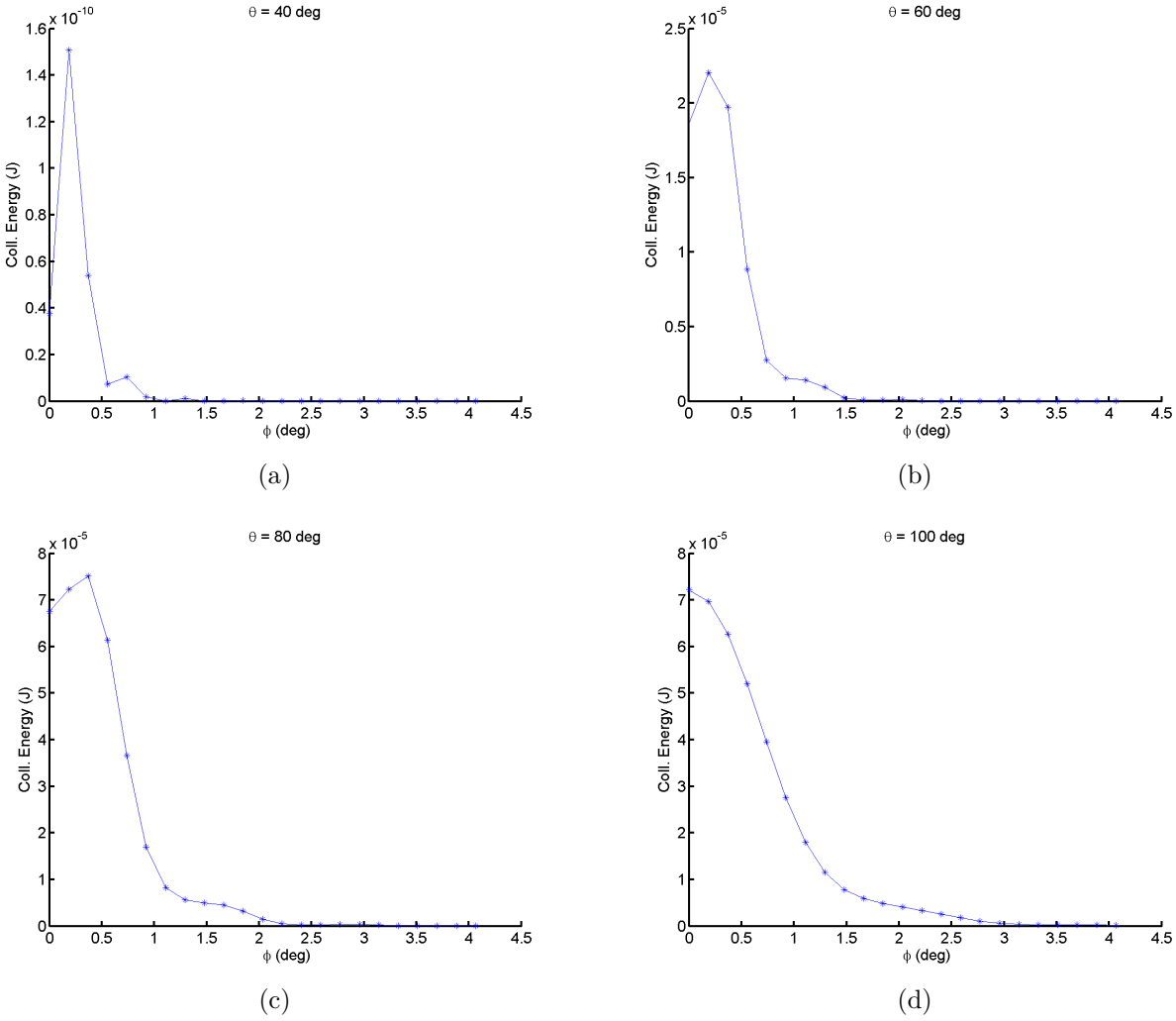

Figure 5.25: A closer look of some simulation patterns for the 250 um grating at 2.24 mm

At 3.24 mm, the observed azimuthal distribution from the 1500 um grating exhibits a more pronounced discrepancy with the simulation. The fact that the predicted order of magnitude is fully compatible with the experiment shows that the surface-current theory is sensible. The main problem comes more from the inability of the surface current theory to predict the fine structure observed from the radiation, as we shall see. With respect to the comparison we performed at 2.24 mm, the more striking difference is probably that that experimental data do not seem to reveal a just double peak structure like before. This is particularly visible in the figure 5.26: at 3.24 mm of beam-grating separation, the signal seems to have a "three-peaked structure" instead of a two-peaked one. This might be another supportive evidence of the existence of higher harmonics, which would be consistent with the exponential

fits discussed in the section 5.1 .

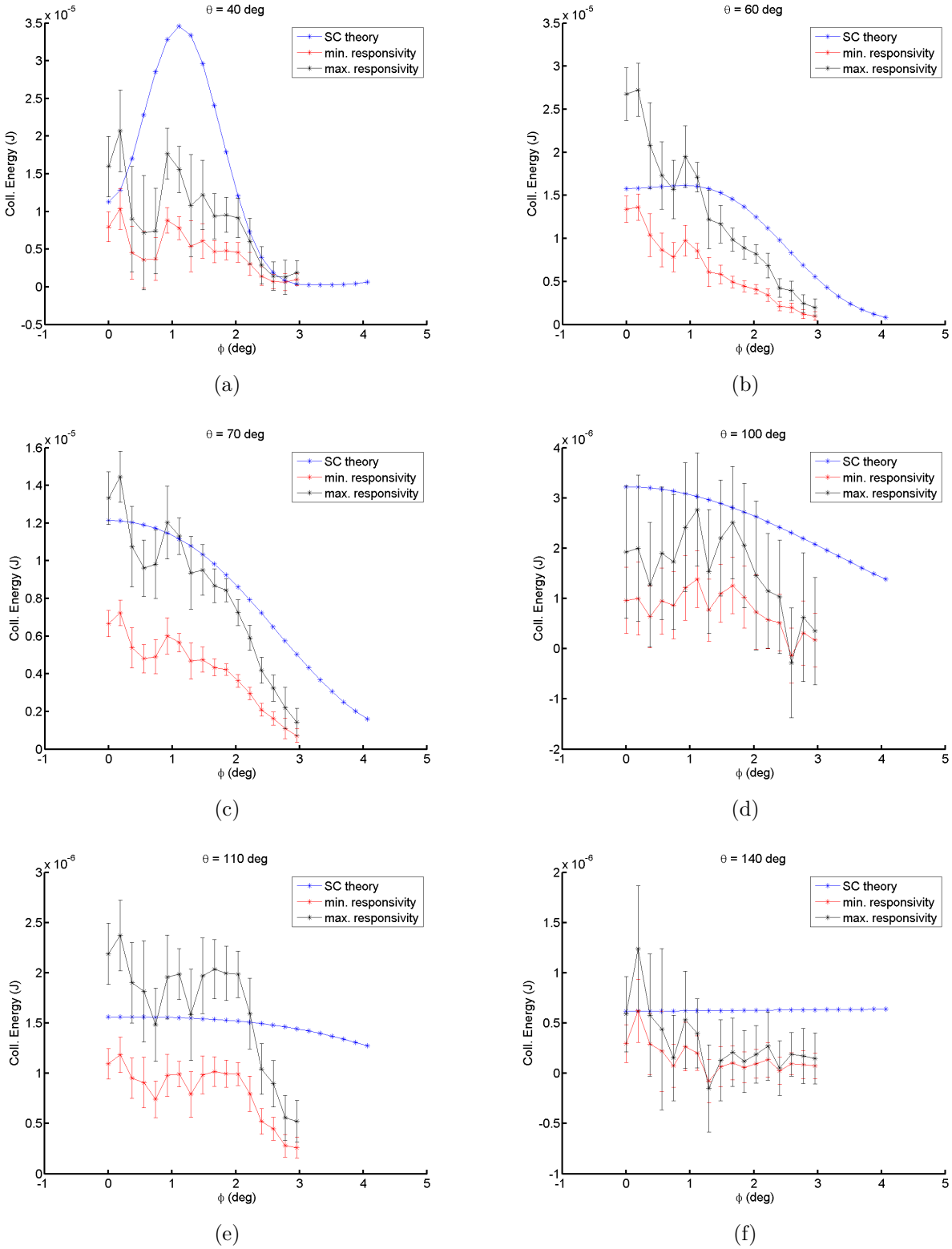

Figure 5.26: Comparison of the azimuthal energy collected at the detector with the predictions of the surface current theory for the 1500 um grating at 3.24 mm

5.2.4 Conclusion of the azimuthal study

In this section , we have shown that the surface-current is very successful in predicting the right order of radiated Smith-Purcell signal with an accuracy of less than order of magnitude. This is definitely an achievement that must be emphasized. We have seen that in general at 2.24 mm of beam-grating separation, the model was also able to predict the correct distribution of energy. It is at the larger distance from the grating that the surface-current model does not really reflect the fine structure we observe very clearly from certain gratings, as shown in the 1500 microns case has been analysed in detail.

5.3 Polarization

5.3.1 Principle of the experiment

In the polarization study, carried in May 2015 just after the directionality experiments, we analysed the coherent Smith-Purcell radiation measured at specific θ angles, for $\phi = 0$. The polarizer plate is used as EM beam splitter beam and has a 45^o inclination toward the beam. One of the polarization components is transmitted through and continues its way to the Winston cone and the pyrodetector (called "T" component where T stands for Transmission) while the second polarization component is reflected at right angle ("R" component for Reflection). A first partial study of polarisation had been carried in June 2012 and published in [21]. There were however a few differences between the 2012 and 2015 study:

1. In the studies carried out in 2012, filters were not used, and therefore the signal was contaminated with background radiation. Because some of the detectors were not located in the far field (especially the longer wavelengths) , a correct removal of background radiation would have required both the use of the subtraction of background radiation observed from the blank, and use of the filters to remove additional signal not fully dispersed by grating. The fact that no filter was used in 2012, gives to those

obtained results only a qualitative quality limiting its quantitative reliability, however the results obtained in 2012 were informative enough to allow us to move forward and design the experimental set up discussed in this chapter. In the current study, the experimental set-up made full use of filters giving us more reliable quantitative information.

2. Another difference between this and the last experiment is that, in 2012, the same detectors were used to measure both polarisations. This was achieved by positioning polarisers instead of filters inside the filter ladder which was moved vertically to measure polarisations, allowing the measurement of polarization components, without changing the detector. The fact that the same detector was used, improved reliability of the measurements as detectors were not polarisation sensitive with relative type of measurements (which polarisation measurements are), and this limited the impact of the problems related to the detector calibration. In the experiment of May 2015, the set-up was different and two polarisation components were sent to different detectors. Despite the fact that the detector calibration was not well known, we estimated that the gain of reliability from using filters, was still beneficial and contributed to a significant improvement of the experiment.

The presentation of the polarization measurements will be organized as follow: I start with an overview of the technical peculiarities and challenges of the experimental set-up and then I will discuss the measurements carried out at $\theta = 90^o$ i.e. just above the grating, illustrating in detail how the analysis was carried out. These results are by no means a complete study, and should be considered more as a contribution to the understanding of cSPR polarization properties complementing the experimental data from the 2012 run, and as a step toward further polarization studies in the context of a single-shot temporal profile monitor.

The first step of the studies is to measure the degree of the radiation polarisation from the grating and the blank. To do so both polarisation components should be measured and the results are shown in the figure 5.27 below. The first measurements were conducted with largest period grating i.e. 1500 microns. It is clear that the radiation signals from the grating

are significantly higher than the signals from the blank. We also see that the measurements of T and R polarisation from the background radiation are not negligible, and remain of same order across the various beam-grating separations. This suggests two conclusion: 1/ the degree of polarization of the background radiation is low; 2/ the background comes mainly from accelerator environment rather than from diffraction radiation (which is expected to be partially polarised). This is confirmed by the figure 5.25, which shows the degree of polarization of the background radiation. The closest beam-grating separation was 770 microns, and at that distance, the degree of polarization of the background was just 7.35%, and then decreases so rapidly with distance, that the uncertainties become compatible with a zero-values from the third data point, at 1.77 microns of beam-grating separation.

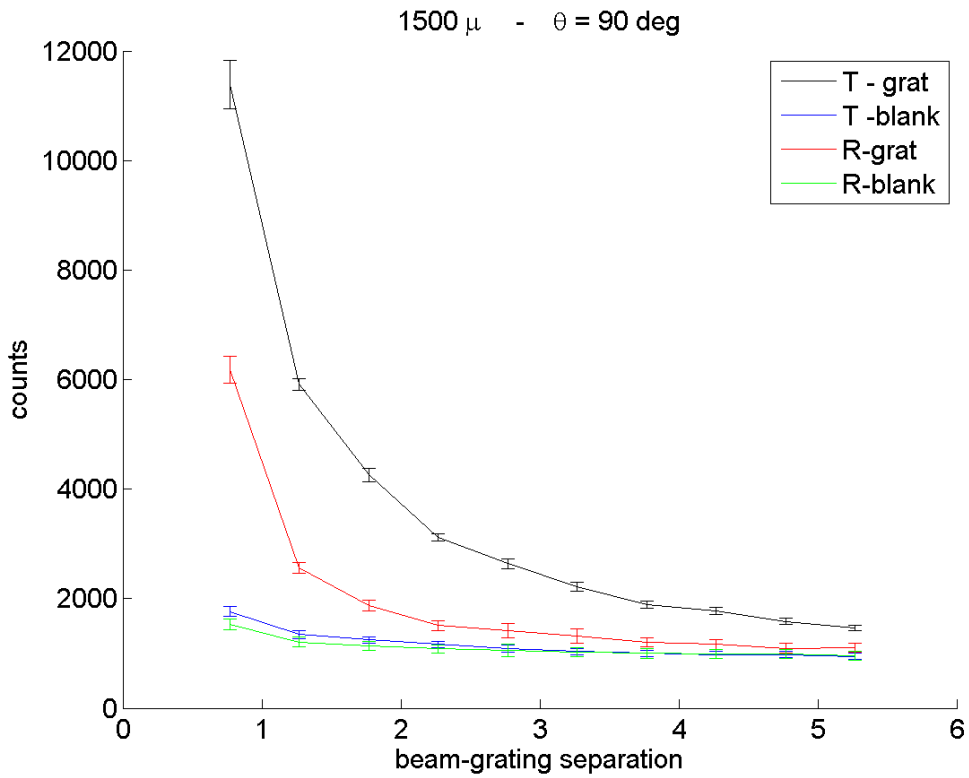

Figure 5.27: Measurements of the two polarization components with the grating and the blank from the 1500 microns grating

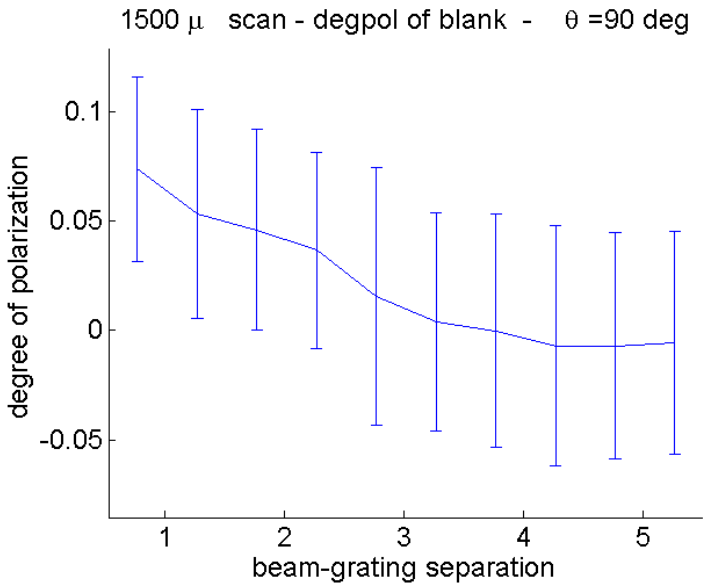

Figure 5.28: Degree of polarization of the background radiation associated to the measurements of the 1500 microns period grating

Such behaviour can be understood if diffraction radiation is taken into account as it yields the degree of polarisation at the short distances between beam and grating. However the intensity of the diffraction radiation drops rapidly as the distance increases. The fact that the blank responses remain relatively similar, while the grating response are significantly different is consistent with the theoretical understanding of polarization of the cSPR. Using the net counts for each polarization component, the degrees of polarization were calculated for each grating and the dependence of the degree of polarisation on the beam grating separation was studied. In the figure 5.26, the net counts for T and R are plotted. Because the two blanks' contributions were small compared to the respective grating signal, the two net curves have essentially the same pattern than in the figure 5.27.

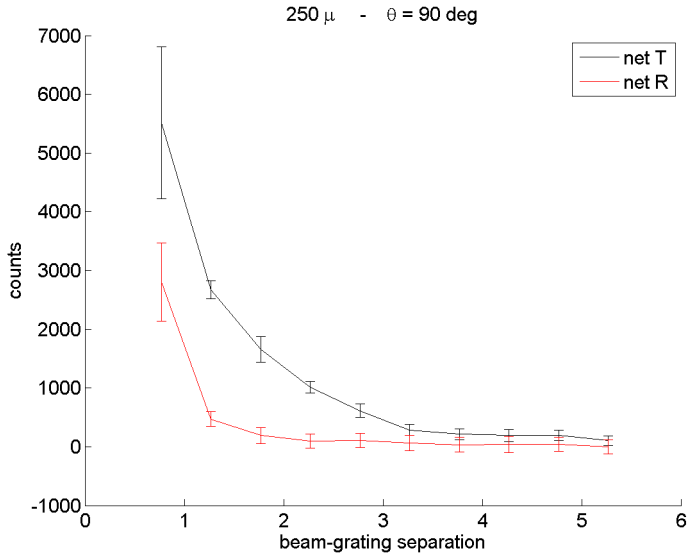

(a)

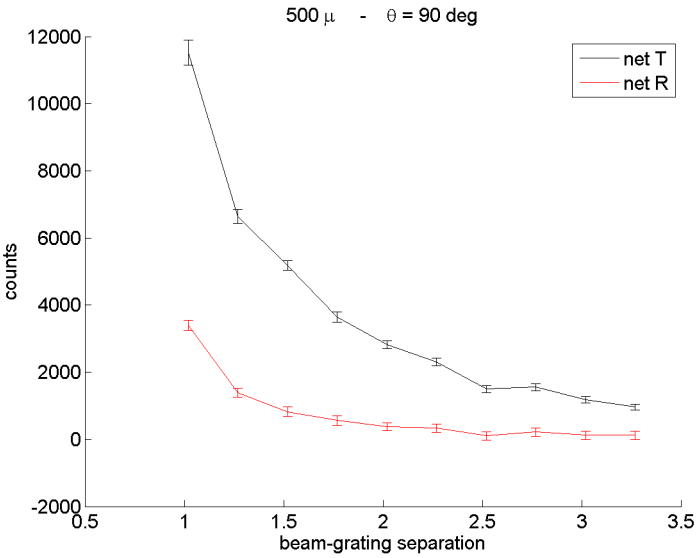

(b)

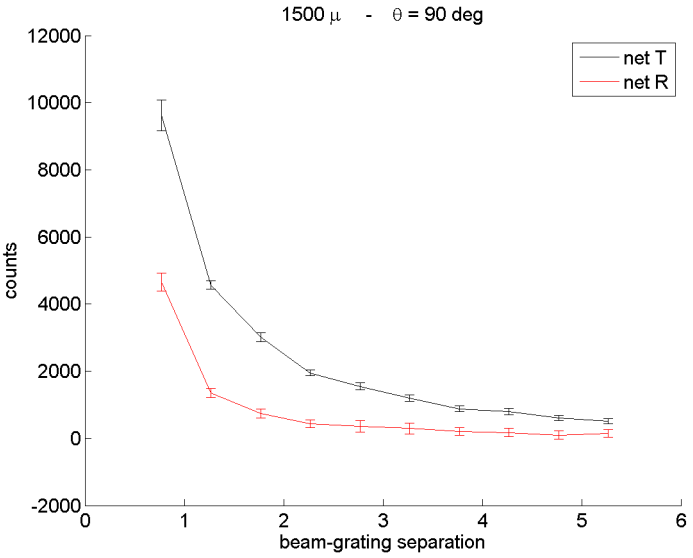

(c)

Figure 5.29: net counts following subtraction for each of the polarization components

The figures 5.30, 5.31 and 5.32 present the results of the studies of degree of polarization of the cSPR for the three gratings, along with the predicted yield from the surface-current theory. In each case, the experimental degree of polarisation fits into the expected interval $[-1, +1]$. The experimental result has a relatively flat response i.e. it is constant, compatible with the uncertainties. This is to be expected, since it has been shown in the chapter 2 that the degree of polarization is completely determined by the grating period, and the two angles θ and ϕ. There is strong variation with change of distance from 0.77 mm to 1.77 mm which is especially clear for 1500 and 500 microns gratings. When comparing with the surface-current theory predictions, it is remarkable to notice that the match with the data is quite satisfactory, especially for the 500 microns grating. It should be noted however that, for small beam-grating separations, the surface-current theory seems to consistently predict a higher yield than the experiment. This is especially true for the 500 and 1500 microns grating, while the 250 microns pattern is compatible with a drop of experimental values at very short distances from the beam.

Discussion of the uncertainties For all gratings, the uncertainties increase dramatically with the beam-grating separation as signal level drops and become comparable with the noise. This increases to the point where the uncertainties can reach values beyond the physical range of $[-1, 1]$. At this point further analysis has no physical meaning. Indeed as signal become of the same level as noise the relative uncertainty of the subtracted signal becomes very large. After that, since the uncertainty propagates on the degree of polarization through its derivative, it becomes even larger.

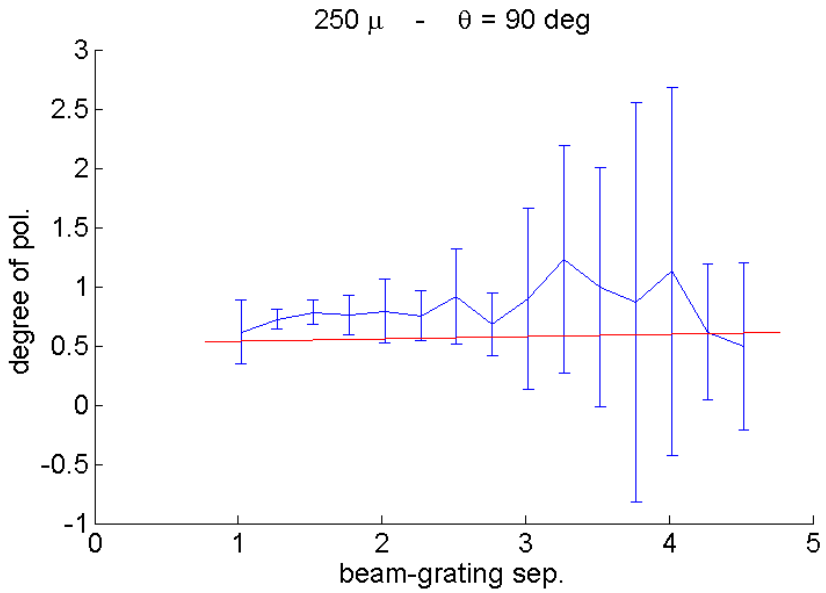

Figure 5.30: Degree of polarisation for the 250 microns grating (in blue) compared with the predicted yield from the surface-current theory (in red)

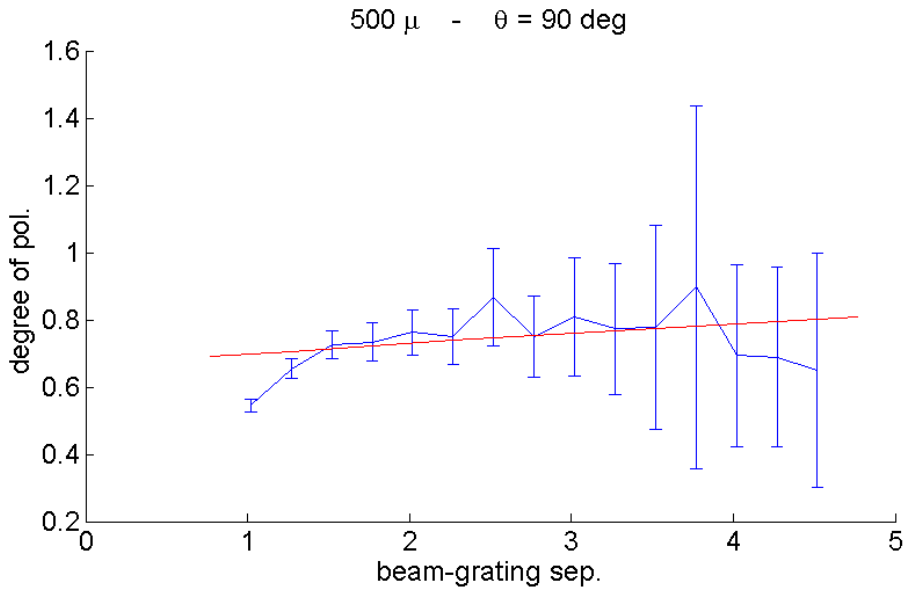

Figure 5.31: Degree of polarisation for the 500 microns grating (in blue) compared with the predicted yield from the surface-current theory (in red)

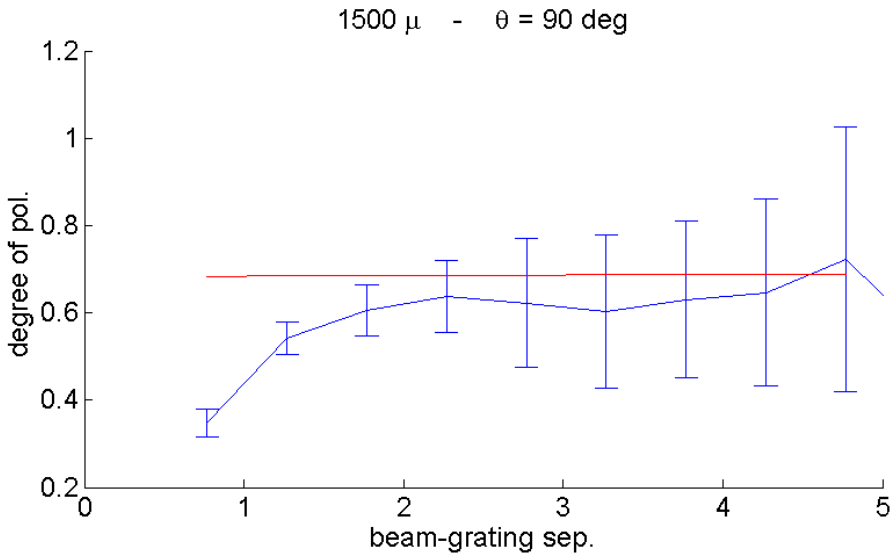

Figure 5.32: Degree of polarisation for the 1500 microns grating (in blue) compared with the predicted yield from the surface-current theory (in red)

Chapter 6

Conclusion

This thesis has presented all my original contributions to the analysis of the experiments that took place in the last three years at SLAC, as well as the supporting simulations that have helped to shed some light on the experimental results. It is worth to notice the strong potential of Smith-Purcell as diagnostic tool and the wide range of possibilities it offers, despite being apparently a very simple process (a bunch travels above a grating at short distance). Because of the growing stronger interest in femtosecond scales bunches driven by research in plasma-wakefield acceleration and FEL's, the potential of cSPR is now beyond doubt. This interest is also strongly motivated by the search for financially affordable diagnostic devices, by opposition to the prohibitive cost of some more traditional tools such as deflecting cavities. In addition of being cost-effective, Smith-Purcell radiation allows to customize the frequency range of interest, since the bandwidth depends only on the grating period.

The formalism used for this work was the surface-current theory. It is not the only one existing, but it has proven to be very effective in explaining the observations, and it is well established in literature that other models fail to describe accurately observations at high energies. As I have shown in this work, in general, the simulations based on the surface-current theory tend to agree reasonably well with the measured spectrum and the azimuthal distribution. However the agreement is often not perfect and this opens room for further

investigations, therefore I would like to say a few words on possible future directions.

Let us first remind that all the reconstructions shown were based on the novel phase-retrieval method called PCI Algorithm that I developed. The major achievement of PCI is that the reconstruction is unique, provided a defined set of parameters is given at input. All previous iterative-Fourier based algorithm could not provide such a result: with previous methods, a given set of reconstruction parameters could generate several solutions, and this would require a substantial amount of post-selection. The finding presented in this thesis regarding the uniqueness of a solution is heuristic, and do not constitute a mathematical proof, but they rely on solid evidence to justify a further study of more mathematical nature. The fundamental feature of PCI, as we have seen, was to implement a KK-boundary condition on Fourier iterations. There could be ways to improve the algorithm in two very different ways:

1. A first option could be to explore a mean of imposing an upper boundary condition on phases. This question is not easy at all to investigate: we can never know if a Fourier transform "overshoots" the upper acceptable limit of a phase and so far there is no equivalent of KK-minimum phase results for the upper-phase ceiling.

2. A second possibility could be to see if KK implemented as boundary condition on a gradient-search iterative algorithm, could bring better results (or not) compared to Fourier-based iterative algorithm like PCI. Gradient-search methods have never been studied very thoroughly despite being very promising: the interest in gradient-search based algorithm originates in their ability to respond very well to signal with several intensities. However the gradient techniques are mathematically heavier than Fourier-type algorithms and hence require more work.

It is only in some pathological situations of mathematical nature that PCI can face problems. Such an example is given by a sum of two Gaussians with the following parameters:

$$A_1 = 1$$

$$A_2 = 0.2$$

$$\sigma_1 = 0.03$$

$$\sigma_2 = 0.21$$

$$\mu_1 = 0.17$$

$$\mu_2 = 0.37$$

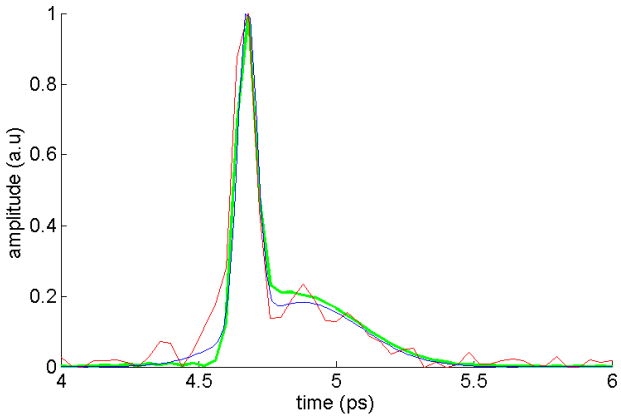

(a)

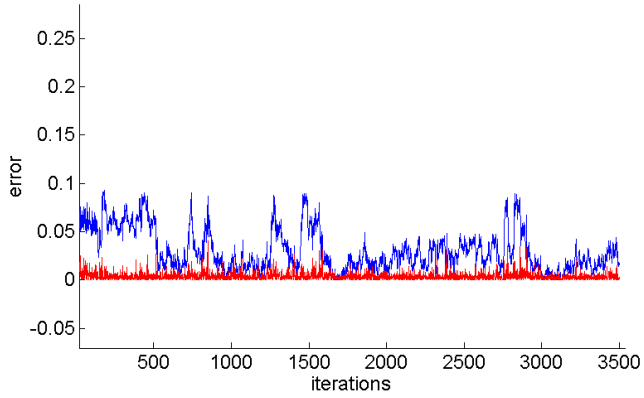

(b)

Figure 6.1: Reconstruction of a problematic Double Gaussian profile at 3500 iterations. Blue: Original Profile – Green : KK retrieval – Red: PCI retrieval (b) The integral errors. Blue : δ_1 - Red: δ_2

In this case, PCI will struggle to converge, as can be seen from the error pattern shown in the figure 6.1, where after 3500 iterations, no decisive convergence of the error integral seems to take place. Despite the difficulty to improve phase-reconstruction algorithms, the current state of PCI is already satisfactory in the sense that in most cases, it gives an equal or better estimate of bunch length than KK, at least for bunch types which are of physical relevance for beam diagnostics.

Regarding the experiment themselves, a few directions of exploration can be proposed:

First, as already mentioned, the azimuthal study is, to the best of our knowledge, the first ever carried. As mentioned above, the agreement with the surface-current theory is reasonably good, without being perfect. I have shown that the surface-current model consistently predicts a wider spatial extension of the cSPR signal in the ϕ direction compared to what is usually observed. This suggests a possible correction to the theory. The interesting part is that, for the very vast majority of measurements, the predicted energy fits extraordinary well within the experimental error bars. This suggests that the overall surface-current model remains a very strong description of cSPR. A possible route of investigation to improve the surface-current model could be provided by the result showed in the bunch diagnostic analysis that a double exponential description in the cSPR radiation integral gives a better fit of the data than a single exponential one: this means that additional modes are present which are responsible of weighting the existing coupling between the beam and the grating.

Having said that, a full azimuthal study would require experiments at various ranges of energy, and not only the ultrarelativistic ones. It should be reminded that some competing cSPR theoretical models have been ruled out because they were agreeing with experiments at some energy range, and contradicting them at some other energy range. It is thus quite natural to say that the azimuthal study provided here should be complemented with other studies that would be undergone at other facilities and in different beam conditions.

Another direction of further work is a more thorough polarization study of the cSPR. As explained in the thesis, the interest in polarization was mostly motivated because it offers a possibility to construct a single-shot device. This is possible only because of supporting evidence that background radiation seems to be unpolarised, or poorly polarized. But here, the study that I carried to show that background polarization is negligible, is valid for FACET facility only, and we should be cautious before making this statement a general result. A clear difficulty comes from the fact that usually, the various sources of background radiation cannot be simulated, and hence a polarisation study relies much more on experimental investigation than other aspects of CSPR.

At this stage, with all the results gathered, the problem of designing a first possible single-shot device becomes largely an engineering problem. Current research is carried at LUCX facility at KEK under the supervision of Dr Konoplev where these topics are addressed, both from an experimental point of view and a theoretical side to improve the surface-current model. One of the design possibility explored is the use of three aligned gratings with different period, and slightly rotated around their alignment axis, in order to cope with the problem of overcrowding of detectors in the limited space available. The work is currently in progress , and experiments are carried out at KEK, Japan [51].

Appendix A

Complementary results on the azimuthal study

During the June 2015 set of experiment, a large amount of data has been collected. Even though I have analysed the totalily of them, this thesis presents only the more representative results in order to avoid repetition of similar type of conclusion. In this perspective, any additional data can be considered as supplementary supportive evidence of the conclusion already made. It is with this idea in mind that some of the additional data of azimuthal study are presented here. Like before, it can be observed that the agreement between the surface-current theory and the experimental data is not always very good, which suggest further work of theoretical nature. It can be noted how the simulations and the experiment differe at various θ for measurements at small ϕ

A.1 Azimuthal signal for the 500 microns grating at 3.24 mm

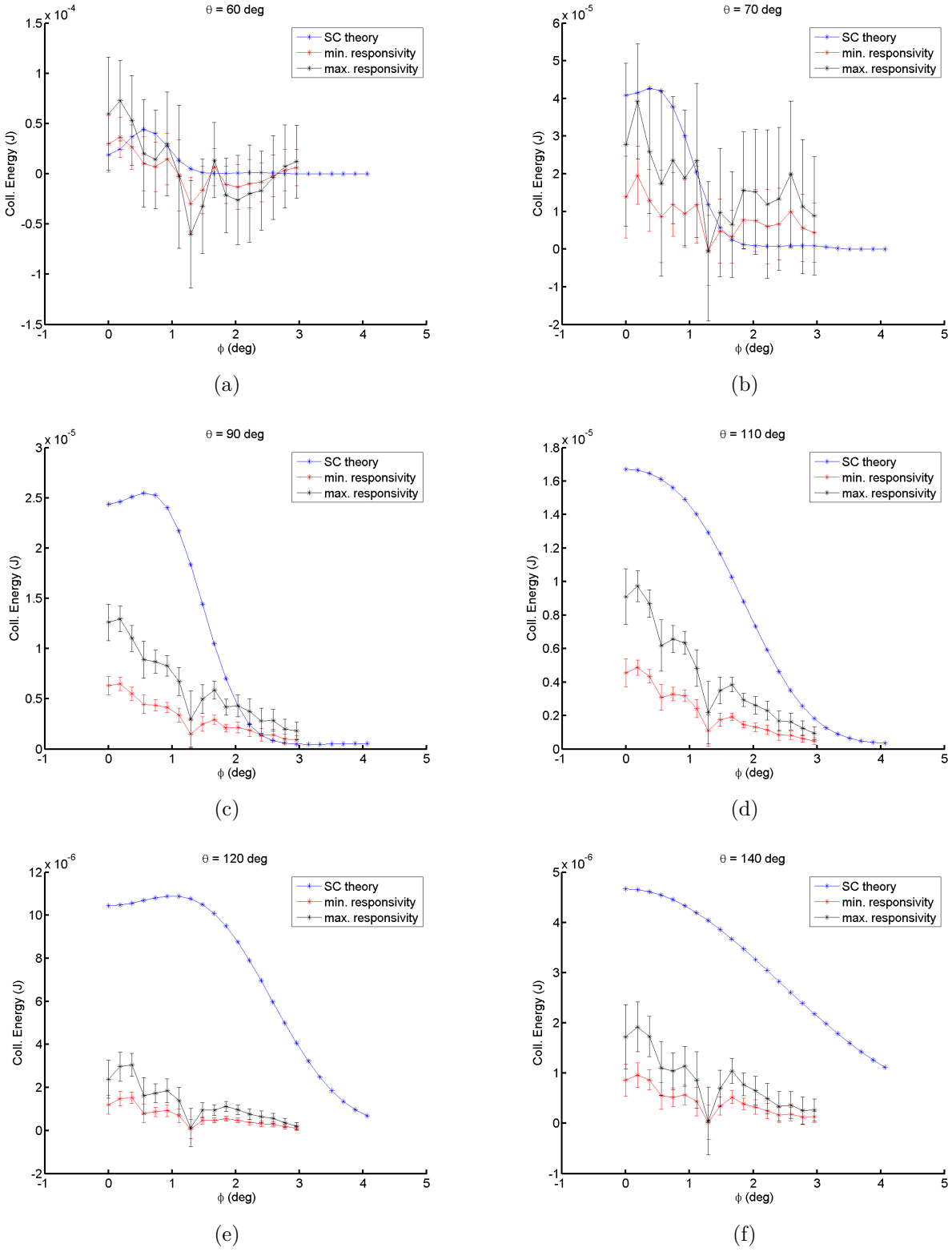

Figure A.1: Comparison of the azimuthal energy collected at the detector with the predictions of the surface current theory for the 500 um grating

A.2 Azimuthal signal for the 250 microns grating at 3.24 mm

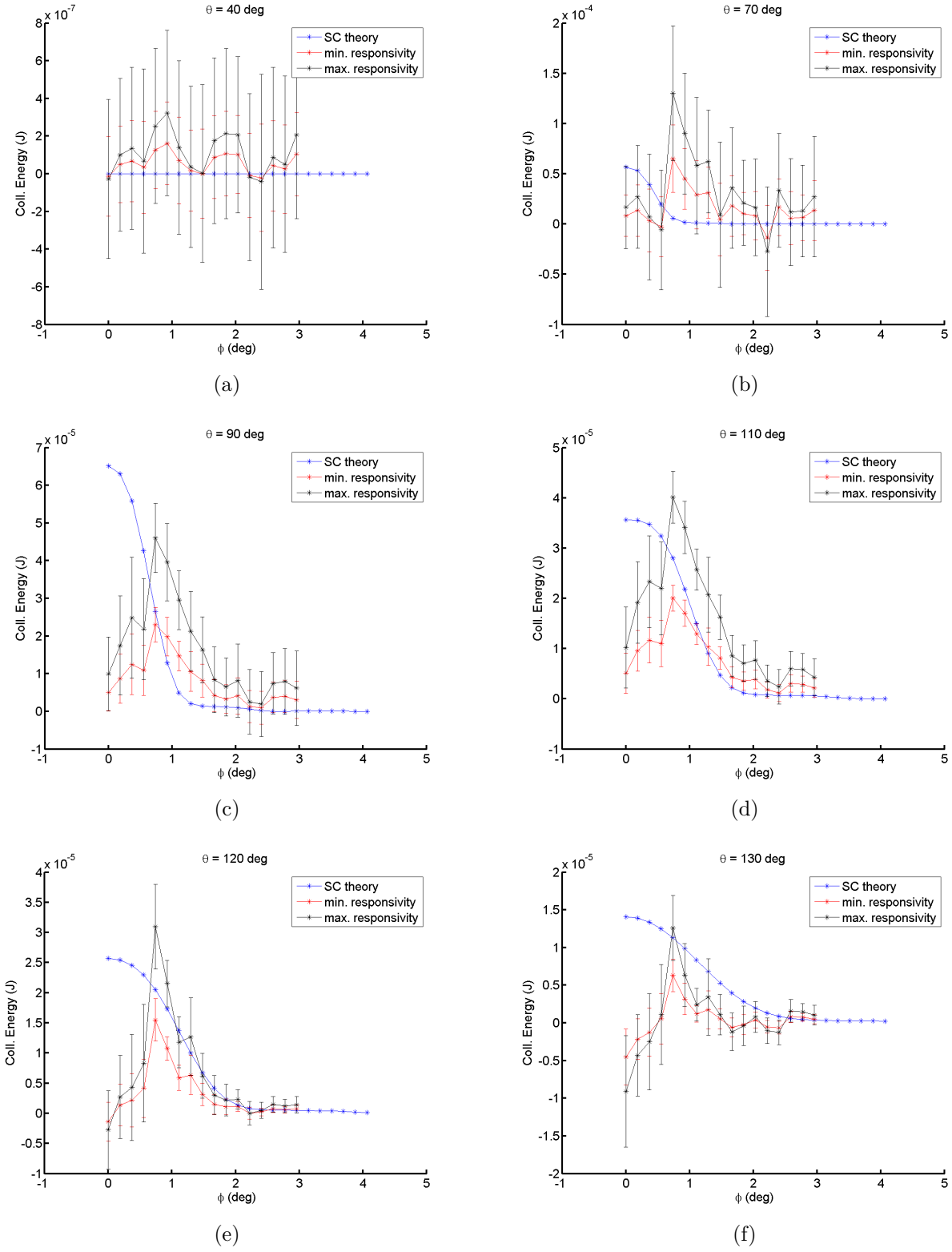

Figure A.2: Comparison of the azimuthal energy collected at the detector with the predictions of the surface current theory for the 250 um grating

Bibliography

[1] P. Forck. "Lecture notes on beam instrumentation and diagnostics". JUAS, Darmstadt,Germany (2011).

[2] O. Grimm. "Principles of longitudinal beam diagnostics with coherent radiation". Technical Report TESLA FEL 2006-03, DESY (2006).

[3] J.S. Nodvick & D.S. Saxon. *Phys. Rev.*, **96** (1954) 180–184. http://link.aps.org/doi/10.1103/PhysRev.96.180

[4] J. Schwinger. *Phys. Rev.*, **75** (1949) 1912–1925. http://link.aps.org/doi/10.1103/PhysRev.75.1912

[5] R.B. Fiorito & D.W Rule. "Optical transition radiation beam emittance diagnostics". In "AIP Conf. Proc. 319, 21 (1994)", Sante Fe, New Mexico (20-23 oct 1993).

[6] G. Decker & X. Sun. "Observation of coherent microwave transition radiation in the APS linac". In "Proceedings of the 2003 Particle Accelerator Conference", (2003).

[7] B. Dolgoshein. *NIM A*, **326** (1993) 434–469.

[8] S. I. Bajlekov, M. Heigoldt, A. Popp, J. Wenz, K. Khrennikov, S. Karsch & S. M. Hooker. *Phys. Rev. ST Accel. Beams*, **16** (2013) 040701. http://link.aps.org/doi/10.1103/PhysRevSTAB.16.040701

[9] G. P. Le Sage, T. E. Cowan, R. B. Fiorito & D. W. Rule. *Phys. Rev. ST Accel. Beams*, **2** (1999) 122802. http://link.aps.org/doi/10.1103/PhysRevSTAB.2.122802

[10] M. Micheler & al. "Longitudinal beam profile monitor at CTF3 based on Coherent Diffraction Radiation". In "Journal of Physics: Conference Series, Volume 236, conference 1", United Kingdom (2010).

[11] G. Doucas, J. H. Mulvey, M. Omori, J. Walsh & M. F. Kimmitt. *Phys. Rev. Lett.*, **69** (1992) 1761–1764. http://link.aps.org/doi/10.1103/PhysRevLett.69.1761

[12] J. Laegsgaard, X. Liu, A. Svane & D. Turchinovich. *SPIE NR*.

[13] Michael J. Moran. *Phys. Rev. Lett.*, **69** (1992) 2523–2526. http://link.aps.org/doi/10.1103/PhysRevLett.69.2523

[14] A.H. Lumpkin, N.S. Sereno & D.W. Rule. *Nuclear Instruments and Methods in Physics Research Section A: Accelerators, Spectrometers, Detectors and Associated Equipment*, **475**, 1–3 (2001) 470 – 475. ISSN 0168-9002. FEL2000: Proc. 22nd Int. Free Electron Laser Conference and 7th F {EL} Users Workshop. http://www.sciencedirect.com/science/article/pii/S0168900201016394

[15] Pavel Karataev, Sakae Araki, Ryosuke Hamatsu, Hitoshi Hayano, Toshiya Muto, Gennady Naumenko, Alexander Potylitsyn, Nobuhiro Terunuma & Junji Urakawa. *Phys. Rev. Lett.*, **93** (2004) 244802. http://link.aps.org/doi/10.1103/PhysRevLett.93.244802

[16] S. J. Smith & E. M. Purcell. *Phys. Rev.*, **92** (1953) 1069–1069. http://link.aps.org/doi/10.1103/PhysRev.92.1069

[17] J. H. Brownell, J. Walsh & G. Doucas. *Phys. Rev. E*, **57** (1998) 1075–1080. http://link.aps.org/doi/10.1103/PhysRevE.57.1075

[18] J. H. Brownell & G. Doucas. *Phys. Rev. ST Accel. Beams*, **8** (2005) 091301. http://link.aps.org/doi/10.1103/PhysRevSTAB.8.091301

[19] J. D. Jackson. "Classical electrodynamics". Wiley, New York, NY, 3rd ed. edition (1999). ISBN 9780471309321. http://cdsweb.cern.ch/record/490457

[20] K. Yee. *IEEE Transactions on Antennas and Propagation*, **14** (1966) 302–307. http://ieeexplore.ieee.org/document/1138693/

[21] H. L. Andrews & al. *Phys. Rev. ST Accel. Beams*, **17** (2014) 052802. http://link.aps.org/doi/10.1103/PhysRevSTAB.17.052802

[22] D. Pellicia & T. Sen. *NIM A*, **764** (2014) 206–214. http://dx.doi.org/10.1016/j.nima.2014.07.02

[23] A.S. Fisher & al. *Rev. Sci. Instrum.*, **84** (2013) 10. http://dx.doi.org/10.1063/1.4790427

[24] P. Emma, J. Frisch & P. Krejcik. "A transverse RF deflecting structure for bunch length and phase space diagnostics". Technical Report LCLS-TN-00-12, SLAC (2000).

[25] M. Litos. "FACET X-band TCAV performance and analysis". In "SLAC ARD BB Seminars", SLAC (2012).

[26] P. Muggli & al. "Measurement of the SLAC ultra-short bunch length using coherent transition radiation autocorrelation". In "Proceedings of the 2005 Particle Accelerator Conference", (2005).

[27] A. Chao & M. Tigner. "Handbook of Accelerator Physics and Engineering". World Scientific, Singapore (1998).

[28] S. Varro & al. "Free electron lasers". INTECH publishers (2012). ISBN 978-953-51-0279-3.

[29] K. J. Woods, J. E. Walsh, R. E. Stoner, H. G. Kirk & R. C. Fernow. *Phys. Rev. Lett.*, **74** (1995) 3808–3811. http://link.aps.org/doi/10.1103/PhysRevLett.74.3808

[30] S. E. Korbly, A. S. Kesar, J. R. Sirigiri & R. J. Temkin. *Phys. Rev. Lett.*, **94** (2005) 054803. http://link.aps.org/doi/10.1103/PhysRevLett.94.054803

[31] J. T. Donohue & J. Gardelle. *Phys. Rev. ST Accel. Beams*, **8** (2005) 060702. http://link.aps.org/doi/10.1103/PhysRevSTAB.8.060702

[32] B. Feng & al. *NIM A*, **475** (2001) 492–497.

[33] C. Balanis. "Advanced engineering electromagnetics". Wiley, USA (2012). ISBN 978-0-470-58948-9.

[34] Levi Schächter & Amiram Ron. *Phys. Rev. A*, **40** (1989) 876–896. http://link.aps.org/doi/10.1103/PhysRevA.40.876

[35] J. T. Donohue & J. Gardelle. *Phys. Rev. ST Accel. Beams*, **9** (2006) 060701. http://link.aps.org/doi/10.1103/PhysRevSTAB.9.060701

[36] P. M. van den Berg. *J. Opt. Soc. Am.*, **63**, 6 (1973) 689–698. http://www.osapublishing.org/abstract.cfm?URI=josa-63-6-689

[37] S. Marchesini, H. He, H. N. Chapman, S. P. Hau-Riege, A. Noy, M. R. Howells, U. Weierstall & J. C. H. Spence. *Phys. Rev. B*, **68** (2003) 140101. http://link.aps.org/doi/10.1103/PhysRevB.68.140101

[38] H. Backe. "Investigation of far-infrared Smith-Purcell radiation at the 3.41 MeV electron injector linac of the MAINZ Microtron MAMI", pages 267–282. Springer Netherlands, Dordrecht (2006). ISBN 978-1-4020-3450-3. http://dx.doi.org/10.1007/1-4020-3450-4$_1$9

[39] Richard P. Leavitt, Donald E. Wortman & Clyde A. Morrison. *Applied Physics Letters*, **35**, 5 (1979) 363–365. http://scitation.aip.org/content/aip/journal/apl/35/5/10.1063/1.91151

[40] S. Korbly & al. "Progress on a Smith-Purcell radiation bunch length diagnostics". In "Proceedings of the 2003 Particle Accelerator Conference", (2003).

[41] Amit S. Kesar, Mark Hess, Stephen E. Korbly & Richard J. Temkin. *Phys. Rev. E*, **71** (2005) 016501. http://link.aps.org/doi/10.1103/PhysRevE.71.016501

[42] R. Lai & A. J. Sievers. *Phys. Rev. E*, **50** (1994) R3342–R3344. http://link.aps.org/doi/10.1103/PhysRevE.50.R3342

[43] S. Korbly & al. *Phys. Rev. ST Accel. Beams*, **9** (2006) 022802. http://link.aps.org/doi/10.1103/PhysRevSTAB.9.022802

[44] Vinit Kumar & Kwang-Je Kim. *Phys. Rev. E*, **73** (2006) 026501. http://link.aps.org/doi/10.1103/PhysRevE.73.026501

[45] R Lai & A.J Sievers. *Nuclear Instruments and Methods in Physics Research Section A: Accelerators, Spectrometers, Detectors and Associated Equipment*, **397**, 2 (1997) 221 – 231. ISSN 0168-9002. http://www.sciencedirect.com/science/article/pii/S0168900297006906

[46] Gi Schneider, R Lai, W Walecki & A.J Sievers. *Nuclear Instruments and Methods in Physics Research Section A: Accelerators, Spectrometers, Detectors and Associated Equipment*, **396**, 3 (1997) 283 – 292. ISSN 0168-9002. http://www.sciencedirect.com/science/article/pii/S016890029700781X

[47] J. R. Fienup. *Appl. Opt.*, **21**, 15 (1982) 2758–2769. http://ao.osa.org/abstract.cfm?URI=ao-21-15-2758

[48] J. R. Fienup & C. C. Wackerman. *J. Opt. Soc. Am. A*, **3**, 11 (1986) 1897–1907. http://josaa.osa.org/abstract.cfm?URI=josaa-3-11-1897

[49] Heinz H. Bauschke, Patrick L. Combettes & D. Russell Luke. *J. Opt. Soc. Am. A*, **19**, 7 (2002) 1334–1345. http://josaa.osa.org/abstract.cfm?URI=josaa-19-7-1334

[50] J. Fienup. "Phase retrieval for imaging and wavefront sensing". In "General Dynamics Distinguished Lecture Series", Michigan (2006).

[51] H. Harrison & al. "First steps towards a single-shot longitudinal profile monitor: study of the properties of coherent smith-purcell radiation using the surface current model." In "Proceedings of the 2016 International Particle Accelerator Conference", Korea (2016).

[52] V. Blackmore. "Determination of the time profile of picosecond-Long electron bunches through the use of coherent Smith-Purcell radiation". Ph.D. thesis, University of Oxford (2008).